Modeling Bubble Coarsening in Froth Phase from First Principles

Seungwoo Park

Dissertation submitted to the faculty of the
Virginia Polytechnic Institute and State University
in partial fulfillment of the requirements for the degree of

Doctor of Philosophy
In
Mining and Minerals Engineering

Roe-Hoan Yoon, Chair
Gerald H. Luttrell
Gregory T. Adel
Saad A. Ragab
Sunghwan Jung

February 27, 2015
Blacksburg, Virginia

Keywords: Bubble-Coarsening, Froth Stability, Thin Liquid Film, Hydrophobic Force

Modeling Bubble Coarsening in Froth Phase from First Principles

Seungwoo Park

ABSTRACT

Between two neighboring air bubbles in a froth (or foam), a thin liquid film (TLF) is formed. As the bubbles rise upwards, the TLFs thin initially due to the capillary pressure (p_c) created by curvature changes. As the film thicknesses (H) reach approximately 200 nm, the disjoining pressure (Π) created by surface forces in the films also begins to control the film drainage rate and affect the waves motions at the air/water interfaces. If $\Pi < 0$, both the film drainage and the capillary wave motion accelerate. When the TLF thins to a critical film thickness (H_{cr}), the amplitude of the wave motion grows suddenly and the two air/water interfaces touch each other, causing the TLF to rupture and bubbles to coalesce.

In the present work, a new model that can predict H_{cr} has been developed by considering the film drainage due to both viscous film thinning and capillary wave motion. Based on the H_{cr} model, bubble-coarsening in a dynamic foam has been predicted by deriving the geometric relation between the thickness of the lamella film, which controls bubble-coalescence rate, and the Plateau border area, which controls liquid drainage rate.

Furthermore, a model for predicting bubble-coarsening in froth (3-phase foam) has been developed by developing a film drainage model quantifying the effect of particles on p_c. The parameter p_c is affected by the number of particles and the local capillary pressure ($p_{c,local}$) around particles, which in turn vary with the hydrophobicity and size of the particles in the film. Assuming that films rupture at free films, the p_c corrected for the particles in lamella films has been used to determine the critical rupture time (t_{cr}), at which the film thickness reaches H_{cr}, using the Reynolds equation. Assuming that the number of bubbles decrease exponentially with froth height, and knowing that bubbles coalesce when film drains to a thickness H_{cr}, a bubble coarsening model has been developed. The model predictions are in agreement with the experimental data obtained using particle of varying hydrophobicity and size.

Acknowledgement

Foremost, I would like to express my sincerest gratitude to my research advisor, Dr. Roe-Hoan Yoon, for providing me an opportunity to challenge such an attractive research area and teaching me how to generate new ideas from fundamental studies.

I am also grateful to Dr. Gerald Luttrell for introducing me hydrodynamic theories, Dr. Gregory Adel for teaching me how to make a professional presentation through his seminar courses, Dr. Saad Ragab for his critical comments on this dissertation, and Dr. Sunghwan Jung for his continued academic advice and valuable classes.

The completion of this work would not have been possible without the support and encouragement of all of the staff members and students at Center for Advanced Separation Technologies. Particular appreciations are expressed to Gaurav Soni and Kaiwu Huang for incorporating the theoretical models developed in this study into a simulator, Dr. Lei Pan for useful discussions and innovative suggestions, and Whiusu Shim for helping me prepare samples and assisting me with image-processing.

I also have been blessed with Dr. Jai-Koo Park and Dr. Sungsoo Cha, who helped me achieve career planning during their visit.

I am also grateful to FLSmidth for funding continuously and providing me with necessary facilities for this project.

I wish to express my sincere thanks to Prof. Siyoung Jeong for propelling me forward since I was an undergraduate.

Finally, I want to acknowledge my family for their love, sacrifice, and patience.

Contents

List of Figures

List of Tables

Chapter 1. Introduction

1.1 Preface

Froth flotation is a method for selectively separating a particulate material from one another by means of the air bubbles dispersed in liquid medium. The flotation technology has been widely used for upgrading pulverized ores in the mining industry, removing contaminants from waste water in the water treatment industry, capturing printing ink from paper fibers in the paper recycling industry, and extracting bitumen form oil sands.

In the minerals separation process, the surface of desired mineral particles is rendered hydrophobic by the absorption of collector (hydrophobizing reagent), whereas that of undesirous minerals remain hydrophilic. The Gibbs energy change (ΔG) associated with the bubble-particle attachment is given by the following form [1],

$$\Delta G = \gamma(\cos\theta - 1) \tag{1.1}$$

where γ is the interfacial tension between liquid and air phases and θ is the water contact angle. Eq. (1.1) indicates that only the attachment between a bubble and a particle with $\theta > 0°$ is thermodynamically favorable. Hence, only the hydrophobized particles selectively can attach to air bubbles, form particle-bubble aggregates, which rise upward due to buoyancy, and form a froth layer at the surface of the pulp phase.

True recovery in the froth phase occurs when the particles attached to bubbles reaches the top of the froth and finally flow into a launder without detachment. As the particle-coated bubbles rise upward along the froth height, they coalesce with each other and become larger. As the bubbles become coarser, the bubble surface area decreases, thereby detaching desired hydrophobic particles from bubbles and causing the true recovery to decrease. However, less hydrophobic particles tend to be detached preferentially, so the froth phase contributes to enhance the grade of a froth product [2].

On the other hand, particles suspended in the pulp can also be recovered without adhesion to bubbles through the entrainment mechanism. The froth recovery due to entrainment occurs when interstitial liquid between bubbles drag particles from the pulp and allow them to reach the launder. The dragging effect may stem from the agitation in the pulp (mechanical entrainment), the wake behind a rising bubble, or bubble swarm crowding effect (hydraulic entrainment). Since entrainment is non-selective, not only hydrophobic but also hydrophilic particles can be recovered, lowing the grade product [3].

As stated, flotation is a multi-phase process involving a variety of physicochemical phenomena and those are interacting each other. As a result, quantitative flotation modelling and simulations are highly required to explore the flotation science and optimize the operation of overall process. In the following section, literatures associated with the two distinct phases, pulp and froth phases, respectively, are briefly reviewed, particularly in modelling perspective. Next, the objective of the present doctoral research is presented.

1.2 Literature Review

1.2.1 Pulp

A. Bubble Generation Model

In a flotation cell, bubbles are generated by splitting injected air into tiny air bubbles and the splitting pressure is originated from rotational motion of a rotor. The splitting pressure is opposed by the surface tension force tending to resist deformation and minimize the surface area of the air/water interface. The ratio of splitting pressure to capillary pressure is defined as Weber number (*We*). Hinze [4] suggested that if *We* reaches a critical value, bubble breaks. The critical Weber number (We_{cr}) is obtained from the following expressions,

$$We_{cr} \equiv \frac{\text{Splitting pressure}}{\text{Capillary pressure}} = \frac{\rho \overline{u^2} d_{2,\max}}{\gamma} \tag{1.2}$$

where ρ is the liquid density, $\overline{u^2}$ is the mean square velocity difference between two points, $d_{2,\max}$ is maximum stable bubble size, and γ is the surface tension. The value of $\overline{u^2}$ is given by [5],

$$\overline{u^2} = C(\varepsilon d_{2,\max})^{2/3} \tag{1.3}$$

where C is the empirical constant and ε is the energy dissipation rate, which can be calculated from follows,

$$\varepsilon = \frac{P}{\rho V} \tag{1.4}$$

where P the power input and V the volume of liquid.

Thus, one can predict $d_{2,\max}$ using Eq. (1.2) if the value of We_{cr} is known, However, there is no consensus on the value of We_{cr}, which may vary with experimental conditions. The known values of We_{cr} include 1.0, 1.2, and 4.7 as reported by Schulze [6] and Schubert [7], Hinze [4], and Lewis *et al*. [8], respectively. Schulze [6] found experimentally that We_{cr} =1 in for bubble generation in water, and that C = 0.47 under turbulent flow conditions. Accordingly, the $d_{2,\max}$ is given by,

$$d_{2,\max} = \left(\frac{2.11\gamma}{\rho\varepsilon^{0.66}}\right)^{0.6} \tag{1.5}$$

Schubert [7] presented a similar bubble generation model by arbitrarily assuming We_{cr} = C =1,

$$d_{2,\max} = \left(\frac{\gamma}{\rho\varepsilon^{0.66}}\right)^{0.6} \tag{1.6}$$

Parthasarathy *et al*. [9] found that the value of We_{cr} is dependent on C and that We_{cr}/C = 7, which gave the following bubble generation model,

$$d_{2,\max} = \left(\frac{7\gamma}{\rho\varepsilon^{0.66}}\right)^{0.6} \tag{1.7}$$

B. Drift-Flux Model

The bubbles generated in the pulp phase of a flotation cell rise upwards due to buoyancy, and the bubble velocity relative to water, or the bubble slip velocity (U_{slip}), is expressed as [10],

$$U_{slip} = \frac{V_g}{1-\varepsilon} \pm \frac{V_l}{\varepsilon} \tag{1.8}$$

where V_g and V_l are the superficial gas and liquid (slurry) velocities, respectively, and ε is the liquid volume fraction. The +/- signs indicates counter-current and-co-current flows of gas and liquid, respectively.

Empirically, it was found that U_{slip} is a function of the terminal rise velocity (U_t) of a single bubble in an infinite pool and ε [11],

$$U_{slip} = U_t \varepsilon^{m-1} \tag{1.9}$$

where m is the empirical parameter that depends on flow patterns. In using Eq. (1.9), the value of U_t is given by [12],

$$U_t = \frac{g\rho d_2^{\,2}}{18\mu(1+0.15\mathrm{Re}^{0.687})} \quad (d_2 < 1.5\,\mathrm{mm}) \tag{1.10}$$

where g is the gravitational , d_2 is the bubble diameter, μ is the liquid viscosity, and Re is the Reynolds number, given by $d_2\rho U_t / \mu$. In the case of a coarse bubble1(1.5 mm $\leq d_2 \leq$ 10 mm), U_t is independent of d_2 and reaches approximately 21 cm/s [13].

By combining Eqs. (1.8) ~ (1.10), one can predict one of unknown parameters if the others are measurable. Banisi and Finch [14] and Ityokumbul *et al*. [15] used the drift-flux analysis to predict the average bubble size dispersed in the pulp in a flotation column. Stevenson *et al*. [16] used the theory to predict liquid overflow rate from a foam column.

1.2.2 Froth

In the Section A below, the bulk motion of a froth (or a foam) in a flotation cell is described. The froth is composed of a cloud of air bubbles. Between three bubbles, a triangular channel called

a Plateau border (PB) is formed, through which liquid drains, as will be described in Section B below. Although liquid drainage models neglect the water presence in the thin film (lamella) formed between two bubbles, the lamella films play an importance role forth and foam stability since bubbles coalesce when the thickness of a lamella film reaches a critical value (h_c). In Section C, the thinning kinetics of lamella films is discussed. In section D, a number of methodology to quantify froth stability is reviewed.

A. Bulk Motion of a Froth

Based on continuum-flow approach, the bulk motion of a froth has been described by the Laplace equation [17-19],

$$\Delta^2\psi = 0 \tag{1.11}$$

where Ψ is the stream function. As is well known, Eq. (1.11) requires incompressible and irrotational flow conditions. The incompressible condition has been assumed due to the fact that the water content in flotation froth may not be enough to compress bubbles and change the volume of them. On the other hand, the irrotational flow assumption has been made based on the premise that the geometry of a flotation cell is generally simple and thus swirling flow cannot be created.

B. Foam Drainage

Verbist *et al*. [20] calculated the liquid drainage velocity through a Plateau border (PB) based on the assumption of Poiseuille-type flow and no-slip boundary condition on air/water interface. Consider a single vertical PB with a cross-sectional area *A*. From the Young-Laplace equation, one can obtain the pressure difference across the PB,

$$p = p_g - \frac{\gamma}{R_{PB}} = p_g - \frac{\gamma}{\sqrt{A}/C} \tag{1.12}$$

where p is the pressure in the PB, p_g is the gas pressure in a bubble, and R_{PB} is the radius of the PB, given by $\sqrt{A}/C$. Here C is the dimensionless geometric parameter. The pressure gradient along the vertical direction x is written as,

$$-\frac{\partial p}{\partial y}=\frac{\partial}{\partial y}\left(\frac{\gamma}{R_{\mathrm{PB}}}\right)=-0.5C\gamma A^{-3/2}\frac{\partial A}{\partial x} \tag{1.13}$$

The pressure gradient should be balanced by gravity, ρg, and dissipative force,

$$-0.5C\gamma A^{-3/2}\frac{\partial A}{\partial x}=\rho g+\frac{f\mu u}{A} \tag{1.14}$$

where u is the liquid drainage velocity averaged over A and f is the PB drag coefficient, can vary with geometry of PB and boundary condition of PB wall. Hence, the drainage rate u is

$$u=-\frac{\rho g A}{fu}-\frac{C\gamma}{2f\mu A^{1/2}}\frac{\partial A}{\partial x} \tag{1.15}$$

The first and the second term on the right side represent the contributions from gravity and capillary suction, respectively.

Eq. (1.15) have some limitations for describing the liquid drainage in a flotation froth. In a flotation froth, air bubbles are not stationary and moves relatively to the liquid. The rising bubble, therefore, could may affect the liquid flow by dragging, but the dragging effect is neglected. Inertial effect is also neglected in Eq. (1.15), but in a froth consisting of large bubbles, inertia may become significant. Moreover, it assumes that viscous loss occurs only in the PBs (channel-dominated hypothesis). However, several researchers have recently reported that most viscous loss occurs at the node, where four PBs meet [21-24]. In a dry foam, the liquid content in the node is quite negligible compared to the same in the PB, thus the channel-dominated hypothesis may be applicable.

C. Film Drainage

Reynolds [25] used simplified Navier–Stokes equations with lubrication approximation to describe the squeezing liquid flow between two flat immobile surfaces. Similarly, the drainage of a lamella film can be described by the Reynolds lubrication equation. The pressure in the lamella film can be calculated by the following equation,

$$\frac{\partial p}{\partial r} = \mu \frac{\partial^2 u}{\partial z^2} \tag{1.16}$$

where p is the excess pressure in the lamella, u is the axial liquid velocity along the radial direction r, and z is the vertical coordinate. By substituting Eq. (1.16) into continuity equation, one can deduce the film thinning rate,

$$\frac{dH}{dt} = \frac{1}{12\mu r} \frac{\partial}{\partial r} \left(rH^3 \left(\frac{\partial p}{\partial r} \right) \right) \tag{1.17}$$

where H is the film thickness and t is the drainage time. By considering the averaged p within the entire film, one can obtain the Reynolds lubrication equation,

$$\frac{dH}{dt} = -\frac{2H^3 p}{3\mu R_f^2} \tag{1.18}$$

where R_f is the film radius. Here the average pressure p is given by,

$$p = p_c - \Pi \tag{1.19}$$

where p_c is the capillary pressure and Π is the disjoining pressure incorporating intermolecular forces. The capillary pressure p_c is given by,

$$p_c = \frac{2\gamma}{R} \tag{1.20}$$

where R is the bubble radius. In calculating Π, in the original model, only the contributions from the electrostatic and van der Waals forces, according to the classical Derjaguin-Landau-Verwey-Overbeek (DLVO) theory. However, in the present study, according the extended DLVO theory [26], the contribution from the hydrophobic force is considered additionally,

$$\Pi = \Pi_{el} + \Pi_{vw} + \Pi_{hp} = 64 C_{el} R_2 T \tanh^2 \left(\frac{e\psi_s}{4kT} \right) \exp(-\kappa H) - \frac{A_{232}}{6\pi H^3} - \frac{K_{232}}{6\pi H^3} \tag{1.21}$$

where Π_{el}, Π_{vw}, and Π_{hp} represent the contribution from the electrostatic, van der Waals, hydrophobic forces, respectively, C_{el} the electrolyte concentration, R_2 the gas constant, T the

absolute temperature, e the electronic charge, ψ_s the surface potential at the air/water interfaces, k the Boltzmann's constant, and κ the reciprocal Debye length.

D. Froth Stability

The froth (or foam) stability, by definition, is the ability of air bubbles in froth phase to resist coarsening and bursting. As is well known, froth stability has a significant effect on determining product grade and recovery in flotation. Therefore, various criteria have been proposed to quantify the froth stability. In general, they can be categorized into two subgroups, *i.e.* static tests and dynamic tests.

In static tests, froth is freely allowed to coalesce without creating additional bubbles. Iglesias [27] used a froth decay rate as an indicator of froth stability. When froth height (h_f) reaches an equilibrium, the air supply to the cell was discontinued and immediately started to measure the h_f as a function of time t, as follows,

$$\text{Froth decay rate} = \frac{dh_f(t)}{dt} \tag{1.22}$$

Instead of monitoring a decaying foam continuously, Zanin [28] simply measured the time need for a foam height to drop to one half of its initial height and the half-life time was used as a measure of froth stability.

On the other hand, in dynamic tests, the froth stability is measured while bubbles are being generated continuously. Therefore, during the tests, the bubbles at the base of the froth are allowed to experience coalescences while moving upwards along the froth height. Due to these similarities between the dynamic tests and real flotation tests, as compared to static tests, dynamic tests may provide more reliable froth stability criterion in flotation applications [27]. Bikerman [29] was the first to propose a methodology for a dynamic test. He introduced the concept of the dynamic stability factor (Σ), which is the ratio of the maximum volume of froth to the air flowrate,

$$\Sigma = \frac{h_{f,max} \times A}{Q} \tag{1.23}$$

where A is the cross-sectional area of a cell and Q is the volumetric air flowrate. Barbian [30] suggested the maximum froth depth $h_{f,max}$ can be a froth stability indicator at equilibrium status. In the case of growing froth, he monitored h_f as a function of time t and the froth rising velocity, u (t) = dh_f(t)/dt, was used as an indicator. The model suggests that as froth becomes stable, u (t) approaches the superficial gas velocity (V_g). The air recovery has been used by several researchers and it is defined as the fraction of air injected into a flotation cell that overflows the cell lip as unburst bubbles [31-33]. The primary limitation of the air recovery concept is that it is volume-based approach though the flotation performance relies mainly on the bubble surface area. Ata [34] measured the bubble size distribution along froth height and the froth stability was quantified in terms of the bubble growth rate. Laplante [35] presented the froth retention time (FRT), which is given by the following equation,

$$\mathrm{FRT} = \frac{h_f}{V_g} \tag{1.24}$$

Eq. (1.24) can also be regarded as the measure of average life time of bubble. More recently, Hu [36] monitored the change in electrical impedance by means of a pair of electrodes immersed in froth phase. It was found that bubble coalescence or froth structure variation can vary the value of electrical impedance sensitively. Based on this finding, the degree of impedance variation was used as a froth stability criteria in his study.

1.2.3 Flotation Model

The flotation as a first-order rate process can be represented as follows [37, 38],

$$\frac{dN_1}{dt} = -kN_1 = Z_{12}P \tag{1.25}$$

where N_1 is the number of particles in the cell at time t, k is the flotation rate constant, P is the probability of flotation, and Z_{12} is the collision frequency between particle **1** and bubble **2**, given by the following relation [7],

$$Z_{12} = 2^{3/2}\pi^{1/2}N_1N_2d_{12}^2\sqrt{\overline{u_1^2} + \overline{u_2^2}} \tag{1.26}$$

where N_2 is the number of bubbles on the cell, d_{12} is the collision diameter (sum of radii of bubbles and particles), and $\overline{u_1^2}$ and $\overline{u_2^2}$ are root mean square velocities of the particles and bubbles, respectively. Here, the values of $\overline{u_1^2}$ and $\overline{u_2^2}$ can be determined as presented previously by Schubert [7] and Lee *et al*. [39], respectively.

In using Eq. (1.25), P may be expressed in the form,

$$P = P_c P_a (1 - P_d) P_f \tag{1.27}$$

where P_c is the probability of collision, P_a the probability of attachment, P_d the probability of detachment, and P_f the probability of particles surviving froth phase.

In using Eq. (1.27), P_c can be determined from stream functions for water around air bubbles [40],

$$P_c = \tanh^2\left(\sqrt{\frac{3}{2}\left[1+\frac{3}{16}\left(\frac{\mathrm{Re}}{1+0.249\mathrm{Re}^{0.56}}\right)\right]}\left(\frac{d_1}{d_2}\right)\right) \tag{1.28}$$

where Re is the Reynolds number, d_1 and d_2 the diameters of a particle and a particle, respectively.

In using Eq. (1.27), P_a can be readily calculated using the following equation [40, 41],

$$P_a = \exp\left(-\frac{E_1}{E_k}\right) \tag{1.29}$$

where E_1 is the energy barrier and E_k is the kinetic energy of a particle. E_1 is equal to the maximum potential energy between a bubble and a particle, which can be obtained from the extended DLVO theory and E_k is calculated using the following relation,

$$E_k = 0.5 m_1 (U_{Hcr})^2 \tag{1.30}$$

where m_1 is the mass of a particle, and U_{Hcr} is the velocity of a particle approaching a bubble at the critical rupture thickness (H_{cr}) of the wetting film in between. The value of U_{Hcr} is inversely proportional to the hydraulic resistance force against the thinning.

In using Eq. (1.27), P_d is given as follows [26],

$$P_d = \exp\left(-\frac{W_a + E_1}{E_k'}\right) \tag{1.31}$$

where W_a is the work of adhesion and E_k' is the kinetic energy that detaches a particle from a bubble surface. Here W_a is obtained as follows,

$$W_a = \gamma\pi r_1^2(1-\cos\theta)^2 \tag{1.32}$$

where γ is the surface tension of water, r_1 is the particle radius, and θ is the water contact angle. In using Eq. (1.31), E'_k may be found by the following relation [26],

$$E'_K = 0.5m_1\left((d_1 + d_2)\sqrt{\varepsilon/\nu}\right)^2 \tag{1.33}$$

where ε is the energy dissipation rate and ν is the kinematic viscosity.

Once particles enter the froth phase, only a part of them survives the froth phase and reaches the launder. In determining P using Eq. (1.27), the probability of particles surviving froth phase (P_f) is given as [42, 43],

$$P_f = P_{fa} + P_{fe} = R_{max}\exp(-\alpha\tau_f) + R_{FW,max}\exp(-0.0325\Delta\rho - 0.063d_1) \tag{1.34}$$

in which P_{fa} and P_{fa} are the froth recovery due to attachment and entrainment, respectively, R_{max} the maximum recovery factor, α fitting parameter, τ_f the froth retention time, $R_{FW,max}$ the maximum feed water recovery to froth, and $\Delta\rho$ the specific gravity difference between particle and water. Here R_{max} is given by,

$$R_{max} = \frac{S_t}{S_b} = \left(6V_g / d_{2,t}\right)/\left(6V_g / d_{2,b}\right) = \frac{d_{2,b}}{d_{2,t}} \tag{1.35}$$

where S_t and S_b are the surface area rates of the bubbles at the top and bottom of the froth phase; $d_{2,t}$ and $d_{2,b}$ are bubble diameters at the top and bottom of the froth phase, respectively; and V_g is the superficial gas velocity.

1.3 Research Objective

As shown in Eqs. (1.34) and (1.35), the froth recovery depends strongly on the bubble-coarsening factor ($d_{2,b}/d_{2,t}$), which is the bubble size ratio between the bottom and the top of a froth phase. As a result, it is of critical importance to understand the mechanisms of bubble-coarsening phenomena in a flotation froth. In determining the bubble-coarsening factor, the bubble size at the bottom of a froth ($d_{2,b}$) may be considered to be the same as the bubble size in the pulp phase, which can be readily predicted from bubble generation model. However, at present, there are no models that can predict the bubble size at the top of a froth ($d_{2,t}$) from $d_{2,b}$. The primary objective of the present study is, therefore, to develop a model for predicting the bubble-coarsening in a froth phase from first principles.

For this to be possible, it is essential to know the critical thickness (H_{cr}) of lamella films at which two neighboring bubbles in a froth coalesce and bubble-coarsening occurs. Therefore, the present work is also aimed to develop a predictive model for the value of H_{cr}.

1.4 Organization

The body of this dissertation consists of six chapters.

Chapter 1 provides a comprehensive review of flotation models. Some of them are used to develop theoretical models presented in the following chapters. This chapter also introduces the goal of the present work.

Chapter 2 introduces a new predictive model for the critical rupture thickness (H_{cr}) of a foam film. The model has been developed on the base of the capillary wave model and the extended Derjaguin-Landau-Verwey-Overbeek (DLVO) theory. By considering the contribution from hydrophobic disjoining pressure, this model can predict H_{cr} reasonable well.

Chapter 3 describes a new model for predicting the bubble-coarsening in a dynamic foam as a function of aeration rate, foam height, and surface tension (frother dosage). This foam model is on the base of the H_{cr} model developed in Chapter 2. The model has been validated using a foam column equipped with a high-speed camera.

Chapter 4 presents a new first principle froth model for predicting the bubble-coarsening in a froth (3-phase foam) as a function of aeration rate, froth height, surface tension (frother dosage), particle hydrophobicity (collector dosage), and particle size. This chapter is focused on the effect of particle hydrophobicity on bubble-coarsening. This model has been validated in a series of flotation tests using monosized spheres of varying hydrophobicity.

Chapter 5 is the same as Chapter 4 except that it is mainly focused on the effect of particle size on bubble-coarsening. The froth model developed in Chapter 4 is capable of predicting the bubble-coarsening as a function of particle size. The model predictions are in good agreement with the changes in bubble sizes measured experimentally in the presence of different sizes of particles.

Chapter 6 summarizes the key findings and accomplishments presented in the foregoing chapters and suggests future research topics.

References

[1] Laskowski, J., The relationship between floatability and hydrophobicity, in *Advances in mineral processing: A half century of progress in application of theory and practive*. 1986.

[2] Seaman, D.R., E.V. Manlapig, and J.P. Franzidis, Selective transport of attached particles across the pulp–froth interface. *Minerals Engineering*, 2006. **19**(6–8): p. 841-851.

[3] George, P., A. Nguyen, and G. Jameson, Assessment of true flotation and entrainment in the flotation of submicron particles by fine bubbles. *Minerals Engineering*, 2004. **17**(7): p. 847-853.

[4] Hinze, J.O., Fundamentals of the hydrodynamic mechanism of splitting in dispersion processes. *AIChE Journal*, 1955. **1**(3): p. 289-295.

[5] Batchelor, G. Pressure fluctuations in isotropic turbulence. in *Mathematical Proceedings of the Cambridge Philosophical Society*. 1951. Cambridge Univ Press.

[6] Schulze, H.-J., Physico-Chemical Elementary Processes in Flotation: Analysis from the Point of View of Colloid Science Including Process Engineering Considerations 1984: Elsevier Science Ltd

[7] Schubert, H., On the turbulence-controlled microprocesses in flotation machines. *International Journal of Mineral Processing*, 1999. **56**(1–4): p. 257-276.

[8] Lewis, D. and J. Davidson, Bubble splitting in shear flow. *Transactions of the Institution of Chemical Engineers*, 1982. **60**(5): p. 283-291.

[9] Parthasarathy, R., G. Jameson, and N. Ahmed, Bubble breakup in stirred vessels: Predicting the Sauter mean diameter. *Chemical engineering research & design*, 1991. **69**(A4): p. 295-301.

[10] Wallis, G.B., One-dimensional two-phase flow. 1962: McGraw Hill.

[11] Richardson, J.F. and W.N. Zaki, The sedimentation of a suspension of uniform spheres under conditions of viscous flow. *Chemical Engineering Science*, 1954. **3**(2): p. 65-73.

[12] Schiller, L. and A. Naumann, A drag coefficient correlation. *Vdi Zeitung*, 1935. **77**(318): p. 51.

[13] Clift, R., J.R. Grace, and M.E. Weber, Bubbles, drops, and particles. 2005: Courier Corporation.

[14] Banisi, S. and J.A. Finch, Reconciliation of Bubble-Size Estimation Methods Using Drift Flux Analysis. *Minerals Engineering*, 1994. **7**(12): p. 1555-1559.

[15] Ityokumbul, M., A. Salama, and A. Al Taweel, Estimation of bubble size in flotation columns. *Minerals engineering*, 1995. **8**(1): p. 77-89.

[16] Stevenson, P., C. Stevanov, and G. Jameson, Liquid overflow from a column of rising aqueous froth. *Minerals engineering*, 2003. **16**(11): p. 1045-1053.

[17] Neethling, S. and J. Cilliers, A visual kinematic model of flowing foams incorporating coalescence. *Powder technology*, 1999. **101**(3): p. 249-256.

[18] Murphy, D.G., W. Zimmerman, and E.T. Woodburn, Kinematic model of bubble motion in a flotation froth. *Powder Technology*, 1996. **87**(1): p. 3-12.

[19] Fuerstenau, M.C., G.J. Jameson, and R.-H. Yoon, Froth flotation: a century of innovation. 2007: SME.

[20] Verbist, G., D. Weaire, and A.M. Kraynik, The foam drainage equation. *Journal of Physics: Condensed Matter*, 1996. **8**(21): p. 3715-3731.

[21] Koehler, S.A., S. Hilgenfeldt, and H.A. Stone, Liquid Flow through Aqueous Foams: The Node-Dominated Foam Drainage Equation. *Physical Review Letters*, 1999. **82**(21): p. 4232-4235.

[22] Koehler, S.A., S. Hilgenfeldt, and H.A. Stone, A Generalized View of Foam Drainage: Experiment and Theory. *Langmuir*, 2000. **16**(15): p. 6327-6341.

[23] Durand, M., G. Martinoty, and D. Langevin, Liquid flow through aqueous foams: From the plateau border-dominated regime to the node-dominated regime. *Physical Review E*, 1999. **60**(6): p. R6307-R6308.

[24] Saint-Jalmes, A., M.U. Vera, and D.J. Durian, Uniform foam production by turbulent mixing: new results on free drainage vs. liquid content. *The European Physical Journal B - Condensed Matter and Complex Systems*, 1999. **12**(1): p. 67-73.

[25] Reynolds, O., On the Theory of Lubrication and Its Application to Mr. Beauchamp Tower's Experiments, Including an Experimental Determination of the Viscosity of Olive Oil. *Proceedings of the Royal Society of London*, 1886. **40**(242-245): p. 191-203.

[26] Yoon, R.-H. and L. Mao, Application of extended DLVO theory, IV: derivation of flotation rate equation from first principles. *Journal of Colloid and Interface Science*, 1996. **181**(2): p. 613-626.

[27] Iglesias, E., et al., A new method to estimate the stability of short-life foams. *Colloids and Surfaces A: Physicochemical and Engineering Aspects*, 1995. **98**(1-2): p. 167-174.

[28] Zanin, M., et al., Quantifying contributions to froth stability in porphyry copper plants. *International Journal of Mineral Processing*, 2009. **91**(1-2): p. 19-27.

[29] Bikerman, J.J., Foams. 1973: Springer-Verlag New York.

[30] Barbian, N., et al., The froth stability column: Linking froth stability and flotation performance. *Minerals Engineering*, 2005. **18**(3): p. 317-324.

[31] Moys, M.H., Residence time distributions and mass transport in the froth phase of the flotation process. *International Journal of Mineral Processing*, 1984. **13**(2): p. 117-142.

[32] Barbian, N., et al., Froth imaging, air recovery and bubble loading to describe flotation bank performance. *International Journal of Mineral Processing*, 2007. **84**(1): p. 81-88.

[33] Qu, X., L. Wang, and A.V. Nguyen, Correlation of air recovery with froth stability and separation efficiency in coal flotation. *Minerals Engineering*, 2013. **41**: p. 25-30.

[34] Ata, S., N. Ahmed, and G.J. Jameson, A study of bubble coalescence in flotation froths. *International Journal of Mineral Processing*, 2003. **72**(1–4): p. 255-266.

[35] Laplante, A.R., J.M. Toguri, and H.W. Smith, The effect of air flow rate on the kinetics of flotation. Part 1: The transfer of material from the slurry to the froth. *International Journal of Mineral Processing*, 1983. **11**(3): p. 203-219.

[36] Hu, S., P. Ofori, and B. Firth, Monitoring of froth stability using electrical impedance spectroscopy. *International Journal of Mineral Processing*, 2009. **92**(1–2): p. 15-21.

[37] Sutherland, K.L., Physical Chemistry of Flotation. XI. Kinetics of the Flotation Process. *The Journal of Physical and Colloid Chemistry*, 1948. **52**(2): p. 394-425.

[38] Soni, G. and R.-H. Yoon. Validation of a first principles flotation model. in *The 27th International Mineral Processing Congress* 2014. Santiago, Chile.

[39] Lee, C.-H., L. Erickson, and L. Glasgow, Bubble breakup and coalescence in turbulent gas-liquid dispersions. *Chemical Engineering Communications*, 1987. **59**(1-6): p. 65-84.

[40] Luttrell, G.H. and R.H. Yoon, A hydrodynamic model for bubble—particle attachment. *Journal of Colloid and Interface Science*, 1992. **154**(1): p. 129-137.

[41] Yoon, R., Hydrodynamic and surface forces in bubble-particle interactions. *INDUSTRIE MINERALE MINES ET CARRIERES LES TECHNIQUES*, 1992: p. 74-74.

[42] Maachar, A. and G. Dobby, Measurement of feed water recovery and entrainment solids recovery in flotation columns. *Canadian metallurgical quarterly*, 1992. **31**(3): p. 167-172.

[43] Gorain, B., et al., The effect of froth residence time on the kinetics of flotation. *Minerals Engineering*, 1998. **11**(7): p. 627-638.

Chapter 2. Prediction of the Critical Rupture Thickness of Foam Films

ABSTRACT

In flotation, a froth recovery depends critically on bubble-coarsening. The bubble-coarsening occurs when a thin liquid film (TLF) confined between two bubbles breaks. As a precursor to developing a model that can predict the bubble-coarsening in a froth (or foam), we have developed a model for predicting the critical film thickness (H_{cr}) at which a foam film ruptures. The model has been derived by considering the film drainage due to viscous film thinning and the capillary wave motion at air/water interfaces. This approach is based on the premise that if the disjoining pressure (Π) created by surface forces in the TLF is negative (attractive), both the film drainage and the capillary wave motion accelerate and consequently the TLF ruptures. The model predictions are consistent with the H_{cr} values measured experimentally. It has been found in the present study that at a relatively low frother (or surfactant) concentration, corrugation of air/water interfaces grow faster in amplitude and thereby the TLF ruptures at a larger film thickness. At a high frother concentration, hydrophobic force is dampened, causing the grown of fluctuation to decrease and hence causing the H_{cr} to decrease.

2.1 Introduction

In froth (or foam) phase, two air bubbles are in close contact with each other and a thin liquid film (TLF) is formed in between. As the bubbles rise along the height of a froth phase, the water in the TLF drains initially due to the capillary pressure (p_c) created from the changes in curvature. As the film thickness (H) reaches approximately 150-200 nm, the process begins to slow down due to the repulsive electrical double-layer forces between the two air/water interfaces facing each other. When the p_c becomes equal in magnitude to the disjoining pressure (Π_e) due to double-layer repulsion, the film thinning stops at an equilibrium film thickness (H_e). If there exists an attractive force in the TLF, the film thinning continues and the film ruptures and the two bubbles become one at a critical film rupture thickness (H_{cr}).

Scheludko [1, 2] was the first to present a theoretical model to predict H_{cr}. The model was derived based on the premise that the air/water interfaces of TLFs are thermally fluctuated and that the TLF becomes unstable and ruptures if the negative disjoining pressure gradient along film thickness H exceeds the capillary pressure gradient along H,

$$H_{cr} = \frac{A_{232}\lambda^2}{128\pi} \tag{2.1}$$

where A_{232} is the Hamaker constant of water between two air bubbles and λ is the wavelength of the surface fluctuations. The primary limitation of this model is that the value of λ is undefined.

Based on Scheludko's theory [1, 2], Vrij and his co-workers [3-5] developed a more advanced H_{cr} model in that not only the model defined the values of λ by calculating the Gibbs energy change associated with fluctuation growth, but also it included the role of film drainage in determining film stability. The following is the H_{cr} model developed by the authors,

$$H_{cr} = 0.2077\sqrt{\frac{A_{232}^{\ 2}R_f^{\ 2}}{\gamma p_c}} \tag{2.2}$$

where R_f is the radius of contact area and γ is the surface tension. Unfortunately, Eq. (2.2) fails to predict H_{cr} accurately, particularly at low surfactant (frother) concentrations, where air bubbles become more hydrophobic [6]. The failure of Eq. (2.2) may arise from the fact that at the time the

classical Derjaguin-Landau-Verwey-Overbeek (DLVO) theory was developed and no one knew that air bubbles in water are hydrophobic. Further, no one thought about the possibility of hydrophobic force playing a role in foam stability. Recently, it has shown that the hydrophobic force is also present in foam films in addition to the van der Waals force, and that the former is larger than the latter at low frother concentrations [7, 8].

More recently, Do [9] modified Eq. (2.2) by considering the possibility that the TLF between air bubbles drains faster due to slip on the hydrophobic air/water interfaces. In addition, he introduced the variation of film thinning velocity from the difference between the wavy film radius and the flat film radius by considering the geometric relation,

$$H_{cr} = \left(1 + 8\sqrt{\frac{4K_{232}}{A_{232}}}\right)^{\frac{1}{3}} \left(\frac{1}{\pi}\sqrt{4\pi^2(\eta/\lambda)^2 + 1} \cdot \int_0^{\pi} \sqrt{1 - \left(\frac{4\pi^2(\eta/\lambda)^2}{4\pi^2(\eta/\lambda)^2 + 1}\right)^2 \sin^2\theta}\, d\theta\right)^{\frac{2}{3}} \left\{0.207\left(\frac{A_{232}^{\ 2} R_f^{\ 2}}{\gamma p_c}\right)^{1/7}\right\} \tag{2.3}$$

where K_{232} is the hydrophobic force constant of water between two air bubbles, η is the amplitude of the wave at the air/water interfaces in a foam film, and λ is the wavelength. However, in this model, the possibility that the amplitude of capillary waves grows faster in the presence of stronger attractive hydrophobic force was not considered. Moreover, this model describes the film thinning process using the classical DLVO theory, which neglects the contributions from the hydrophobic force. Also, the fact that value of η/λ in Eq. (2.3) needs to be empirically determined is problematic.

In the present work, we have derived a model for predicting H_{cr} by incorporating the hydrophobic force in the capillary wave model developed by Vrij. This new model has been developed by considering the effects of hydrophobic force on the film drainage and the wave motion.

2.2 Model Incorporating Hydrophobic Force

The capillary wave model developed by Vrij *et al*. [3-5] described the film thinning process and the capillary wave motion to predict the critical rupture thickness (H_{cr}) of a foam film. In

Section 2.2, we incorporate the hydrophobic force into the Vrij *el al*.'s model to predict H_{cr} at low frother concentrations.

2.2.1 Film Thinning

The kinetics of thinning of a horizontal thin liquid film (TLF) between two air bubbles can be described in view of the Reynolds lubrication equation,

$$\frac{dH}{dt_{drain}} = -\frac{2H^3 p}{3\mu R_f^2} \tag{2.4}$$

where H is the TLF thickness, t_{drain} the drainage time, μ the dynamic viscosity, R_f the film radius, and p the driving force for TLF thinning. In Eq. (2.4), the driving force p is given by the expression,

$$p = p_c - \Pi \tag{2.5}$$

where p_c is the capillary pressure and Π is the disjoining pressure. The capillary pressure p_c is given by,

$$p_c = \frac{2\gamma}{R} \tag{2.6}$$

where R is the bubble radius and γ is the surface tension of water. In calculating Π, in the original Vrij's model, only the contributions from the electrostatic and van der Waals forces are included, according to the classical DLVO theory. However, in the present study, according the extended DLVO theory, the contribution from the hydrophobic force is considered additionally,

$$\Pi = \Pi_{el} + \Pi_{vw} + \Pi_{hp} = 64 C_{el} R_2 T \tanh^2\left(\frac{e\psi_s}{4kT}\right)\exp(-\kappa H) - \frac{A_{232}}{6\pi H^3} - \frac{K_{232}}{6\pi H^3} \tag{2.7}$$

where Π_{el}, Π_{vw}, and Π_{hp} represent the contribution from the electrostatic, van der Waals, hydrophobic forces, respectively, C_{el} the electrolyte concentration, R_2 the gas constant, T the absolute temperature, e the electronic charge, ψ_s the surface potential at the air/water interfaces, k the Boltzmann's constant, and κ the reciprocal Debye length.

2.2.2 Growth of Surface Fluctuation

Figure 2.1 shows one of corrugating components of air/water interfaces of the TLF due to thermal motion. Corrugation due to thermal motion increases the surface area of the air/water interface and hence the free energy. However, the corrugation causes the film thickness at the valleys to decrease as the inverse curve of the film thickness due to the van der Waals attraction, which in turn causes the free energy to decrease and the film thinning kinetics to accelerate. By considering film thinning due to the growth of fluctuation, Vrij estimated the time it takes for a film to thin due to fluctuation (t_{fluct}) as follows,

$$t_{\text{fluct}} = -24 f \mu \gamma H^{-3} \left(\left. \frac{d\Pi}{dH} \right|_{H=H} \right)^{-2} \tag{2.8}$$

where f is the adjustable parameter. $f = 6$ was assumed in the original model. We also use the same value in the present study. In using Eq. (2.9), we recognize the contributions from Π_{hp} in addition to Π_{el} and Π_{vw}, as presented in Eq. (2.7).

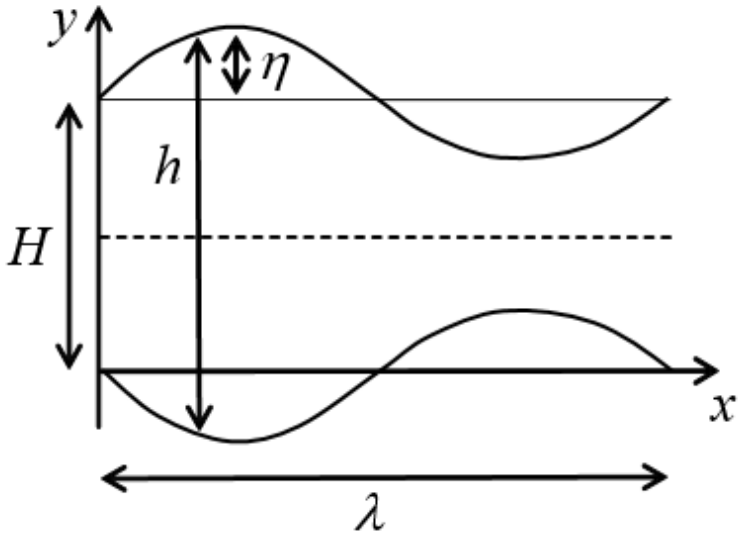

Figure 2.1 One of the capillary wavy patterns at the facing air/water interfaces confining the foam film with the average film thickness H and the local thickness h. λ represents the wavelength and η represents the amplitude of the wave motion.

2.2.3 Calculation of H_{cr}

Vrij assumed that a TLF ruptures when two surfaces touch each other. This condition can be represented by the following relation,

$$\left.\frac{dt_{\text{drain}}}{dH}\right|_{H=H_{\text{m}}} + \left.\frac{dt_{\text{fluct}}}{dH}\right|_{H=H_{\text{m}}} = 0 \tag{2.9}$$

where H_{m} is the mean film thickness at which satisfies the above requirement.

Substituting Eqs. (2.4) and (2.8) into Eq. (2.9), one can obtain H_{m} as follows,

$$144\gamma\left\{3H_{\text{m}}^{-4}\left(\left.\frac{\partial\Pi}{\partial H}\right|_{H=H_{\text{m}}}\right)^{-2} - 2H_{\text{m}}^{-3}\left(\left.\frac{\partial\Pi}{\partial H}\right|_{H=H_{\text{m}}}\right)^{-3}\left.\frac{\partial^2\Pi}{\partial H^2}\right|_{H=H_{\text{m}}}\right\} - \frac{3H_{\text{m}}^{-3}R_{\text{f}}^{2}}{2(p_{\text{c}}-\Pi)} = 0 \tag{2.10}$$

Vrij recognized the fact that the critical film rupture thickness (H_{cr}) may be slightly smaller than H_{m} due to the fact that the viscous film thinning continues while the wave is growing. Accordingly, he suggested the following relation,

$$H_{\text{cr}} = 0.845H_{\text{m}} \tag{2.11}$$

2.3 Model Validation

To validate the model developed in the present work, the model predictions were compared with experimental H_{cr} values reported by Wang [10]. Wang measured H_{cr} values of the foam films stabilized with methyl isobutyl carbinol (MIBC) in the presence of 0.1 M NaCl, where $\Pi_{\text{el}} \approx 0$ due to double-layer compression. In his study, foam films of small film radius ($R_{\text{f}} < 50$ μm) were tested to avoid dimple formation.

In the present work, H_{cr} values have been predicted from Eqs. (2.10) and (2.11). In using them, the values of K_{232} were obtained from Wang and Yoon's results [11]. They determined the K_{232} values at different concentrations of MIBC by fitting experimental film thinning data to the Reynolds equation coupled with the extended DLVO theory. The values of A_{232}, γ, and ψ_{s} were used as reported by Wang [10], Comley *et al*. [12], and Srinivas *et al*. [13], respectively. Only the

values of T = 298 K and κ^{-1}= 30 nm were assumed. C_{el} was simply predicted from κ using the relation, $C_{el} = 0.092\kappa^2 = 10^{-4}$ mole/liter [14].

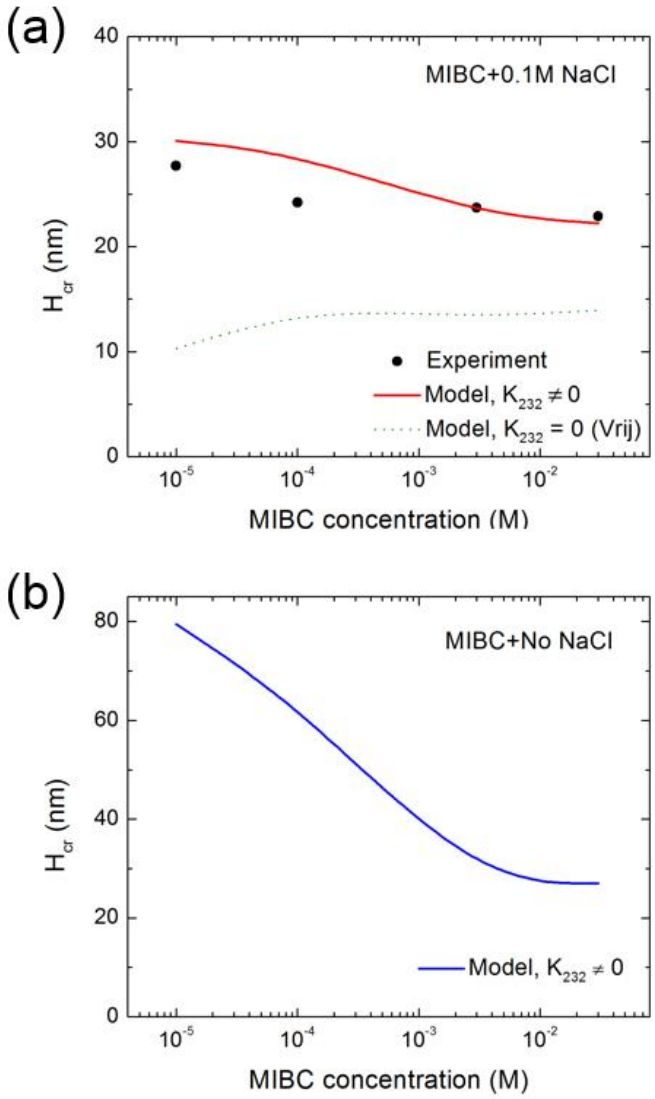

Figure 2.2 Plots of the critical film rupture thicknesses (H_{cr}) predicted using the model, Eqs. (2.10) and (2.11), at varying MIBC concentrations. In Figure 2.2 (a), the red line represents the predictions by considering contributions from the hydrophobic disjoining pressure (Π_{hp}) at 0.1 M NaCl, while the points represent the experimental H_{cr} values. The green dotted line below represents the model predictions at Π_{hp} = 0 and 0.1 M NaCl. In Figure 2.2 (b), the blue line represents the predictions with $\Pi_{hp} \neq 0$ in the absence of NaCl. The values of Π_{hp} have been obtained from K_{232} values presented by Wang and Yoon (2009).

As shown in Figure 2.2 (a), there is an excellent agreement between the experimental (filled circles) and the model predictions (line). The model include the contributions from the hydrophobic disjoining pressure, which is the reason for the excellent fit between theory and experiment. If the hydrophobic force is not considered, the model predicts substantially smaller H_{cr} values as shown by the bottom most (green) line in Figure 2.2 (a).

Figure 2.2 (b) shows the H_{cr} values (the topmost blue line) predicted using Eqs. (2.10) and (2.11) at different concentrations of MIBC in the absence of NaCl. As shown, the model gives substantially higher H_{cr} values than those obtained at 0.1 M NaCl, which can be attributed to the fact that the hydrophobic force (or K_{232}) increases with decreasing NaCl concentration. It is believed that the hydrophobic force originating from the cohesive energy of water is compromised in the presence of electrolytes.

2.4 Summary and Conclusions

In this study, we have developed a predictive model for the critical rupture thickness (H_{cr}) of foam films. This new model has been derived on the basis of the capillary wave model and the extended DLVO theory, which includes the contributions from the attractive hydrophobic force. It has been found in the present work that at lower frother concentration, where the hydrophobic force is stronger, a foam film ruptures at higher film thickness due to faster growth rate of surface wave. It has also been found that H_{cr} decreases with increasing frother concentration, which may be attributed to a decrease in the hydrophobic force, resulting in retarded wave motion. As is well known, bubble-coarsening in a froth (or foam) occurs when thin liquid film confined between two bubbles ruptures. This H_{cr} model will be useful for developing a model describing bubble-coarsening phenomena in a froth.

References

[1] Scheludko, A., Sur certaines particularités des lames mousseuses. *Proc. Konikl. Ned. Akad. Wet. B*, 1962. **65**: p. 86-99.

[2] Sheludko, A., Thin liquid films. *Advances in Colloid and Interface Science*, 1967. **1**(4): p. 391-464.

[3] Vrij, A., Possible mechanism for the spontaneous rupture of thin, free liquid films. *Discussions of the Faraday Society*, 1966. **42**(0): p. 23-33.

[4] Vrij, A. and J.T.G. Overbeek, Rupture of thin liquid films due to spontaneous fluctuations in thickness. *Journal of the American Chemical Society*, 1968. **90**(12): p. 3074-3078.

[5] Donners, W.A.B. and A. Vrij, The critical thickness of thin free liquid films. *Colloid and Polymer Science*, 1978. **256**(8): p. 804-813.

[6] Wang, L. and R.-H. Yoon, Effects of surface forces and film elasticity on foam stability. *International Journal of Mineral Processing*, 2008. **85**(4): p. 101-110.

[7] Wang, L. and R.-H. Yoon, Role of hydrophobic force in the thinning of foam films containing a nonionic surfactant. *Colloids and Surfaces A: Physicochemical and Engineering Aspects*, 2006. **282**: p. 84-91.

[8] Yoon, R.-H. and B.S. Aksoy, Hydrophobic Forces in Thin Water Films Stabilized by Dodecylammonium Chloride. *Journal of Colloid and Interface Science*, 1999. **211**(1): p. 1-10.

[9] Do, H. Development of a Turbulent Flotation Model from First Principles. 2010, Virginia Polytechnic Institute and State University. PhD thesis.

[10] Wang, L. Inter-bubble attractions in aqueous solutions of flotation frothers. in *SME Annual Meeting*. 2011. Denver, CO, United States.

[11] Wang, L. and R.-H. Yoon. Effect of pH and electrolyte on the stability of surfactant-free foam films. in *SME Annual Meeting*. 2009. Denver, CO, United States: SME.

[12] Comley, B.A., et al., Frother characterisation using dynamic surface tension measurements. *International Journal of Mineral Processing*, 2002. **64**(2-3): p. 81-100.

[13] Srinivas, A. and P. Ghosh, Coalescence of bubbles in aqueous alcohol solutions. *Industrial & Engineering Chemistry Research*, 2011. **51**(2): p. 795-806.

[14] Butt, H.-J., Measuring electrostatic, van der Waals, and hydration forces in electrolyte solutions with an atomic force microscope. *Biophysical Journal*, 1991. **60**(6): p. 1438.

Chapter 3. Development of a Bubble-Coarsening Model in a Dynamic Foam

ABSTRACT

In a flotation froth (and foam), air bubbles become larger due to coalescence, causing bubble size to increase, bubble surface area to decrease, and hence causing less hydrophobic particles to drop off to the pulp phase below. Thus, bubble coarsening provides an important mechanism by which product grades are increased. On the other hand, excessive bubble coarsening results in low recoveries. In the present work, a model describing the process of bubbles becoming coarser in a foam as they rise to the top by deriving a mathematical relation between the Plateau border area, which controls liquid drainage rate, and the lamella film thickness, which controls bubble-coalescence rate. The model developed in the present work can predict the bubble size ratio between the top and bottom of a foam as functions of aeration rate, foam height, and surface tension (frother dosage). The model predictions are in good agreement with the changes in bubble sizes measured using a high-speed camera.

3.1 Introduction

Froth flotation is the most widely used method of upgrading pulverized ores in the minerals industry. In this process, hydrophobic particles selectively attach to air bubbles in a pulp phase, forming particle-bubble aggregates, which rise upward due to reduced buoyancy and form a froth phase. In the froth phase, the bubbles coalesce with each other and become larger as they rise. As the bubbles become larger, the bubble surface area decreases, thereby restricting the number of hydrophobic particles that can be carried upward and subsequently flow into a launder. Therefore, in flotation modelling, froth recovery due to attachment (R_f^a) is given as a function of surface area as follows,

$$R_f^{\ a} = R_{\max} \exp(-\alpha \tau_{f,p}) \tag{3.1}$$

where $R_{\max}$ is the maximum froth recovery factor representing the carrying capacity limit, α is a fitting parameter, $\tau_{f,p}$ is the retention time of particles in the froth phase. In using Eq. (3.1), $R_{\max}$ can be expressed as follows,

$$R_{\max} = \frac{S_t}{S_b} = \frac{6V_g / d_{2,t}}{6V_g / d_{2,b}} = \frac{d_{2,b}}{d_{2,t}} \tag{3.2}$$

where S_t and S_b is the bubble surface area flux at the top and base of a froth, respectively, $d_{2,t}$ and $d_{2,b}$ are the corresponding bubble sizes, and V_g is the superficial gas velocity.

On the other hand, the bubble coarsening helps increase the grade of a froth product, as less hydrophobic particles selectively drop off the coarsening bubbles [1]. Thus, it is of critical importance to understand and control bubble coarsening in the froth phase. Despite of its significance, the bubble coarsening in the froth phase has not been studied widely until now, due to the structural complexity and the opaqueness of a mineral-coated froth. Recently, Barbian *et al*. [2, 3] conducted dynamic froth stability tests in a flotation column and observed experimentally that increasing gas flow rate benefits the froth stability. Tao *et al*. [4] found that lowering froth height help increase froth stability by measuring the water recovery in a flotation column, as a measure of froth stability. Wang and Yoon [5] reported that the disjoining pressure (Π) created by surface forces in the lamella films controls the foam stability. More recently, the first theoretical

model that can predict bubble-coarsening or bubble size distribution in foam has been developed by coupling a liquid drainage model with a population balance model [6]. The authors employed a single fitting parameter associated with the frequency of film rupture and assumed that it is a function of fluid viscosity and surface chemistry. The model was validated by a single experiment in a surfactant solution of a fixed concentration.

In the present work, we have developed a bubble-coarsening model that can predict the bubble coarsening ($d_{2,t}/d_{2,b}$) by deriving a mathematical relation between the Plateau border area, which controls liquid drainage rate, and the lamella film thickness, which controls bubble-coalescence rate. The model is based on the capillary wave model [7, 8], in which air/water interfaces in form films oscillate due to thermal motions such that the instantaneous thickness of a foam film becomes smaller than the average thickness. Because the van der Waals force varies as H^{-3}, where H is film thickness, a small change in film thickness can greatly decrease the free energy of film rupture. The bubble-coarsening model developed in the present work is also based on the recognition that the air bubbles dispersed in water are hydrophobic [9], which will in turn increase drainage rate and hence facilitate bubble coarsening.

The objective of the present work is to develop a model for predicting bubble-coarsening in foams and verify it in experiment. We have measured the bubble size ratio ($d_{2,t}/d_{2,b}$) of a foam stabilized with Methyl isobutyl carbinol (MIBC) at varying frother concentrations, foam heights, and gas rates.

3.2 Model Development

As is well known, bubbles become larger as they rise along the height of a foam mainly due to bubble coalescence. The bubble coarsening can be controlled by frother addition. Thermodynamically, frother decrease the free energy of bubble coalescence, *i.e.*, $\Delta G_c = -2\gamma$, by decreasing the surface tension, γ, at the air/water interface. Kinetically, frother decreases the rate of film thinning by decreasing capillary pressure, $\Delta P = 2\gamma/R$, where R is the Plateau boarder radius. It has been shown also that frother dampens the hydrophobic force in the lamellar (or foam) films, which has been shown to accelerate the rate of film thinning at film thicknesses (H) below approximately 250 nm [10]. As film thinning continues, H reaches a critical thickness (H_{cr}), where

the film ruptures catastrophically. Thus, it is necessary to model the kinetics of film thinning at the Plateau border and predict H_{cr} for developing a mathematical for bubble coarsening.

In a dry foam, when two bubbles face each other, they form a lamella, a thin liquid film (TLF). When three TLFs meet together, they form a Plateau border (PB). A PB is a channel in which liquid flows though. Four PB forms a vertex, where liquid meet together. In the absence of external water supply to a foam (e.g. wash water in column flotation), the base of the foam is relatively wet, whereas the top of the foam is dry due to the downward liquid drainage in the foam phase. In general, water amount in the TLF is small compared to the same in the PB, especially in the case of dry area. Therefore, for the modeling purpose of a foam or liquid drainage in the foam, most studies have been neglected water in the TLF.

3.2.1 Foam Drainage

Now consider liquid drainage in a PB in the vertical direction. On the base of consideration of the force balance and the mass conservation, the drainage of liquid through a PB can be derived as follows [11, 12],

$$U = \frac{1}{\mu}\left(\rho g A - \gamma \frac{1}{\sqrt{A}} \frac{\partial A}{\partial x}\right) \tag{3.3}$$

where U is the drainage rate; g is the gravitational acceleration; μ, ρ, and γ are the kinematic viscosity, density, and surface tension of water, respectively; A is the cross-sectional area of the Plateau border (PB), and x is the distance from the top of a foam. For the force balance, the balance between gravitational force (forcing downward), capillary force (forcing upward), and viscous force (forcing opposing direction of the liquid flow) is considered. In terms of viscous loss, there are two controversial hypotheses.

3.2.2 Steady State

At a steady state, the downward liquid drainage velocity (U) is equal to the upward superficial gas velocity ($-V_g$),

$$U = -V_g \tag{3.4}$$

Combining Eqs. (3.3) and (3.4) and then integrating from the top to the bottom of a foam, one obtains,

$$\sqrt{A_t} = \sqrt{\frac{V_g \mu}{\rho g}} \tan\left[\tan^{-1}\left(\sqrt{\frac{\rho g A_b}{V_g \mu}} \right) \right] - \frac{h_f}{2} \frac{\sqrt{\rho g \mu V_g}}{\gamma} \tag{3.5}$$

where A_t is the PB area at the top of a foam and A_b is the same at the bottom, and h_f is the foam height.

3.2.3 Bubble Coarsening Model

In a dry foam, each PB is formed by the intersection of three lamellar films, and each corner of the surrounding polyhedron is the intersection of four PBs. Thus, it would be reasonable to assume that the number of PBs (N_{pb}) is proportional to the number of bubbles, which can be calculated by dividing the cross-sectional area (S) of a foam (or froth) column by bubble diameter, *i.e.*, $4S/\pi d^2$. One can then write the following relation,

$$\frac{N_{pb,t}}{N_{pb,b}} = \frac{4S/\pi {d_{2,t}}^2}{4S/\pi {d_{2,b}}^2} = \left(\frac{d_{2,b}}{d_{2,t}} \right)^2 \tag{3.6}$$

where $N_{pb,t}$ and $N_{pb,b}$ are the PB numbers at the top and bottom of a foam, respectively, and $d_{2,t}$ and $d_{2,b}$ are the corresponding bubble sizes.

As a foam drains, A becomes smaller, or the foam becomes drier. As a foam becomes drier, the thickness (H) of the lamella films will also become thinner. As H becomes thinner, there will be a point where, a lamellar film will rupture catastrophically, which is referred to as critical rupture thickness (H_{cr}). Likewise, it may be reasonable to assume that bubbles begin to coalesce when A reaches A_{cr}, provided that there is a mathematical relation between A_{cr} and H_{cr}. As bubbles coalesce, N_{pb} will decrease. In the present work, N_{pb} may be related to A_{cr} as follows [11],

$$N_{pb} = N_0 \exp\left(-C \sqrt{\frac{A_{cr}}{A}} \right) \tag{3.7}$$

where N_0 is the number of PBs at the base of a foam, and C is an adjustable parameter. Eq. (3.7) suggests that N_{pb} increases exponentially with the square root of A_{cr}, which can be related to H_{cr} analytically as will be shown later.

Substituting Eq. (3.7) into Eq. (3.6), one obtains the following relation,

$$\frac{d_{2,b}}{d_{2,t}} = \sqrt{\exp C\sqrt{A_{cr}}\left(\frac{1}{\sqrt{A_b}} - \frac{1}{\sqrt{A_t}}\right)} \tag{3.8}$$

which will allow prediction of bubble size ratio (or bubble coarsening) if the values of A_b, A_t and A_{cr} are known.

According to Eq. (3.5), one can determine the value of A_t if A_b is known. One can determine A_b by considering the geometrical relationships between bubble size, lamellar film thickness, and Plateau border radius [13, 14],

$$\sqrt{A_b} = \sqrt{0.124(d_{2,b}\sqrt{\varepsilon_b})^2 + 1.52 d_{2,b}\sqrt{\varepsilon_b} H_b} \tag{3.9}$$

where $d_{2,b}$ is the bubble size at the base of a foam (or froth), which may be considered the same as the bubble size in the pulp phase; ε_b is the liquid fraction at the base of the foam under consideration; and H_b is the lamella film thickness at the base.

One can determine $d_{2,b}$ using a simple bubble generation model [15],

$$d_{2,b} = \left(\frac{2.11\gamma}{\rho\varepsilon_{bg}^{0.66}}\right)^{0.6} \tag{3.10}$$

where ε_{bg} is the energy dissipation rate in the bubble generation zone of a flotation cell.

In using Eq. (3.9), one can obtain ε_b using a drift-flux analysis [16],

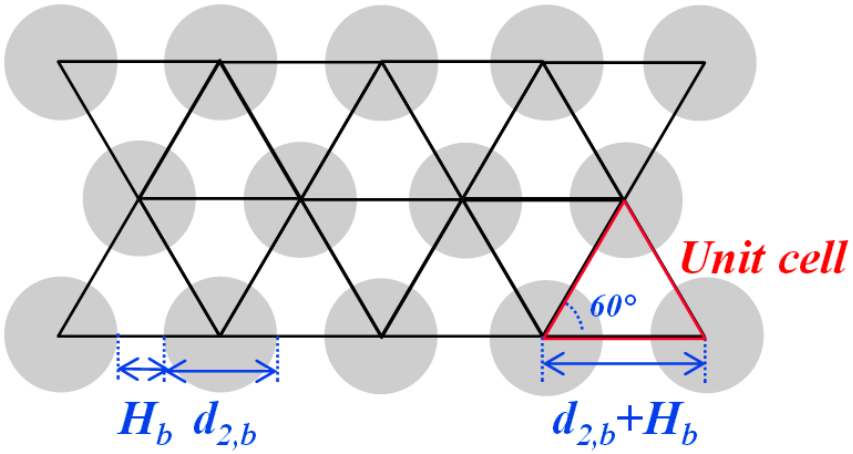

Figure 3.1 A model for the unit cell of the bubbles packed at the base of a foam (or froth).

$$U_{slip} = \frac{V_g}{1-\varepsilon_b} + \frac{V_l}{\varepsilon_b} = \frac{g d_2 \varepsilon_b^{\,2} \rho}{18\mu(1+0.15\mathrm{Re}^{0.687})} \tag{3.11}$$

where U_{slip} is the slip velocity of bubbles, V_g and V_l are the superficial velocities of gas and liquid, respectively, and Re is the Reynolds number.

By the geometrical considerations depicted in Figure 3.1, the H_b of Eq. (3.9) was determined combining Eqs. (3.12) and (3.13),

$$\varepsilon_b = 1 - \frac{\frac{4}{3}\pi\left(\frac{d_{2,b}}{2}\right)^3 N_{2,b}}{S(d_{2,b}+H_b)} \tag{3.12}$$

where $N_{2,b}$ is the number of bubbles of size $d_{2,b}$ in a foam column of cross-sectional area of S. Assuming that the bubbles at the base are spherical and form a two-dimensional monolayer as depicted in Figure 3.1, one calculate $N_{2,b}$ as follows,

$$N_{2,b} = 2N_{t,b} = 2\left(\frac{S}{0.5(d_{2,b}+H_b)^2\cos 30°}\right) \tag{3.13}$$

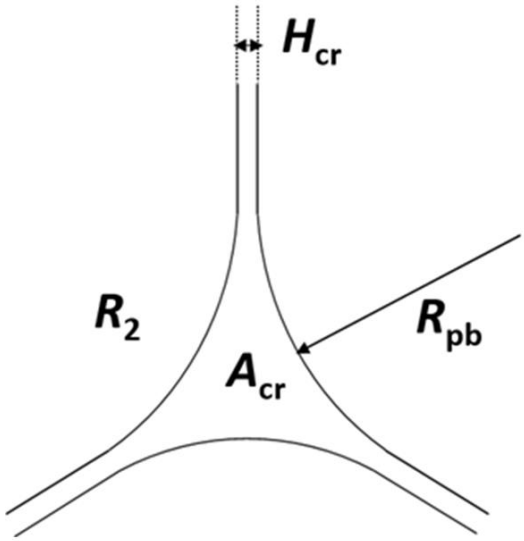

Figure 3.2 A geometrical relationship between bubble size (R_2), Plateau boarder radius (R_{pb}), the critical Plateau boarder area (A_{cr}), and the critical lamella film thickness (H_{cr}) in a foam.

Since each triangular unit contains one half of a bubble, $N_{2,b}$ is twice the number of the triangles at the base ($N_{t,b}$), which can be determined simply by dividing S with the area of a triangle

In calculating the bubble size ratio using Eq. (3.8), it is also necessary to know the value of A_{cr}. In the present work, the values of A_{cr} were calculated from those of H_{cr} based on the geometric relation between A and H [14], as shown in Figure 3.2.

$$A_{cr} = (\sqrt{3} - \frac{\pi}{2}) R_{pb}{}^2 + \sqrt{3} R_{pb} H_{cr} \tag{3.14}$$

where R_{pb} is the radius of curvature of PB. In Eq. (3.14), H_{cr} can be determined from the methodology presented in Chapter 2.

3.3 Experimental

3.3.1 Materials

In this study, the model presented in the foregoing section was validated using a specially designed foam column shown in Figure 3.3. The column (15cm wide × 15cm deep × 47 cm high)

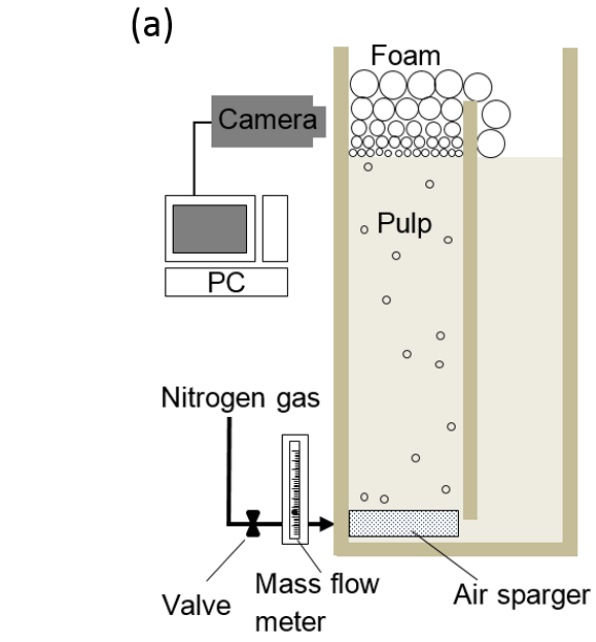

Figure 3.3 Equipment used to measure the bubble in a foam.

was built with flat plates to reduce optical distortion. The walls were made of glass to which bubbles rarely stick, enabling clear observation of a foam.

All experiments was conducted using a Millipore pure water with a resistivity of 18.2MΩ·cm at 25℃. Methyl isobutyl carbinol (MIBC, 98% purity, Aldrich) was chosen as a frother since it is the most widely used in industry [17].

Prior to each test, the column was placed in a base solution (distilled water, hydrogen peroxide and, ammonium hydroxide at a ratio of 4:1:1) for 10 min. to clean the surface of the glass wall. The column was then thoroughly rinsed with distilled water and allowed to be dried.

3.3.2 Experimental Procedure

The cell was first filled with aqueous solutions of methyl isobutyl carbinol (MIBC). Bubbles were generated by pumping the nitrogen gas through an air sparger located at the bottom of the foam column. The flow rate of gas was accurately controlled by adjusting the valve connected to a flow meter (Aalborg). The foam generated in this manner was allowed to freely overflow, mimicking flotation. The overflowed solution was recycled continually. The recirculation help keep the amount of MIBC in the solution, thus the value of surface tension may be kept. The foam height was monitored using a graduated scale embedded on the front wall of the column and was manually controlled by adjusting the level of pulp/froth interface. Behind the column, a 250 W light source was placed to illuminate the observation region with plastic board to obtain clear images. Once a steady state condition was reached, the images of the bubbles in a foam column were recorded by means of a high-speed camera (Fastec imaging).

3.3.3 Bubble Size Measurement

The average bubble diameters at the base of the froth ($d_{2,b}$) and the same at the top ($d_{2,b}$) were then calculated by analyzing the images offline using the BubbleSEdit, image-analysis software. The average bubble diameters were given by Sauter mean diameter (d_{32}),

$$d_{32} = \frac{\sum n_i d_i^{\,3}}{\sum n_i d_i^{\,2}} \tag{3.15}$$

where n_i is the number of bubbles with diameter d_i. In measuring the average bubble size in a foam or a froth, d_{32} is widely used since it can represent the average suitably [18] and also the flotation

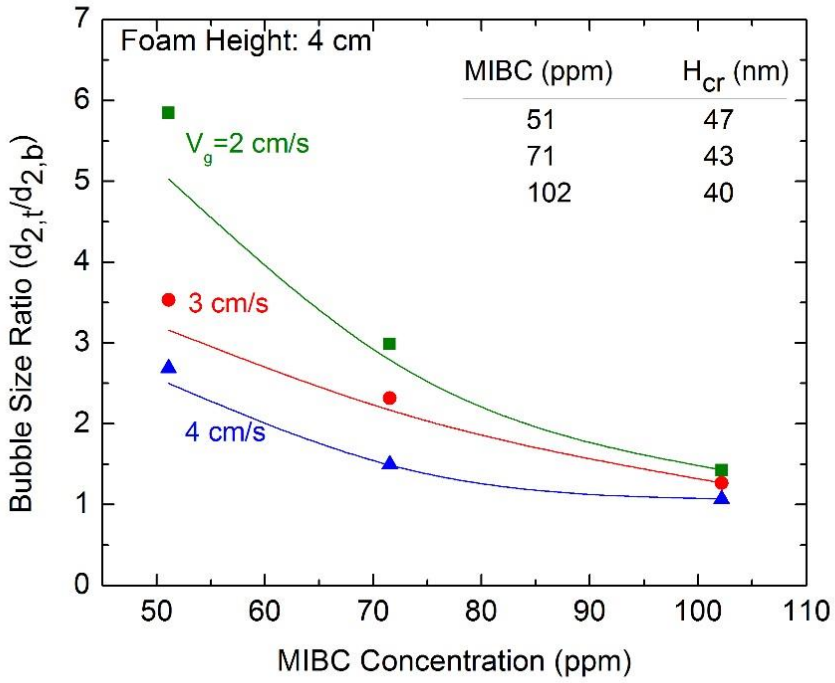

Figure 3.4 Bubble size ratio ($d_{2,t}/d_{2,b}$) between the top and bottom of a foam as a function MIBC concentration at different gas rates at a foam height of 4 cm. The lines drawn through the experimental data points represent the model predictions obtained using Eq. (3.7) on the basis of the critical film rupture thicknesses (H_{cr}) calculated from Eqs. (2.11) and (2.12).

rate is critically related with surface area of bubbles [19]. In the study, the values of bubble size ratio ($d_{2,t}/d_{2,b}$) were used as a measure of froth stability.

3.4 Results and Discussion

3.4.1 Effect of Frother Concentrations

Figure 3.4 shows the effect of frother (MIBC) concentration on bubble size ratio ($d_{2,t}/d_{2,b}$), a measure of bubble coarsening. While the foam height was kept constant at 4 cm, the experiments were conducted at 51, 71, and 102 ppm MIBC, which are much higher than industrial flotation dosage ranging between 1 and 10 ppm [17]. Such a high dosage was employed because at lower

concentrations, stable foam phase was not generated, mostly due to the absence of particles. It is generally known that particles are a solid-state surfactant that can enhance the form stability [20, 21]. The values of the *C* parameter were obtained by fitting the experimental data to the model and summarized in Table 3.1. The fit between the experimental data and simulation results (curves) were excellent. Both the model prediction and experimental data showed that the bubble coarsening decreased with increasing MIBC concentration, indicating that the frother stabilized the foam and retarded bubble coarsening. In effect, MIBC caused a decrease in $\sqrt{A_{cr}}$ or H_{cr}.

As suggested previously, the hydrophobic force present in foam films may be the major driving force for foam film rupture and that the hydrophobic force decreases with increasing frother concentration [9, 22]. Therefore, the decrease in hydrophobic force with increasing MIBC concentration can provide an explanation for the decrease in both $d_{2,t}/d_{2,b}$ and H_{cr}.

3.4.2 Effect of Foam Height

Figure 3.5 compares the values of $d_{2,t}/d_{2,b}$ at the foam heights of 2 and 4 cm. As expected, it was observed that the bubble size ratio increased with increasing foam height at a given superficial gas rate (V_g). The reason is simply that bubbles will have a longer time to coalesce in a taller froth height. The experiments were conducted at three different gas rates, i.e., V_g = 2, 3, and 4 cm/s. At a higher gas rates, the froth/pulp interface was lost due to flooding [23]. As shown, the bubble size ratio decreased most probably due to shorter residence times of bubbles [4].

Table 3.1 Values of fitting parameter *C* of Eqs. (3.7) and (3.8) used to predict bubble coarsening.

Superficial Gas Rate (cm/s)	MIBC (ppm)		
	51	71	102
2	16.60	10.01	3.33
3	8.44	5.75	1.65
4	5.30	2.29	0.36

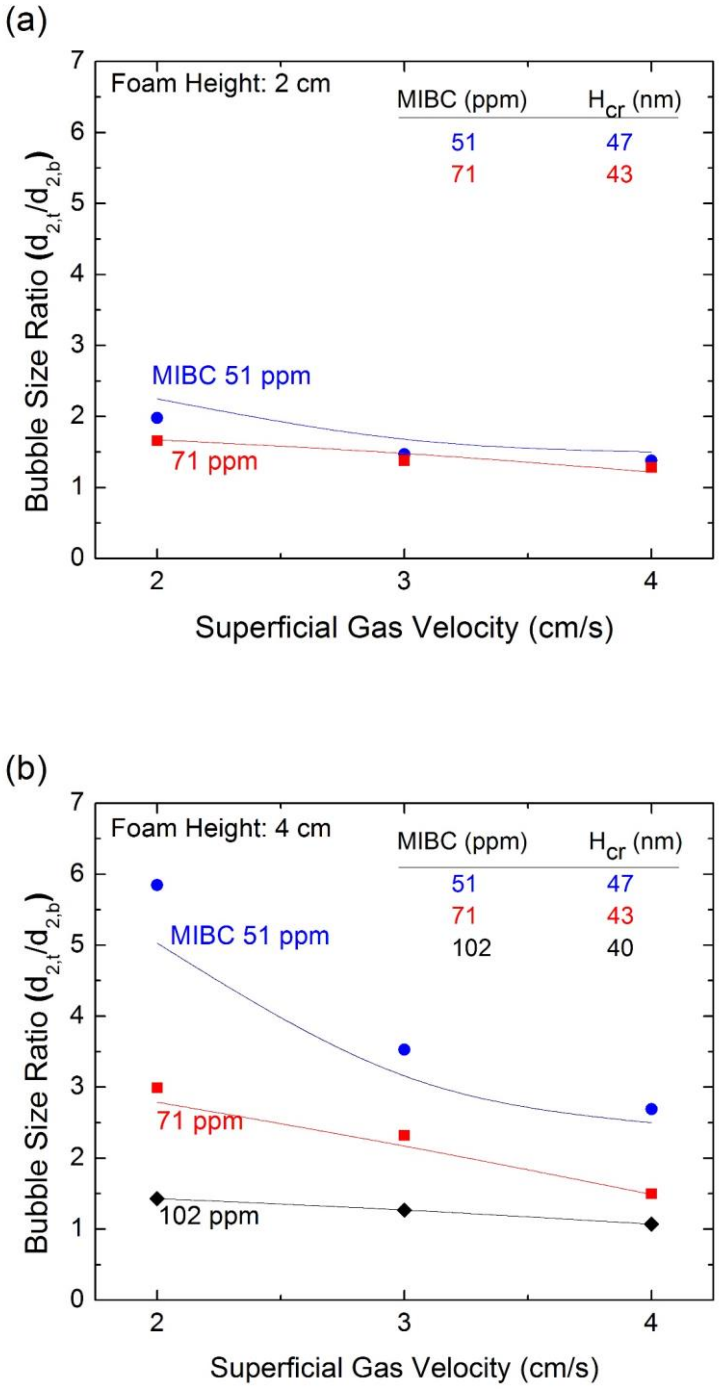

Figure 3.5 Bubble size ratio ($d_{2,t}/d_{2,b}$) between the top and bottom of a foam as a function of superficial gas rate at foam heights of 2 and 4 cm. The lines drawn through the experimental data points represent the model predictions obtained using Eq. (3.7) on the basis of the critical film rupture thicknesses (H_{cr}) calculated from Eqs. (2.10) and (2.11).

3.4.3 Effect of Gas Flow Rate

As shown in Figure 3.5, the experiments were conducted at three different gas flow rates, i.e., V_g = 2, 3, and 4 cm/s. A lower gas rate was not enough to create a foam phase. On the other hand, at a higher gas rates, the froth/pulp interface was lost due to flooding [23]. As shown, the bubble size ratio decreased with increasing gas rate. It may be due to the less chances for the bubble to be coalesce, most probably due to shorter residence times of bubbles in the foam phase [4].

3.5 Summary and Conclusions

A bubble-coarsening foam model has been developed. It is capable of predicting the bubble size at the top of a foam from the bubble size at the bottom. The input parameters of the bubble-coarsening model include froth height, frother dosage, gas flow rate, and the bubble size in the pulp phase. The model predictions show that bubble coarsening increases with decreasing frother dosage, which may be attributed to the increased hydrophobic force at lower frother dosages. It is also shown that bubble coarsening increases with increasing foam height and decreasing aeration rate, which can be attributed to longer residence times of the bubbles in the foam (or froth) phase. The model predictions are consistent with the experimental results. At this point, however, we are not considering the effects of particle size and particle hydrophobicity, which is known to affect froth stability [20, 21]. Thus, the model presented in this communication is for foam rather than for froth.

References

[1] Schwarz, S., et al., Water behaviour within froths during flotation. 2001.

[2] Barbian, N., K. Hadler, and J.J. Cilliers, The froth stability column: Measuring froth stability at an industrial scale. *Minerals Engineering*, 2006. **19**(6–8): p. 713-718.

[3] Barbian, N., et al., The froth stability column: linking froth stability and flotation performance. *Minerals Engineering*, 2005. **18**(3): p. 317-324.

[4] Tao, D., G.H. Luttrell, and R.H. Yoon, A parametric study of froth stability and its effect on column flotation of fine particles. *International Journal of Mineral Processing*, 2000. **59**(1): p. 25-43.

[5] Wang, L. and R.-H. Yoon, Effects of surface forces and film elasticity on foam stability. *International Journal of Mineral Processing*, 2008. **85**(4): p. 101-110.

[6] Tong, M., K. Cole, and S.J. Neethling, Drainage and stability of 2D foams: Foam behaviour in vertical Hele-Shaw cells. *Colloids and Surfaces A: Physicochemical and Engineering Aspects*, 2011. **382**(1–3): p. 42-49.

[7] Ivanov, I.B., et al., Theory of the critical thickness of rupture of thin liquid films. *Transactions of the Faraday Society*, 1970. **66**(0): p. 1262-1273.

[8] Vrij, A. and J.T.G. Overbeek, Rupture of thin liquid films due to spontaneous fluctuations in thickness. *Journal of the American Chemical Society*, 1968. **90**(12): p. 3074-3078.

[9] Wang, L.Q. and R.H. Yoon, Role of hydrophobic force in the thinning of foam films containing a nonionic surfactant. *Colloids and Surfaces a-Physicochemical and Engineering Aspects*, 2006. **282**: p. 84-91.

[10] Wang, L.G. and R.H. Yoon, Hydrophobic forces in thin aqueous films and their role in film thinning. *Colloids and Surfaces a-Physicochemical and Engineering Aspects*, 2005. **263**(1-3): p. 267-274.

[11] Do, H. Development of a Turbulent Flotation Model from First Principles. 2010, Virginia Polytechnic Institute and State University. PhD thesis.

[12] Verbist, G., D. Weaire, and A.M. Kraynik, The foam drainage equation. *Journal of Physics: Condensed Matter*, 1996. **8**(21): p. 3715-3731.

[13] Ganesan Narsimhan, E.R., Structure, drainage and coalescence of foams and concentrated emulsions in *Foams: Theory, Measurments, and Applications*, S.A.K. Robert K. Prud'homme, Editor. 1996, Marcel Dekker.

[14] Leonard, R.A. and R. Lemlich, A study of interstitial liquid flow in foam. Part I. Theoretical model and application to foam fractionation. *AIChE Journal*, 1965. **11**(1): p. 18-25.

[15] Schulze, H.-J., Physico-Chemical Elementary Processes in Flotation: Analysis from the Point of View of Colloid Science Including Process Engineering Considerations 1984: Elsevier Science Ltd

[16] Banisi, S. and J.A. Finch, Reconciliation of Bubble-Size Estimation Methods Using Drift Flux Analysis. *Minerals Engineering*, 1994. **7**(12): p. 1555-1559.

[17] Wang, L., Drainage and rupture of thin foam films in the presence of ionic and non-ionic surfactants. *International Journal of Mineral Processing*, 2012. **102–103**(0): p. 58-68.

[18] Feitosa, K. and D.J. Durian, Gas and liquid transport in steady-state aqueous foam. *The European Physical Journal E*, 2008. **26**(3): p. 309-316.

[19] Ata, S., N. Ahmed, and G.J. Jameson, A study of bubble coalescence in flotation froths. *International Journal of Mineral Processing*, 2003. **72**(1–4): p. 255-266.

[20] Binks, B.P., Particles as surfactants - similarities and differences. *Current Opinion in Colloid & Interface Science*, 2002. **7**(1-2): p. 21-41.

[21] Kaptay, G., On the equation of the maximum capillary pressure induced by solid particles to stabilize emulsions and foams and on the emulsion stability diagrams. *Colloids and Surfaces a-Physicochemical and Engineering Aspects*, 2006. **282**: p. 387-401.

[22] Wang, L.G., Drainage and rupture of thin foam films in the presence of ionic and non-ionic surfactants. *International Journal of Mineral Processing*, 2012. **102**: p. 58-68.

[23] Xu, M., J.A. Finch, and A. Uribe-Salas, Maximum gas and bubble surface rates in flotation columns. *International Journal of Mineral Processing*, 1991. **32**(3–4): p. 233-250.

Chapter 4. Modeling Froth Stability: Effect of Particle Hydrophobicity

ABSTRACT

As bubbles rise in a froth phase, a thin liquid film (TLF) confined between bubbles thins by the capillary pressure (p_c) and the disjoining pressure (Π). Once the intervening TLF ruptures, bubble-coarsening occurs. In the present work, we have studied the effect of particle hydrophobicity (or water contact angle θ) on the bubble-coarsening (or froth stability). The study was conducted by measuring the bubble size ratio between the top and bottom of a forth in the presence of monosized particles of varying hydrophobicity. The experimental results showed that the froth stability increases with θ up to $\theta = 70°$ and decreases with further increase in θ. We have also developed a model for predicting the bubble-coarsening in a froth by deriving a film drainage model quantifying the effect of θ on p_c. The model shows that with increasing θ up to $\theta = 70°$, p_c may decrease and thereby the film thinning is decelerated and the froth becomes more stable. At $\theta > 70°$, however, the froth becomes less stable due to increased p_c and, hence, increased drainage rate.

4.1. Introduction

Froth flotation is the most widely used method of upgrading pulverized ores in the minerals industry [1]. In this process, hydrophobic particles selectively attach to air bubbles in a pulp phase, forming particle-bubble aggregates, which subsequently rise upward due to reduced buoyancy and form a froth phase. In the froth phase, the bubbles coalesce with each other and become larger as they rise. As the bubbles become larger, the bubble surface area decreases, thereby restricting the number of hydrophobic particles that can be carried upward and subsequently flow into a launder. On the other hand, the bubble coarsening helps increase the grade of a froth product, as less hydrophobic particles selectively drop off the coarsening bubbles [2]. Thus, it is of critical importance to study and control bubble coarsening in the froth phase.

It is known that bubble coarsening occurs when a thin liquid film (TLF) formed between two bubbles in a froth phase breaks as a result of thinning. The kinetics of thinning of a TLF can be described by the Reynolds lubrication equation [3],

$$\frac{dH}{dt} = -\frac{2H^3 p}{3\mu R_f^2} \tag{4.1}$$

where H is the TLF thickness, t the drainage time, μ the dynamic viscosity, R_f the film radius, and p the driving force for TLF thinning. The equation is derived based on the Navier-Stokes equations under the assumptions of plane-parallel films and no-slip boundary conditions at the air/water interfaces.

In using Eq. (4.1), the driving force is given by the following relation,

$$p = p_c - \Pi \tag{4.2}$$

which shows that the driving force is the sum of capillary (or curvature) pressure (p_c) and disjoining pressure (Π).

During the initial film thinning, the drainage of a TLF is governed by the p_c whose magnitude is given by the Laplace equation [4],

$$p_c = \frac{2\gamma}{R} \tag{4.3}$$

where R is the bubble radius and γ is the surface tension of water.

When H reaches ~200 nm, surface forces or disjoining pressure (Π) between two air/water interfaces begin to act and control the thinning of the TLF. In Eq. (4.2), Π is determined according to the extended DLVO theory [5],

$$\Pi = \Pi_{el} + \Pi_{vw} + \Pi_{hp} = 64 C_{el} R_2 T \tanh^2\left(\frac{e\psi_s}{4kT}\right)\exp(-\kappa H) - \frac{A_{232}}{6\pi H^3} - \frac{K_{232}}{6\pi H^3} \tag{4.4}$$

where Π_{el} is the disjoining pressure due to electrostatic interaction, Π_{vw} is the disjoining pressure due to the van der Waals dispersion force, Π_{hp} is the disjoining pressure due to hydrophobic force, C_{el} is the electrolyte concentration, R_2 the gas constant, T the absolute temperature, e the electronic charge (e = 1.6 $\times 10^{-19}$ C), ψ_s the surface potential at the air/water interfaces, k the Boltzmann's constant, κ the reciprocal Debye length, A_{232} the Hamaker constant, and K_{232} the hydrophobic constant.

When the H finally reaches a critical thickness (H_{cr}), the TLF ruptures and thereby bubble coalesces. The value of H_{cr} was theoretically predicted by Vrij and his co-workers based on capillary wave theory [6-8],

$$144\gamma\left\{3H_m^{-4}\left(\left.\frac{\partial\Pi}{\partial H}\right|_{H=H_m}\right)^{-2} - 2H_m^{-3}\left(\left.\frac{\partial\Pi}{\partial H}\right|_{H=H_m}\right)^{-3}\left.\frac{\partial^2\Pi}{\partial H^2}\right|_{H=H_m}\right\} - \frac{3H_m^{-3}R_f^{\,2}}{2(p_c - \Pi)} = 0 \tag{4.5}$$

where $H_{cr} = 0.845 H_m$. The model assumes that the air/water interfaces of a foam film fluctuate due to thermal or mechanical motion, creating corrugation. The amplitude of the wave motion grows if the disjoining pressure of the film (Π) is negative, and the film ruptures when the two interfaces touch each other. In their original model, only the van der Waal disjoining pressure (Π_{vw}) and the electrostatic disjoining pressure (Π_{el}) were considered, which makes it difficult to predict H_{cr} at low frother concentration, at which air bubbles become strongly hydrophobic [9]. Park *et al.* [10] predicted the values of H_{cr} of foam films containing methyl-isobutyl carbinol (MIBC) using

the extended DLVO theory, which considers the contributions from the hydrophobic force (Π_{hp}) [11]. The hydrophobic force constant (K_{232}) determined by Wang [12] were used for this approach. The model predictions are in agreement with the H_{cr} values measured by Wang [12], and the results show that foam film stability increases with increasing frother dosage due to dampening of the hydrophobic force in the presence of a frother.

Froth is a 3-phase foam, and its behavior is different from foam due to the presence of particles. As is well known, froth becomes more stable in the presence of particles [13-16]. Ata *et al*. [17] experimentally observed that the froth stability depends critically on particle hydrophobicity (or water contact angle θ). They measured the bubble size distribution within froth phase along the height in the presence of glass particles of different contact angles (θ = 50°, 66°, and 82°). The bubble size increased with froth height owing to increased bubble coalescence. They found also that the bubble growth rate was sensitive to θ. The bubble growth rate was lowest in the presence of the intermediate hydrophobic particles (66°) and highest in the presence of the weekly hydrophobic particles (50°). Experimentally, their results indicated that there is an optimum particle hydrophobicity (~66°) for the maximum froth stability.

Binks [18] derived a model that can calculate the energy required to detach a particle from an air/water interface,

$$\Delta G_d = \pi r_1^2 \gamma (1-\cos\theta)^2 \tag{4.6}$$

where r_1 is the particle radius. For the TLF of a froth to rupture and disappear, the particle located at the interface should be removed. Eq. (4.6) suggests that less hydrophobic particles can be readily washed off the TLF, whereas more hydrophobic particles will be more difficult to be washed off and thereby help stabilize the froth. If this was the case, the maximum froth stability should be achieved at θ = 90°. However, the Binks' model alone cannot successfully explain the Ata *et al*.'s observations [17]. The discrepancy may be originated from the limitation that the Binks' model is derived on the basis of only thermodynamic aspect, though the kinetics of the TLF is a more dynamic process including the hydrodynamic effect.

Denkov *et al*. [19] proposed a stabilization mechanism of emulsions by absorbed particles. The mechanism was based on the recognition that the particles create changes in the curvature of

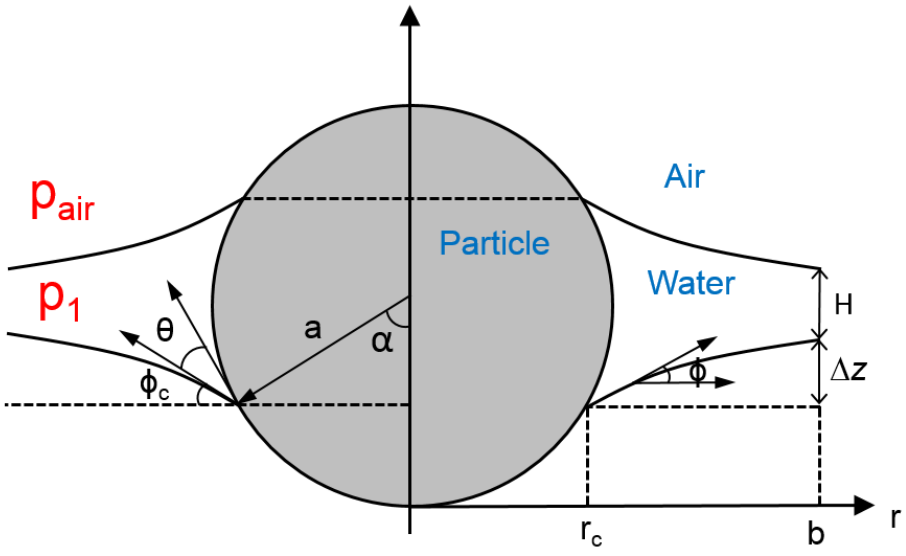

Figure 4.1 Sketch of an absorbed particle in the thin liquid film between two air bubbles. The curvature of the air/water interface around the particle creates the difference between the pressure inside of the bubble (p_{air}) and the same in the film (p_1).

the air/water interface and hence the local capillary pressure ($p_{c,local}$), which in turn affect thin film rupture. Due to the similarity between a foam and an emulsion, their model may possibly be used to explain the froth stability. As shown in Figure 4.1, the $p_{c,local}$ ($\equiv p_{air} - p_{water}$) arises from the local curvature changes around the particle and it can be given by the Young-Laplace equation,

$$p_{c,local} = \frac{\gamma}{r}\frac{d}{dr}(r\sin\phi) \tag{4.7}$$

where r is the radial position, and ϕ is the running slope angle. In their paper, the $p_{c,local}$ was calculated numerically by combining the following geometrical relationships,

$$p_{c,local} = 2\gamma\frac{\sin\phi_c r_c}{b^2 - r_c^2} \tag{4.8}$$

$$\Delta z = \int_{r_c}^{b} \frac{b^2 - r^2}{\sqrt{\left(\frac{2\gamma}{p_{c,local}}\right)^2 r^2 - (b^2 - r^2)^2}}dr \tag{4.9}$$

$$H = 2(a\cos\alpha - \Delta z) \tag{4.10}$$

$$r_c = a\sin(\phi_c + \theta) \tag{4.11}$$

where ϕ_c is the slope of the curvature at contact line, r_c the radial position of contact line, α the angle between the vertical line and contact line, Δz the depth between the contact line and the interface, θ the contact angle, b the radius of the cell, and H the TLF thickness at the boundary of the cell.

Figure 4.2 shows the $p_{c,local}$ *vs*. H plots predicted from Denkov's model. It indicates that $p_{c,local}$ increases slightly with decreasing H and reaches a maximum at $H = 0$. The model assumed that the TLF ruptures at $H = 0$ and the maximum values of $p_{c,local}$ were used as a criteria for evaluating the emulsion stability. The higher the maximum values of $p_{c,local}$, the more stable emulsions. Thus, the calculation results shown in Figure 4.2 suggest that the froth stability

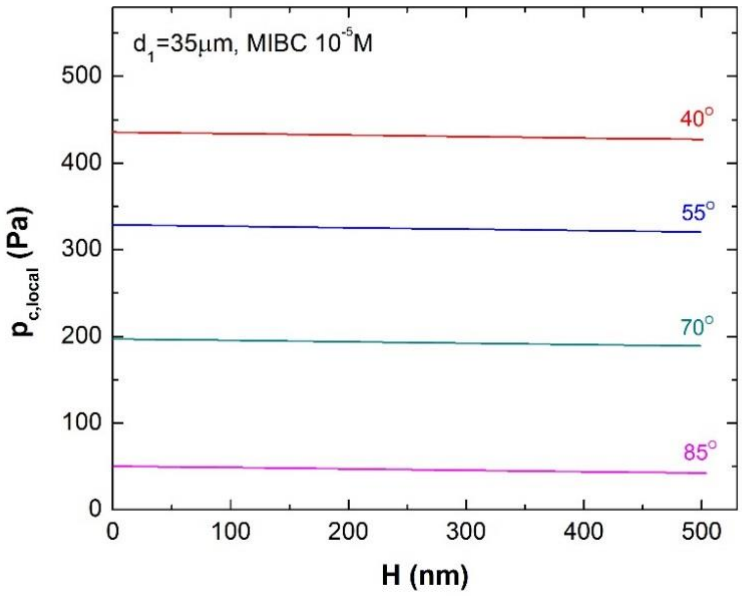

Figure 4.2 Local capillary pressure ($p_{c,local}$) arising from a particle with contact angle (θ) of 40°, 55°, 70° and 85°, respectively, as a function of the film thickness (H). The plots are obtained using Eqs. (4.8) ~ (4.11) with a = 70 μm, b = 210 μm, γ = 0.0724 N/m.

decreases with increasing θ. However, this trend is not compatible with previous experimental observations mentioned above [17]. The discrepancy may be due to several limitations of Denkov's model. First, the model did not consider the whole area of a film. Only the force balance around particles was considered. Second, surface forces were neglected although recently it has shown that they are important in determining the stability of foam films [5, 20]. Finally, the model assumes that films rupture when film thickness is reduced to zero. Many investigators showed, however, that films rupture at critical rupture thicknesses, which are non-zero and vary significantly with surfactant type and dosage [5, 7, 8].

More recently, Morris *et al*. [21-23] conducted computational simulations to estimate the TLF stability by calculating the maximum values of $p_{c,local}$ in the TLF containing multiple spherical particles. Their approach was a step forward from Denkov *et al*.'s work in that the whole area of a film was modelled. However, their simulation result showing that the maximum values of $p_{c,local}$ and the TLF stability decrease with increasing θ still do not agree well with the Ata *et al*.'s observations [17]. The discrepancy may be attributed to the still unresolved limitations that surface forces and H_{cr} were not considered and that the possible variation of the number of particles in a TLF with changes in θ.

In the present work, we have conducted laboratory-scale flotation testes to measure froth stability in the presence of silica particles of varying surface hydrophobicity (θ = 40°, 55°, 70°, 85°). In each experiment, using a high-speed camera and image-analysis software, we have measured the bubble size ratio ($d_{2,t}/d_{2,b}$), the ratio of average bubble diameter at the top of the froth ($d_{2,t}$) and to the same at the base of the froth ($d_{2,b}$), as a measure of froth stability. We have also developed a theoretical model that can explain the effects of θ on bubble coarsening (or froth stability). The model was derived by modelling the whole area of a TLF by considering both the capillary force and the surface forces. Furthermore, the model developed here enables us to predict $d_{2,t}/d_{2,b}$ as a function of frother dosage, froth height, gas rate, specific power, particle size, particle hydrophobicity (collector dosage), particle concentration, *etc*.

4.2. Experiment

4.2.1 Materials and Hydrophobization of Silica Surfaces

In the present study, silica spheres (Potters industries) of 35 μm diameter (d_1) were used for flotation test. The spheres along with a referential silica plate were firstly cleaned in Piranha solution (H_2O_2/H_2SO_4 3: 7 by volume) for 1 h at 120 ℃, rinsed with ultrapure water for 10 min, and then dried at 160 ℃ in an oven for 24 h. The silica surface is naturally hydrophilic; therefore, its surface was rendered hydrophobic using octadecyltrichlorosilane (OTS, 95% purity, Alfa Aesar). The spheres were immersed in a 10^{-4} M OTS-in-toluene (99.9% purity, Spectrum Chemical) solution along with a referential silica plate, so that both could have identical hydrophobicity. The hydrophobized surfaces were then rinsed with chloroform (99.9% purity, Fisher Chemical), acetone (99.9 % purity, Aldrich), and ultrapure water sequentially. The hydrophobicity of the particle surfaces, as measured by water contact angles (θ), was controlled by varying the

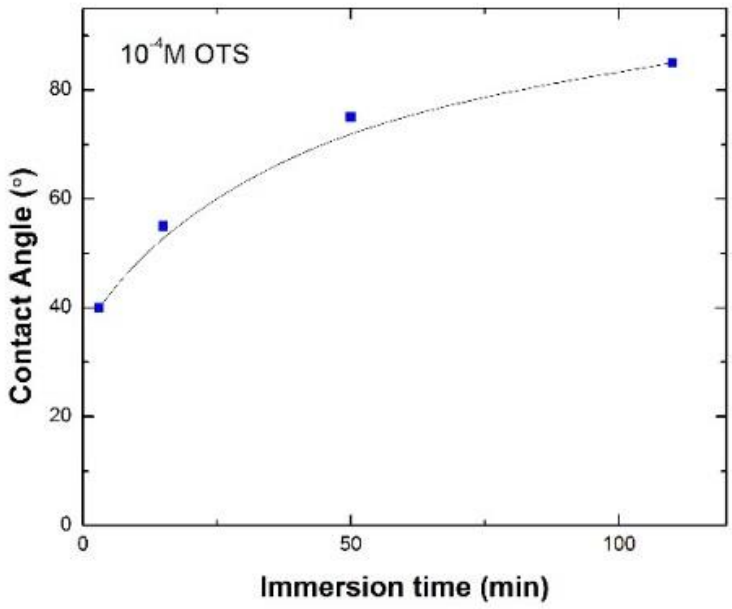

Figure 4.3 Effects of immersion time on the contact angles of silica in 10^{-4} M OTS-in-toluene solutions.

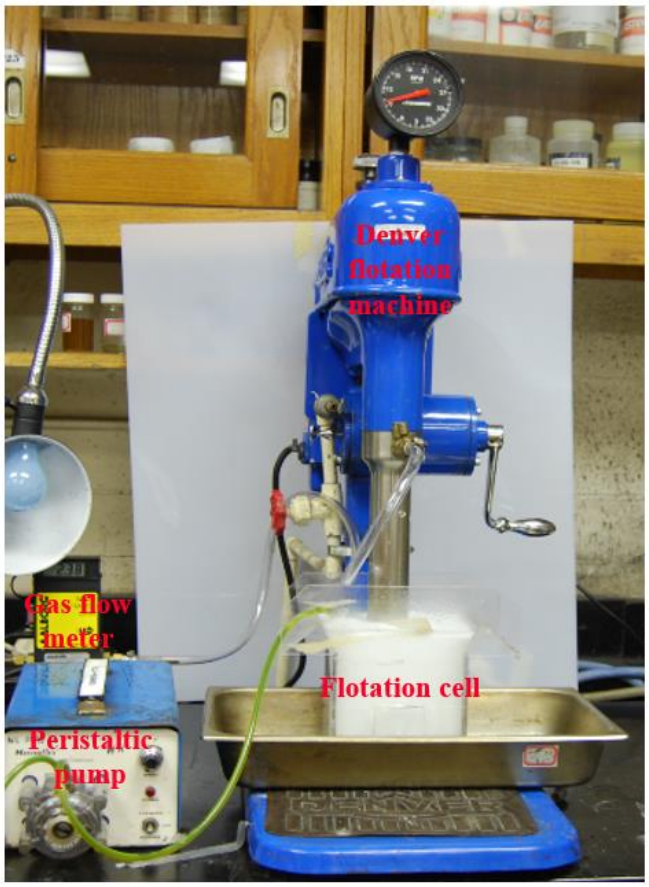

Figure 4.4 Equipment used to measure the bubble sizes in the froth.

immersion time. The contact angle measurements were conducted on the silica plates using the sessile drop technique. The measurements were five times on each sample and averaged. As shown in Figure 4.3, the contact angles increased with increasing immersion times. Accordingly, particles with four different particle hydrophobicities (θ = 40°, 55°, 70°, and 85°, respectively) were prepared to investigate the effect of θ on froth stability.

4.2.2 Experimental Procedure

The stability measurements were conducted using a Denver laboratory flotation cell shown in Figure 4.4. The 1.5 L of cell was filled with water of 10^{-5} M methyl-isobutyl carbinol (MIBC, 98% purity, Aldrich). The hydrophobized silica particles were added to the cell so that the solids concentration became 5% w/w. Air bubbles were generated by blowing air into the pulp phase at

a fixed gas rate of 6 L/min to obtain a superficial gas velocity of 1cm/s. The slurry was kept in suspension by agitating it at an impeller speed of 900 rpm.

The froth was allowed to freely overflow, let to destabilize, and then recycled back to the cell by means of a peristaltic pump. The froth height was monitored using a graduated scale embedded on the front wall of the cell. Once a steady state condition was reached, the images of the bubbles in the froth were recorded by means of a high-speed camera. The average bubble diameters at the base of the froth ($d_{2,b}$) and at the top ($d_{2,b}$) were then obtained by analyzing the images offline using the BubbleSEdit, image-analysis software. The average bubble diameters were given by calculating the Sauter mean diameter (d_{32}),

$$d_{32} = \frac{\sum n_i d_i^3}{\sum n_i d_i^2} \tag{4.12}$$

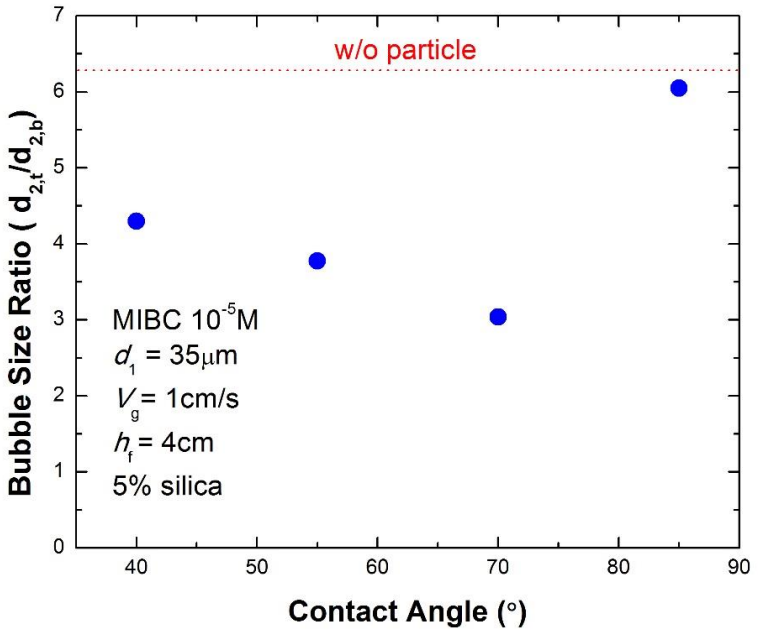

Figure 4.5 The bubble size ratio ($d_{2,t}/d_{2,b}$) measured in the presence of particles with contact angle(θ) of 40°, 55°, 70°, and 85°, respectively. The dotted line represents $d_{2,t}/d_{2,b}$ in the absence of particles.

where n_i is the number of bubbles with diameter d_i. In measuring the average bubble size in a foam or a froth, d_{32} is most widely used in flotation literature. The number-mean diameter gives excessive weights on fine bubbles, while the volume-mean diameters does son on coarse bubbles. On the other hand, flotation rate is shown is critically related to surface area of bubbles [17]. Therefore, the Sauter mean diameter may be considered most suitable for flotation studies [24].

4.3 Experimental Results

Laboratory flotation tests were conducted both in the absence and presence of monosized (35μm) silica particles. To investigate the effect of particle hydrophobicity (θ) on the bubble size ratios ($d_{2,t}/d_{2,b}$), which is considered as a measure of froth stability in the present work, particles of different contact angles (θ = 40°, 55°, 70°, and 85°, respectively) were tested. In all tests, the frother dosage (10^{-5} M MIBC), gas flow rate (V_g = 1 cm/s), froth height (h_f = 4 cm), agitation speed (900 rpm), and the particle concentrations (5% w/w) were carefully kept constant.

Figure 4.5 shows the experimentally measured values of $d_{2,t}/d_{2,b}$. As shown, the $d_{2,t}/d_{2,b}$ ratios becomes smaller in the presence of particles. As shown, air bubbles becomes stable in the presence of particles of $\theta < 90°$. Note also that $d_{2,t}/d_{2,b}$ decreased with increasing θ, reaching a minimum at $\theta = 70°$, and the increased with further increase in θ. The observed trends are consistent with Ata *et al.*'s results [17]. It was shown that bubbles in the froth phase immediately collapsed when very hydrophobic particles ($\theta > 90°$) were added to a forth phase.

4.4 Model Development

In section 4.4, we present a new methodology that can predict the bubble size ratios ($d_{2,t}/d_{2,b}$) in a froth phase. In Subsection 4.4.1, we first calculate the driving force (p) for the thinning of a froth film containing particles with different contact angles (θ). To calculate p, we need to know $N_{1,film}$ (the number of particles in a single film). Subsection 4.4.2 introduces a new model that can predict $N_{1,film}$ as a function of θ. In Subsection 4.4.3, substituting the p values into the Reynolds equation, the thinning rates of the froth films are determined as a function of θ. After that, the critical rupture thickness (H_{cr}) model developed in Chapter 2 is used to predict the critical rupture time (t_{cr}) of the froth film as a function of θ. In Subsection 4.4.4, a model that can predict $d_{2,t}/d_{2,b}$ from t_{cr} is developed.

4.4.1 Driving Force for a Froth Film Thinning

a. Foam Film

Prior to modelling a froth film, consider a foam film stabilized in the presence of 10^{-5} M MIBC. As shown in Eq. (4.2), the driving force (p) for film thinning is the sum of the capillary pressure (p_c) and the disjoining pressure (Π). These parameters are functions of film thickness (H) as shown in Eqs. (4.2), (4.3), and (4.4). The model parameters were calculated using the values of R = 0.44 mm and T = 298 K in accordance to the actual bubble sizes measured at the base of a foam and the temperature at which the experiments were conducted. The values of γ = 0.0724 N/m and ψ_s = -30 mV were also used as reported by Comley *et al*. [25] and Srinivas *et al*. [26]. Also the values of $K_{232} = 2.3\times10^{-19}$ J and $A_{232}= 4\times10^{-21}$ J were used as reported by Wang [12]. Only the value of κ^{-1}= 30 nm was assumed. The calculation results are shown in Figure 4.6. As shown, p_c is constant during film thinning due to the assumption of flat lamella film. On the other hand, Π becomes more negative as the film becomes thinner, which can be attributed to the presence of

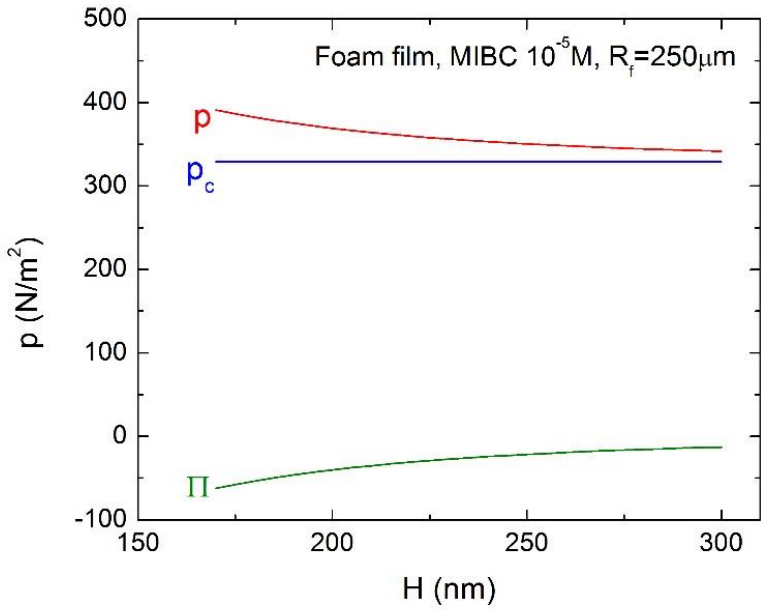

Figure 4.6 The changes in driving pressure (p), capillary pressure (p_c), and disjoining pressure (Π) as a function of a MIBC foam film thickness (H). The plots are drawn from Eqs. (4.2) ~ (4.4) with $K_{232} = 2.3\times10^{-19}$ J, $A_{232}= 4\times10^{-21}$ J, R = 0.44 mm, γ = 0.0724 N/m, T = 298 K, e = 1.6 $\times10^{-19}$ C, ψ_s = -30 mV, and κ^{-1}= 30 nm.

attractive force in the film that varies as H^{-3}. Note here that as the film drains, p increases mainly due to the increase in the negative disjoining pressure ($\Pi < 0$).

The critical rupture thickness (H_{cr}) of the foam film was determined using Eq. (4.5). In using Eq. (4.5), we needed to know the film size (R_f). Assuming that a bubble has a dodecahedron structure, consisting of 12 films, the surface area of a single film (πR_f^2) should be the same as $4\pi R^2/12$. Thus, R_f can be determined from R as follows,

$$R_f = R/\sqrt{3} \tag{4.13}$$

in which R = 0.44 mm as measured at the base of the froth (or foam) in this study. Eq. (4.13) gives the value of R_f to be 250 μm. In the present study, R_f was assumed to be independent of H in accordance to the previous experimental observations [20]. Figure 4.7 shows the model prediction of the values of H_{cr} using Eq. (4.5). As shown, H_{cr} decreases with MIBC concentration, which can be attributed to the effect of dampening of hydrophobic force in the presence of a surfactant [27]. At 10^{-5} M MIBC, where tests were conducted, H_{cr} was found to be 171 nm.

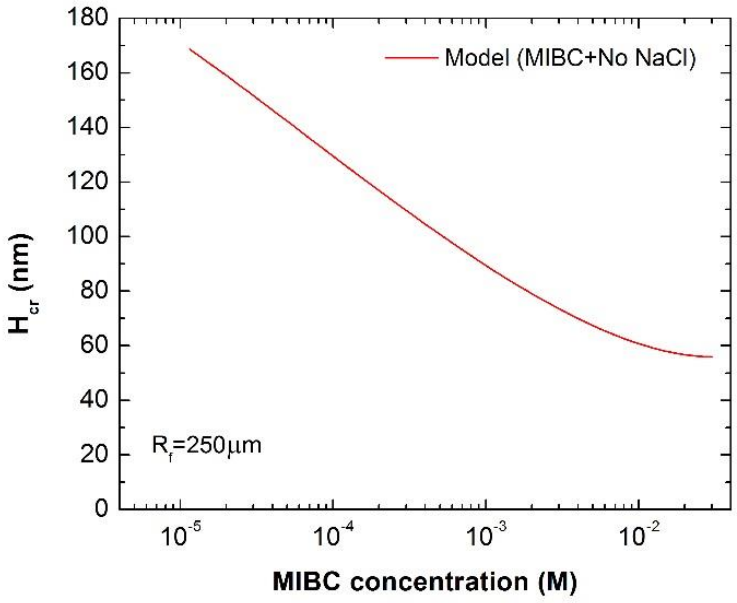

Figure 4.7 Plots of the critical film rupture thicknesses (H_{cr}) of a foam film predicted using the H_{cr} model developed in Chapter 2 vs. MIBC concentration.

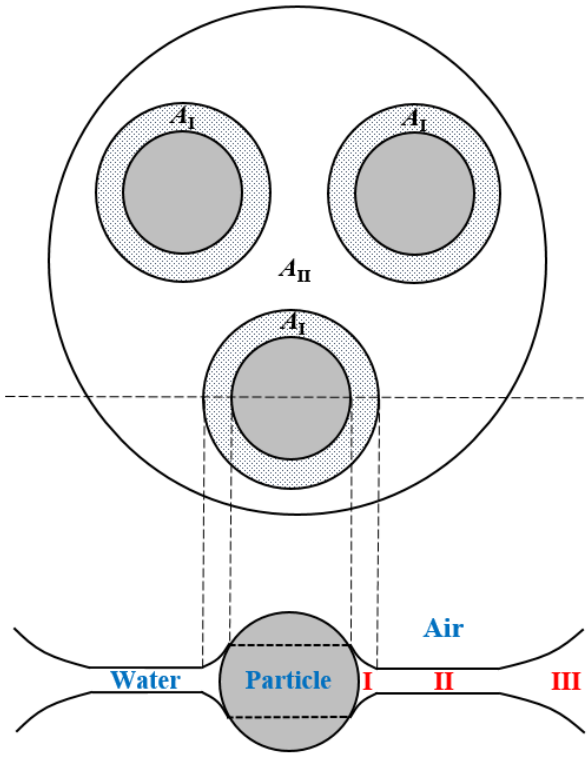

Figure 4.8 Sketch of a layer of particles located in the thin liquid film between two air bubbles. Near the particle a curvature change occurs (Section I), while the free film is formed away from the particle (Section II). Section III denotes a Plateau boarder area.

b. Froth Film

The presence of particles in froth films should cause the local curvatures at the air/water interface to change, which should in turn cause the capillary pressure (p_c) to change from that of free films. The presence of particles may also change the disjoining pressure (Π) and hence the hydrodynamic pressure (p). Figure 4.8 represents a lamella film, in which three spherical particles are embedded. The film around each particle, may be subdivided into Sections I, II and III, representing the area in the vicinity of a particle, the area away from the particle, and the outside the film (Plateau border), respectively.

The pressure (or force) balance in each section may be give as follows,

$$p_{air} - p_I = p_{c,local} \tag{4.14}$$

$$p_{air} - p_{II} = 0 \tag{4.15}$$

$$p_{air} - p_{III} = \frac{2\gamma}{R} \tag{4.16}$$

where p_{air} is the pressure in the air bubble, p_I and p_{II} are the those in Sections I and II, respectively, $p_{c,local}$ is the local capillary pressure that may be calculated using Eqs. (4.7)-(4.11), and R is the bubble radius. Assuming that $p_{III} \approx 0$, one obtains the capillary pressures in Sections I and II as follows,

$$p_I = \frac{2\gamma}{R} - p_{c,local} \tag{4.17}$$

$$p_{II} = \frac{2\gamma}{R} \tag{4.18}$$

The capillary pressure (p_c) of the film as a whole may then be calculated as follows,

$$p_c = \frac{\text{Overall capillary force}}{\text{Film area}} = \frac{p_I A_I N_{1,film} + p_{II} A_{II}}{A_I N_{1,film} + A_{II}} \tag{4.19}$$

where A_I and A_{II} is the film areas occupied by Section I and II, respectively, and $N_{1,film}$ is the number of particles present in the single film. The values of $N_{1,film}$ may vary with operating conditions. A model for predicting $N_{1,film}$ is presented in Section 4.4.2.

Likewise, one can calculate the overall disjoining pressure (Π) using the following relation,

$$\Pi = \frac{\text{Overall surface force}}{\text{Film area}} = \frac{\Pi_I A_I N_{1,film} + \Pi_{II} A_{II}}{A_{II}} \tag{4.20}$$

in which Π_I and Π_{II} are the disjoining pressures in Sections I and II, respectively. Section II is a free film; therefore, its disjoining pressure can be given as follow,

$$\Pi_{II} = \Pi_{el} + \Pi_{vw} + \Pi_{hp} = 64 C_{el} RT \tanh^2\left(\frac{e\psi_s}{4kT}\right)\exp(-\kappa H) - \frac{A_{232}}{6\pi H^3} - \frac{K_{232}}{6\pi H^3} \tag{4.21}$$

On the other hand, the disjoining pressure in Section I (Π_I) may be obtained by integrating the local disjoining pressure along the radial direction,

$$\Pi_I = \frac{\int_{r_c}^{b} \Pi(r)(2\pi r)dr}{A_I} \tag{4.22}$$

In the vicinity of a particle, $\Pi(r)$ is small because the film thickness (H) increases sharply with decreasing r, approaching the length scale of the particle. At such large film thicknesses, disjoining pressures should be close to zero. Thus, $\Pi_I \approx 0$. Substituting this into Eq. (4.20), $\Pi \approx \Pi_{II}$, which means that particles should not seriously affect Π.

4.4.2 Number of Particles in a Froth Film

In using Eqs. (4.19) and (4.20), we need to know the value of $N_{1,film}$ (the number of particles in a froth film). This section shows a new model that can predict $N_{1,film}$ theoretically. $N_{1,film}$ may change continually along the froth height due to the continuing detachment of particles resulting

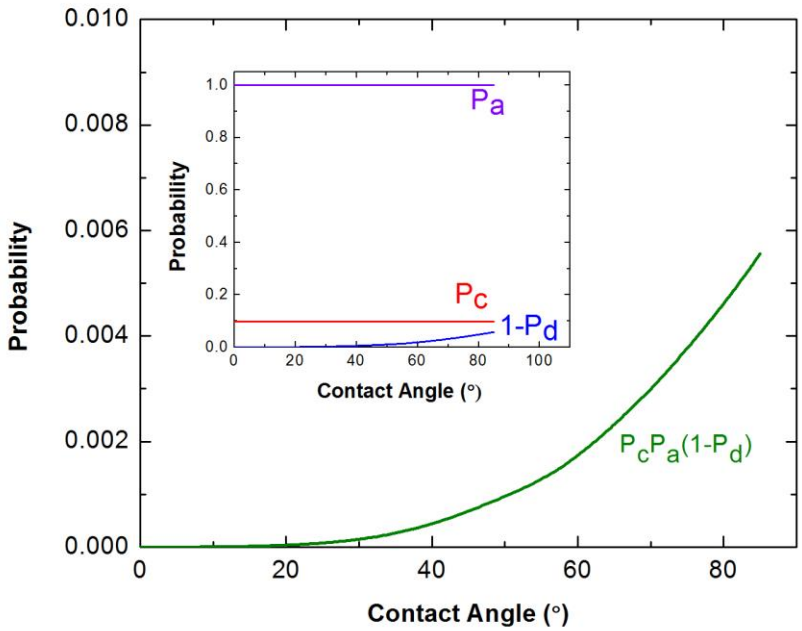

Figure 4.9 Probability of particles surviving in a pulp phase $P_c\,P_a\,(1\text{-}P_c)$ vs. particle contact angles (θ). The inset shows the probability of collision (P_c), the probability of attachment (P_a), and the probability of detachment (P_d), respectively.

from bubble coarsening. This model is aimed to model the base of a froth. Thus, $N_{1,film}$ at the base of a froth is need to be predicted. The model for predicting $N_{1,film}$ at the base of a froth was derived based on the assumption that the value of $N_{1,film}$ may be proportional to the probability of particles reaching a froth phase.

The probability of particles reaching a froth phase (P) is given by,

$$P = P_c P_a (1 - P_d) \tag{4.23}$$

where P_c is the probability of collision, P_a the probability of attachment, and P_d the probability of detachment. The probability functions are given as follows, respectively,

$$P_c = \tanh^2\left(\sqrt{\frac{3}{2}\left[1+\frac{3}{16}\left(\frac{\mathrm{Re}}{1+0.249\mathrm{Re}^{0.56}}\right)\right]}\left(\frac{d_1}{d_2}\right)\right) \tag{4.24}$$

$$P_a = \exp\left(-\frac{E_1}{E_k}\right) \tag{4.25}$$

Table 4.1 Input parameters for the simulation shown in Figure 4.9.

Frother (MIBC) concentration (M)	10^{-5}
Solids concentration (% w/w)	5
Specific power (kW/m^3)	22.8
Superficial gas rate (cm/s)	1.0
Froth height (cm)	4
Particle size (μm)	35
Particle Zeta potential (mV)	-0.08
Bubble Zeta potential (mV)	-0.03

$$P_d = \exp\left(-\frac{W_a + E_1}{E_k'}\right) \tag{4.26}$$

where Re is the Reynolds number, E_1 is the energy barrier, E_k is the kinetic energy available during attachment process, W_a is the work of adhesion, and E'_k is the kinetic energy of detachment. The plots of probability functions (P_c, P_a, and P_d) are shown in Figure 4.9 and input parameters for this simulation is summarized in Table 4.1. In the simulation, the bubble zeta potential was obtained from Comley *et al.*'s study [25], the particle zeta potential was assumed, and the other parameters were measured from experiments. Note in Figure 4.9 that the value of 1-P_d increases with increasing θ, which is mainly due to the increase in adhesion force (W_a) between a bubble and a particle. It is also noteworthy that P_a is close to 1 even for hydrophilic particles. This is mainly due to the relatively higher power dissipation rate (22.8 kW/m^3) of laboratory flotation cells as compared to industrial flotation machines, resulting in higher kinetic energy.

In the present study, $N_{1,film}$ may be related to P (=$P_c P_a$ (1 - P_d)) as follows,

$$N_{1,film} = N_{1,seg} P_c P_a (1 - P_d) \tag{4.27}$$

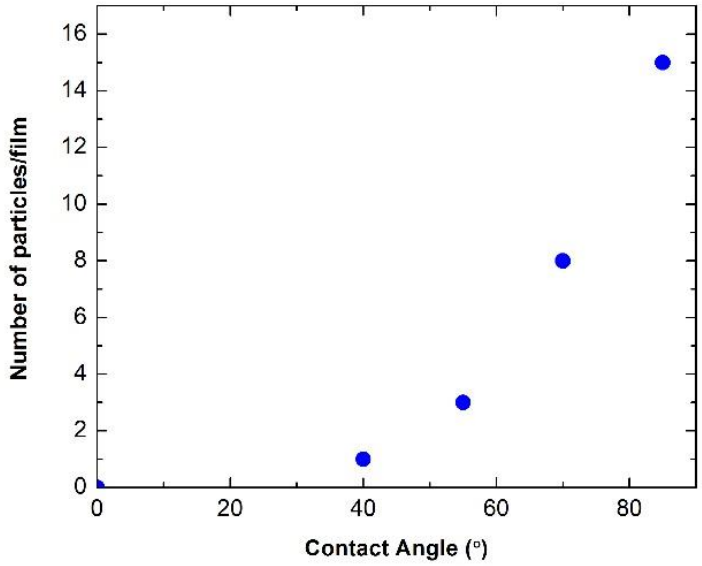

Figure 4.10 The number of particles residing in a froth film ($N_{1,film}$) predicted as a function of particle contact angles (θ).

where $N_{1,seg}$ is the number of the particles having a chance to collide with a bubble surface segment in pulp phase ending up a single lamellar film in the froth phase. The value of $N_{1,seg}$ may be proportional to the number of particles suspending in the pulp. In each experiment, we added same amount of particles, so the constant $N_{1,seg}$ value ($N_{1,seg}$ = 2667) was assumed. After that, as shown in Figure 4.10, we finally predicted the values of $N_{1,film}$ as a function of θ. It was found that $N_{1,film}$ critically depends on θ. Note here that more particles can locate in a film at higher θ, most probably due to lower P_d values.

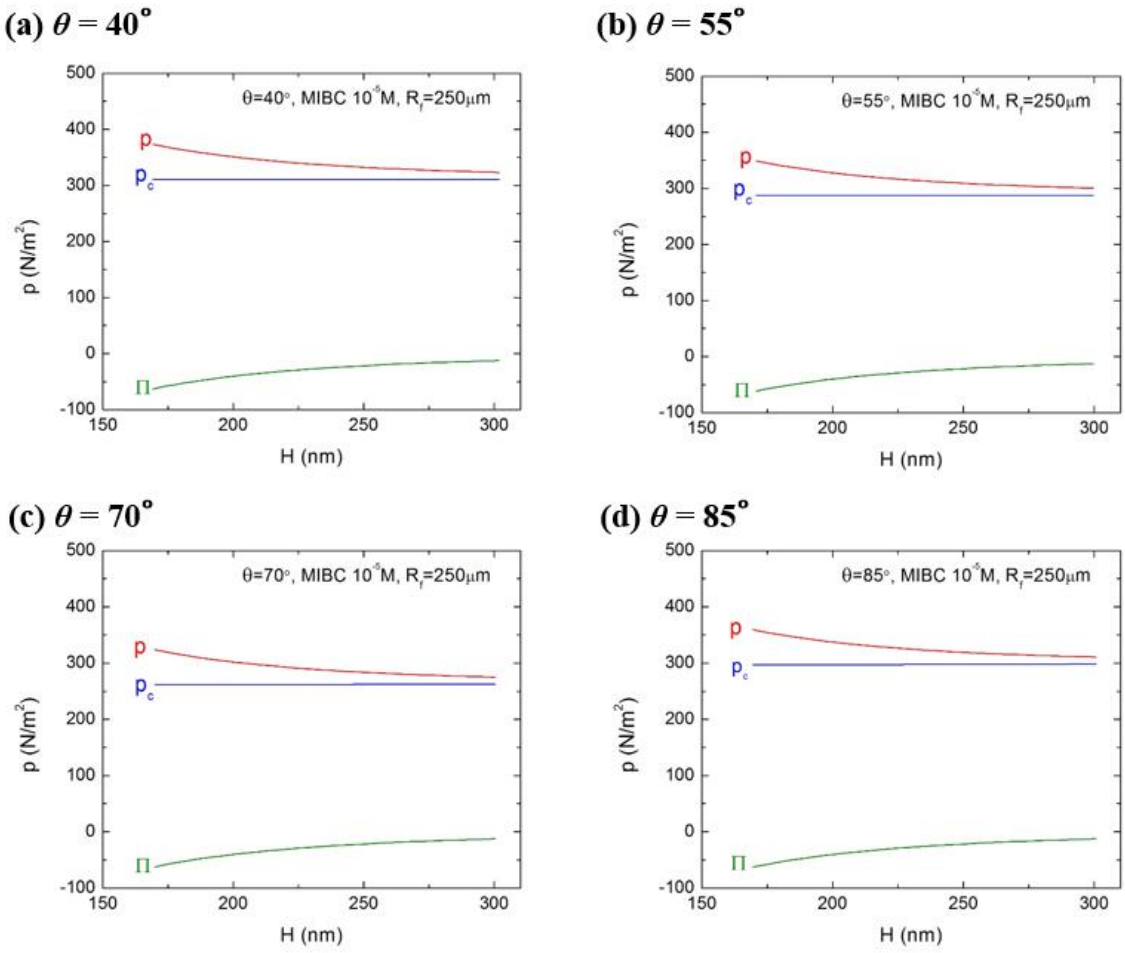

Figure 4.11 The changes in driving pressure (p), capillary pressure (p_c), and disjoining pressure (Π) as a function of the froth film thickness (H) containing particles with contact angle (θ) of (a) 40°, (b) 55°, (c) 70°, and (d) 85°. The values of K_{232} = 2.3×10^{-19} J, A_{232}= 4×10^{-21} J, R = 0.44 mm, γ = 0.0724 N/m, T = 298 K, e = 1.6 ×10^{-19} C, ψ_s = -30 mV, and κ^{-1}= 30 nm were used.

4.4.3 The Critical Rupture Time (t_{cr}) of a Froth Film

Substituting the $N_{particle}$ values predicted in Section 4.4.2 into Eq. (4.19), one can determine the values of p_c. On the other hand, Π can be determined using Eq. (4.21) using the values of K_{232} = 2.3×10^{-19} J, A_{232} = 4×10^{-21} J, R_f = 250 μm, T = 298 K, γ = 0.0724 N/m, ψ_s = -30 mV, and κ^{-1}= 30 nm were used. Substituting the values of p_c and Π obtained in this manner into Eq. (4.2), one can obtain p as a function of particle hydrophobicity (θ). Figure 4.11 shows the calculated values of p_c, Π, and p. It is noteworthy that as compared to the foam film (shown in Figure 4.6), the absorbed particles decreased p_c and p during the process of film drainage, which can be attributed to the local capillary pressure ($p_{c,local}$) created by the particles. However, Π was not changed, as mentioned above. More importantly, Figure 4.11 shows that the values of p_c and p change with θ. It was found also that with increasing θ up to θ = 70°, p_c decreased and, therefore, p decreases. On the other hand, at θ > 70° p_c and p increased with further increase in θ.

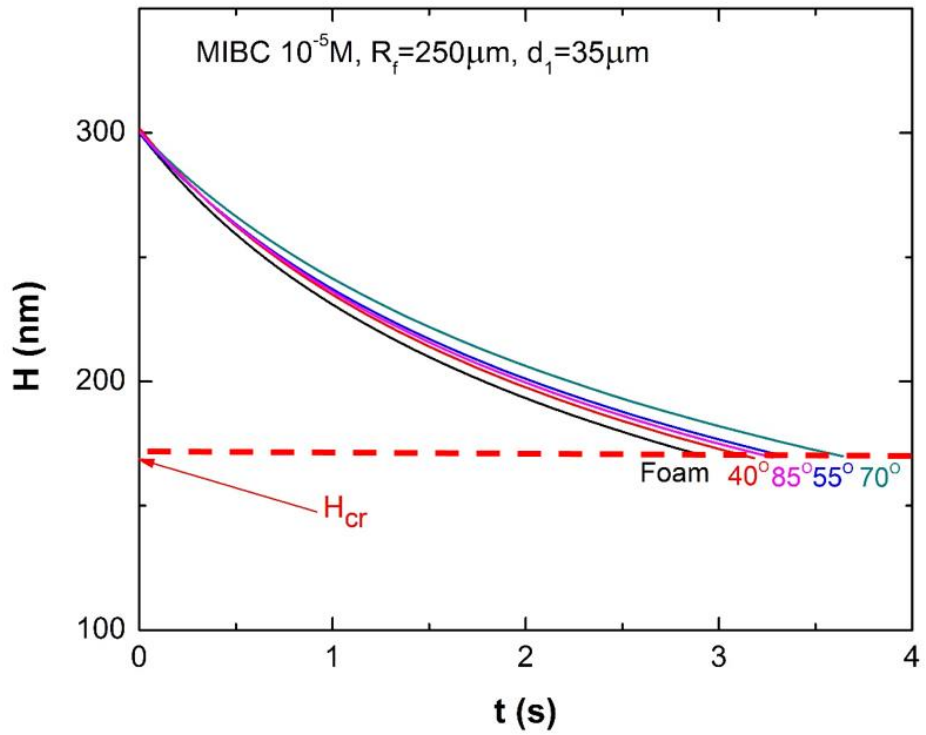

Figure 4.12 Effect of particle hydrophobicity on film thinning rate. The red line represents the critical rupture thickness (H_{cr}) of a 10^{-5}M MIBC foam film predicted from the H_{cr} model developed in Chapter 2.

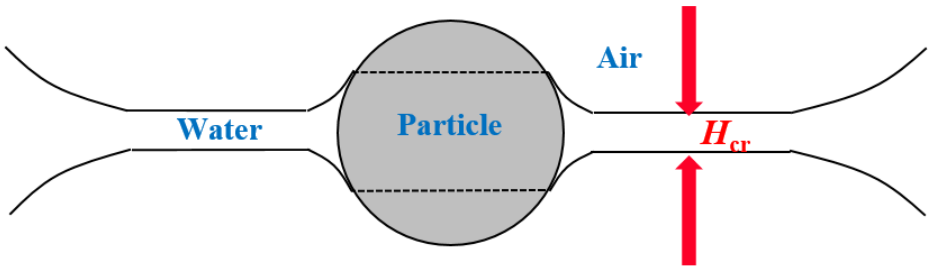

Figure 4.13 Rupture mechanism of a thin liquid film in the presence of a particle. The film rupture may occur in the free film at H_{cr}.

Figure 4.12 shows the film thinning kinetics of a foam film and froth films containing particles with θ = 40°, 55°, 70°, and 85°, respectively. We obtained the film thinning rates by using the calculated p values shown in Figures 4.6 and 4.11 into the Reynolds equation shown in Eq. (4.1). Note in Figure 4.12 that the foam film thins fastest when p is large. In the presence of particles, the thinning rate is retarded due to relatively smaller p. In the case of the foam film, it is obvious that it ruptures at its critical rupture thickness (H_{cr}), which was predicted to 171 nm in Section 4.4.1. The foam film, therefore, ruptures in 2.8 s. A question that may be raised here is how to predict the H_{cr} value for froth films and how to relate H_{cr} of a foam film to that a froth film. Until now, there has been no model for predicting H_{cr} of a froth film.

Figure 4.13 shows a proposed rupture mechanism of a froth film. It may be reasonable to assume that the film rupture occurs in the free film section of a froth film. Since the free film section is exactly same as a foam film, we assume in the present work that H_{cr} of a foam film and that of a froth film are identical. Accordingly, we can determine the critical rupture time (t_{cr}) of a

Table 4.2 The critical rupture time (t_{cr}) of a froth film predicted as a function of θ.

θ (°)	t_{cr} (s)
40	3.1
55	3.3
70	3.7
85	3.2

froth film at different θ, as shown in Table 4.2. It has been found that t_{cr} increases with θ, reaching a maximum at $\theta = 70°$, and then decreases with further increase in θ.

4.4.4 Prediction of Bubble Size Ratio ($d_{2,t}/d_{2,b}$) from t_{cr}

Figure 4.14 shows the schematic representation of a model for predicting the bubble size ratio ($d_{2,t}/d_{2,b}$) from t_{cr}. As a bubble rises along the y direction in a froth phase, the number of bubbles decreases due to bubble coarsening. The number of bubbles can be calculated by dividing the cross-sectional area (S) of a flotation cell by bubble diameter, *i.e.*, $4S/\pi d^2$. One can then write the following relation,

$$\frac{N_{\text{bubble,t}}}{N_{\text{bubble,b}}} = \frac{S/\pi(d_{2,\text{t}}/2)^2}{S/\pi(d_{2,\text{b}}/2)^2} = \left(\frac{d_{2,\text{b}}}{d_{2,\text{t}}}\right)^2 \tag{4.28}$$

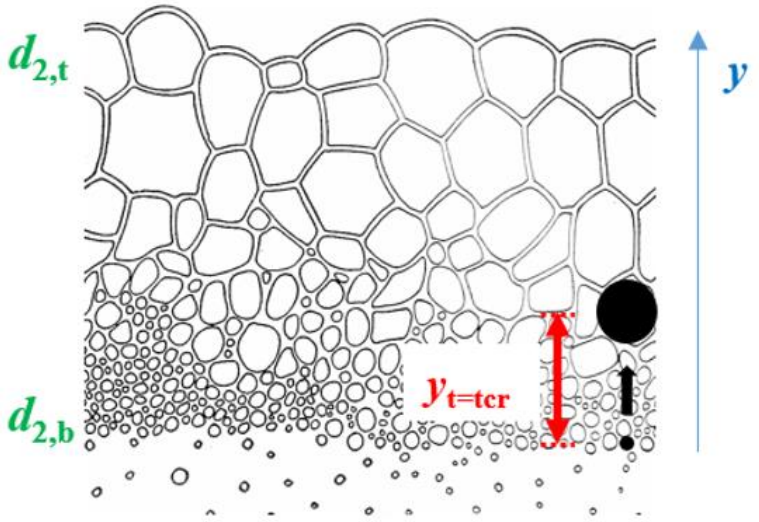

Figure 4.14 A model for predicting $d_{2,t}$ (bubble size at the top of the froth) from $d_{2,b}$ (the same at the base). A bubble created in the pulp arrives at the base at the terminal velocity of U_t. Then it starts to rise along the y direction at the velocity of U_{froth} and thin liquid films between bubbles starts to drain. At a critical rupture time (t_{cr}), the film ruptures and the rising bubbles coalesce.

where $N_{bubble,t}$ and $N_{bubble,b}$ are the bubble numbers at the top and bottom of a froth, respectively. Eq. (4.28) indicates that the bubble size ratio can be obtained if the bubble number ratio is predicted.

We assume that the number of bubbles decreases exponentially with froth height,

$$N_{bubble}(y) = N_{bubble,b} \exp(-C \frac{y}{h_f}) \tag{4.29}$$

where C is the decay constant, h_f is the froth height, and y is the distance from the base of a froth, which can be given by,

$$y = V_g t \tag{4.30}$$

where V_g is the superficial gas velocity and t is the time. Knowing that bubbles coalesce at the critical rupture time (t_{cr}), at which the film thickness reaches its H_{cr}, Eq. (4.29) can be rewritten as follows,

$$N_{bubble}(y_{t=t_{cr}}) = N_{bubble,b} \exp(-C \frac{y_{t=t_{cr}}}{h_f}) \tag{4.31}$$

In the process of bubble coalescence, the total volume of bubbles should be conserved. If a single thin liquid film between two bubbles of initial diameter d_i ruptures and thereby one bubble-coarsening event occurs, the diameter of the final bubble (d_f) should be $2^{1/3} d_i$. Therefore, one can obtain a more generalized relationship,

$$\frac{d_f}{d_i} = 2^{\frac{N_{rupture}}{3}} \tag{4.32}$$

in which d_i is the initial bubble diameter, d_f is the final bubble diameter, and $N_{rupture}$ is the number of film rupture for coarsening the bubble diameter from d_i to d_f.

Combining the relation shown in Eqs. (4.28) and (4.32), one can obtain the following equation,

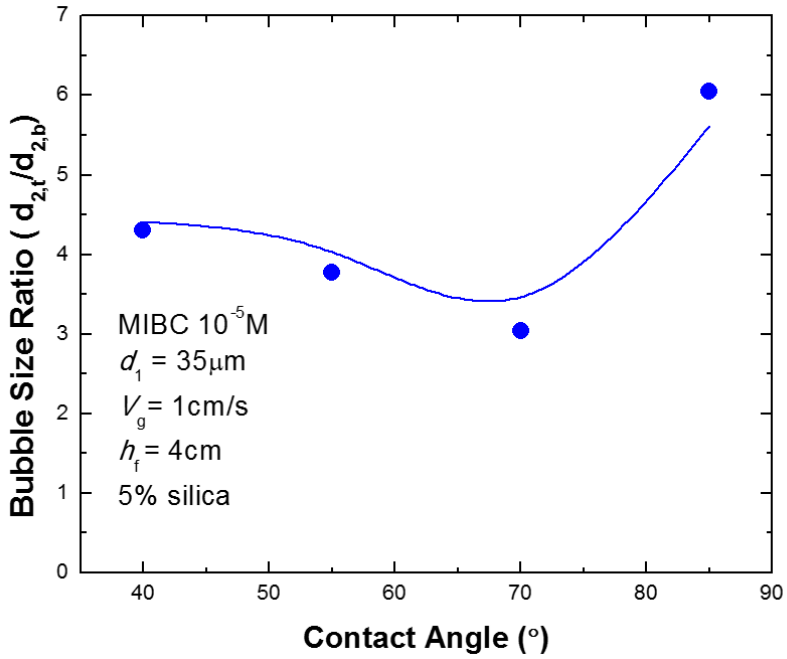

Figure 4.15 Bubble size ratio ($d_{2,t}/d_{2,b}$) as a function of particle contact angle (θ). The lines drawn through the experimental data points represent the model predictions.

$$\frac{N_{\text{bubble}}(y_{t=t_{cr}})}{N_{\text{bubble,b}}} = \left(\frac{d_{2,b}}{d_2(y_{t=t_{cr}})}\right)^2 = \left(2^{-\frac{N_{\text{rupture}}}{3}}\right)^2 \tag{4.33}$$

where N_{rupture} is the number of the films that rupture at $t = t_{cr}$ among 12 films consisting a dodecahedron-shaped bubble.

Then, by combining Eqs. (4.28) ~ (4.33), finally one can deduce the following model predicting the bubble size ratio,

$$\frac{d_{2,t}}{d_{2,b}} = \left[\exp\left(-\frac{0.46 h_f N_{\text{rupture}}}{t_{cr} V_g}\right)\right]^{-0.5} \tag{4.34}$$

In using Eq. (4.34) note that the values of h_f, t_{cr}, and V_g are known, while one needs to determine N_{rupture}. The values of N_{rupture} were back-calculated by fitting the model predictions using Eq. (4.34) to experimental results shown in Figure 4.5. In the present study, $N_{\text{rupture}} = 5$ was used at $\theta < 70°$,

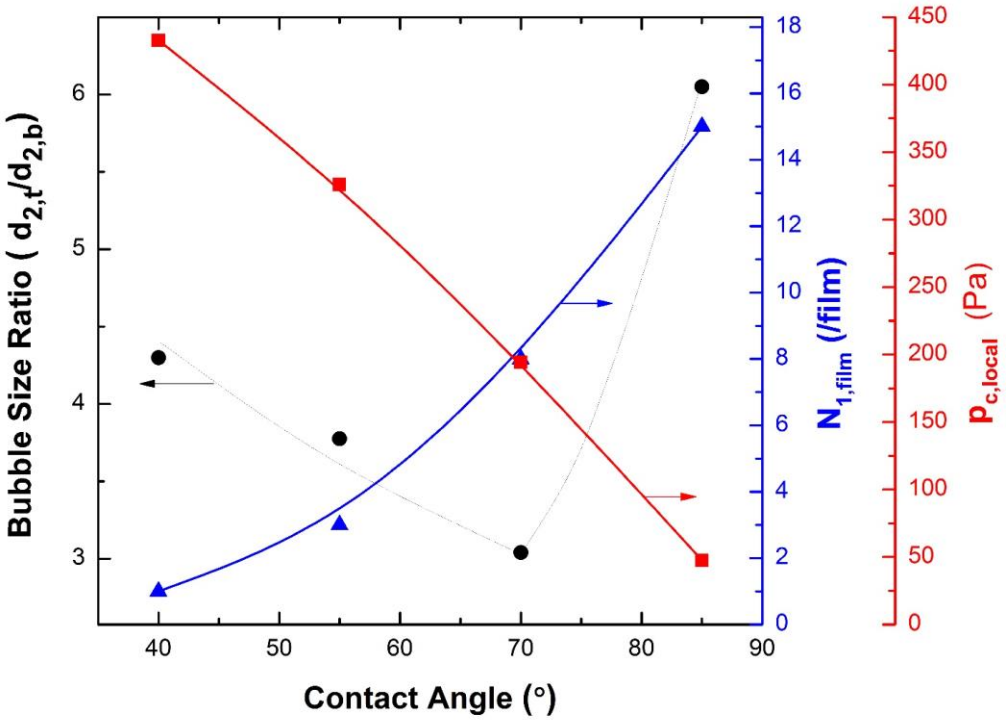

Figure 4.16 Effect of particle contact angle (θ) on bubble size ratio ($d_{2,t}/d_{2,b}$), the number of particles ($N_{1,film}$) in a froth film, and the local capillary pressure ($p_{c,local}$) around a particle. At θ <70° the increase in froth stability with increasing θ may be mainly due to the increase in $N_{1,film,}$ whereas at θ >70° the decrease in froth stability with increasing θ may be mainly due to the decrease in $p_{c,local}$.

while $N_{rupture}$ = 7 was assumed at θ = 85°. It indicates that more films ruptured at θ = 85°. This may be probably due to the possible existence of very hydrophobic particles (θ > 90°), which act as a foam breaker.

In Figure 4.15, the dots represent the experiential results shown in Figure 4.5 and the line represents the model predictions from Eq. (4.34). As shown, the model predictions are in good agreement with the experimentally measured $d_{2,t}/d_{2,b}$ values.

The model presented in the present work suggests that two independent parameters govern bubble–coarsening in a froth. One parameter is the number of particles ($N_{1,film}$) in a film, and the

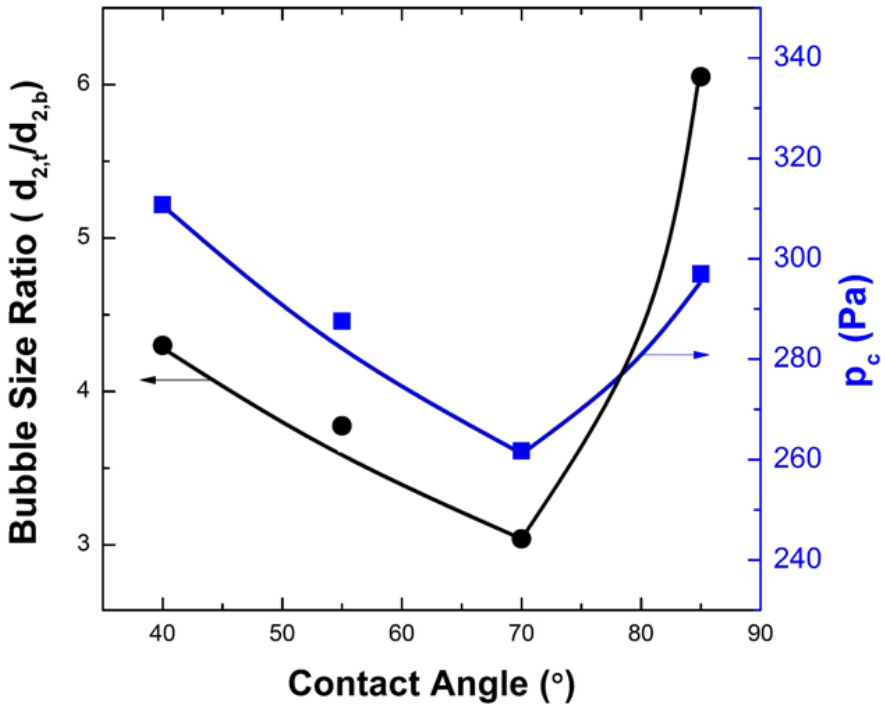

Figure 4.17 Effect of particle contact angle (θ) on bubble size ratio ($d_{2,t}/d_{2,b}$) and the capillary pressure (p_c) at the critical film thickness (H_{cr}).

other is the local capillary pressure ($p_{c,local}$) created by a single particle. The model shows that the higher the $N_{1,film}$ or the $p_{c,local}$, the lower the overall capillary pressure (p_c), resulting in a slower drainage rate and hence a higher froth stability. Figure 4.16 shows the changes in $N_{1,film}$ and $p_{c,local}$ with θ. Note here that at $\theta < 70°$, the decrease in $p_{c,local}$ with increasing θ can partially cause p_c to increase, but the effect of increasing $N_{1,film}$ may overcome the $p_{c,local}$ and hence decreases p_c. On the other hand, at $\theta > 70°$, with increasing θ, the decrease in $p_{c,local}$, countering the $N_{1,film}$ effect, causes p_c to decrease

As a result, as shown in Figure 4.17, it was found that the overall capillary pressure p_c significantly decreases with θ and begins to increase at $\theta = 70°$.

Figure 4.18 shows the effect of θ on driving force p for film drainage. This trend can give the explanation for the effect θ of on forth stability in terms of the drainage rate according to the Reynolds equation.

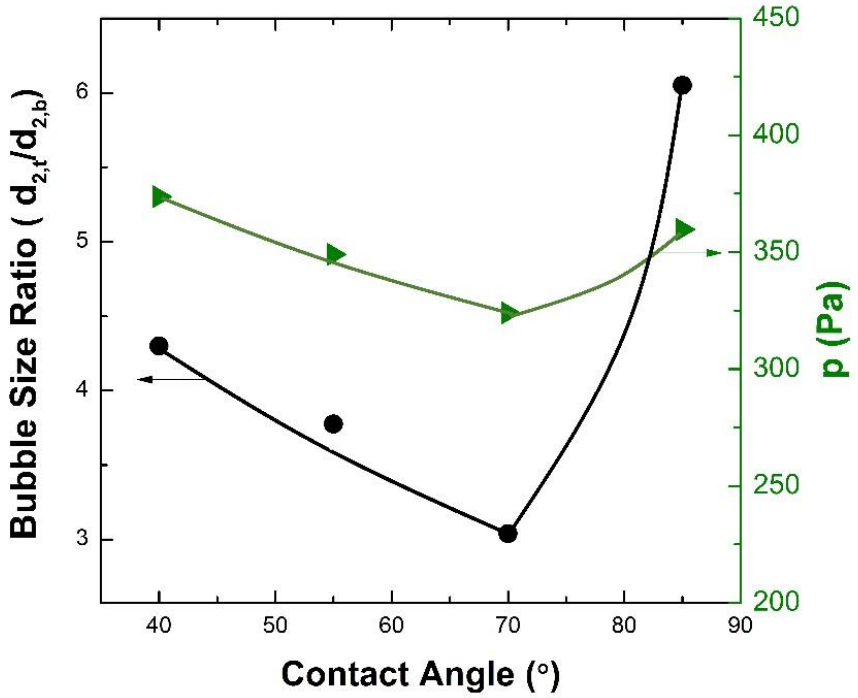

Figure 4.18 Effect of particle contact angle (θ) on bubble size ratio ($d_{2,t}/d_{2,b}$) and the driving pressure (p) for the film thinning at the critical film thickness (H_{cr}).

4.5 Summary and Conclusions

The effect of particle hydrophobicity (or water contact angle θ) on the bubble-coarsening (or froth stability) has been studied by measuring the bubble size ratio between the top and bottom of a forth in the presence of monosized (35μm) silica particles of varying hydrophobicity (θ = 40°, 55°, 70°, and 85°, respectively). It has been found that the froth stability increased with increasing θ, reached a maximum at θ = 70°, and decreased with further increase in θ.

In addition, we have developed a model for predicting the bubble-coarsening in a froth by deriving a film drainage model quantifying the effect of θ on the capillary pressure (p_c), which drives the drainage process. The parameter p_c is affected by the number of particles ($N_{1,film}$) in a film and the local capillary pressure ($p_{c,local}$) around particles, which in turn vary with θ. The model shows that as θ increases, $p_{c,local}$ decreases but $N_{1,film}$ increases sharply, causing p_c to decrease. As

a result, the film drains slower and the froth becomes more stable. However, at $\theta > 70°$, $p_{c,local}$ decreases too much, overcoming the effect of increased $N_{1,film}$ and thereby p_c begins to increase. As a consequence, the film drains faster and the froth becomes less stable.

References

[1] Fuerstenau, M.C., G.J. Jameson, and R.-H. Yoon, Froth flotation: a century of innovation. 2007: SME.

[2] Seaman, D.R., E.V. Manlapig, and J.P. Franzidis, Selective transport of attached particles across the pulp–froth interface. *Minerals Engineering*, 2006. **19**(6–8): p. 841-851.

[3] Reynolds, O., On the Theory of Lubrication and Its Application to Mr. Beauchamp Tower's Experiments, Including an Experimental Determination of the Viscosity of Olive Oil. *Proceedings of the Royal Society of London*, 1886. **40**(242-245): p. 191-203.

[4] Sheludko, A., Thin liquid films. *Advances in Colloid and Interface Science*, 1967. **1**(4): p. 391-464.

[5] Wang, L.Q. and R.H. Yoon, Role of hydrophobic force in the thinning of foam films containing a nonionic surfactant. *Colloids and Surfaces a-Physicochemical and Engineering Aspects*, 2006. **282**: p. 84-91.

[6] Donners, W.A.B. and A. Vrij, The critical thickness of thin free liquid films. *Colloid and Polymer Science*, 1978. **256**(8): p. 804-813.

[7] Vrij, A., Possible mechanism for the spontaneous rupture of thin, free liquid films. *Discussions of the Faraday Society*, 1966. **42**(0): p. 23-33.

[8] Vrij, A. and J.T.G. Overbeek, Rupture of thin liquid films due to spontaneous fluctuations in thickness. *Journal of the American Chemical Society*, 1968. **90**(12): p. 3074-3078.

[9] Wang, L. and R.-H. Yoon, Effects of surface forces and film elasticity on foam stability. *International Journal of Mineral Processing*, 2008. **85**(4): p. 101-110.

[10] Park, S., et al. Development of a model for bubble coarsening in a flotation froth. in *The 27th International Mineral Processing Congress* 2014. Santiago, Chile.

[11] Yoon, R.-H. and L. Mao, Application of extended DLVO theory, IV: derivation of flotation rate equation from first principles. *Journal of Colloid and Interface Science*, 1996. **181**(2): p. 613-626.

[12] Wang, L. Inter-bubble attractions in aqueous solutions of flotation frothers. in *SME Annual Meeting*. 2011. Denver, CO, United States.

[13] Ip, S.W., Y. Wang, and J.M. Toguri, Aluminum foam stabilization by solid particles. *Canadian Metallurgical Quarterly*, 1999. **38**(1): p. 81-92.

[14] Aktas, Z., J.J. Cilliers, and A.W. Banford, Dynamic froth stability: Particle size, airflow rate and conditioning time effects. *International Journal of Mineral Processing*, 2008. **87**(1–2): p. 65-71.

[15] Tang, F.-Q., et al., The effect of SiO2 particles upon stabilization of foam. *Journal of Colloid and Interface Science*, 1989. **131**(2): p. 498-502.

[16] Johansson, G. and R.J. Pugh, The influence of particle size and hydrophobicity on the stability of mineralized froths. *International Journal of Mineral Processing*, 1992. **34**(1–2): p. 1-21.

[17] Ata, S., N. Ahmed, and G.J. Jameson, A study of bubble coalescence in flotation froths. *International Journal of Mineral Processing*, 2003. **72**(1–4): p. 255-266.

[18] Binks, B.P., Particles as surfactants - similarities and differences. *Current Opinion in Colloid & Interface Science*, 2002. **7**(1-2): p. 21-41.

[19] Denkov, N.D., et al., A Possible Mechanism of Stabilization of Emulsions by Solid Particles. *Journal of Colloid and Interface Science*, 1992. **150**(2): p. 589-593.

[20] Wang, L.G. and R.H. Yoon, Hydrophobic forces in thin aqueous films and their role in film thinning. *Colloids and Surfaces a-Physicochemical and Engineering Aspects*, 2005. **263**(1-3): p. 267-274.

[21] Morris, G., S.J. Neethling, and J.J. Cilliers, Predicting the Failure of a Thin Liquid Film Loaded with Spherical Particles. *Langmuir*, 2014. **30**(4): p. 995-1003.

[22] Morris, G., et al., The effect of particle hydrophobicity, separation distance and packing patterns on the stability of a thin film. *Journal of Colloid and Interface Science*, 2008. **327**(1): p. 138-144.

[23] Morris, G.D.M., S.J. Neethling, and J.J. Cilliers, A Model for the Stability of Films Stabilized by Randomly Packed Spherical Particles. *Langmuir*, 2011. **27**(18): p. 11475-11480.

[24] Feitosa, K. and D.J. Durian, Gas and liquid transport in steady-state aqueous foam. *The European Physical Journal E*, 2008. **26**(3): p. 309-316.

[25] Comley, B.A., et al., Frother characterisation using dynamic surface tension measurements. *International Journal of Mineral Processing*, 2002. **64**(2-3): p. 81-100.

[26] Srinivas, A. and P. Ghosh, Coalescence of bubbles in aqueous alcohol solutions. *Industrial & Engineering Chemistry Research*, 2011. **51**(2): p. 795-806.

[27] Wang, L. and R.-H. Yoon, Role of hydrophobic force in the thinning of foam films containing a nonionic surfactant. *Colloids and Surfaces A: Physicochemical and Engineering Aspects*, 2006. **282**: p. 84-91.

Chapter 5. Modeling Froth Stability: Effect of Particle Size

ABSTRACT

A lamella film formed between two bubbles in a flotation froth drains due to the capillary pressure (p_c) and the disjoining pressure (Π). When the film breaks, the two bubbles become one and the bubble size becomes coarser. In the present work, the effect of particle size (d_1) on the bubble-coarsening (or froth stability) was investigated. The study was conducted by measuring the bubble size ratio between the top and bottom of a forth in the presence of different sizes of particles (d_1 = 11, 35, 71, and 119 μm). It was found that the froth stability decreases considerably as particle size becomes coarser from 11 to 71 μm. However, as particle size increases further to 119 μm, the froth stability changes little.

In the present work, a model for predicting the bubble-coarsening in a froth has also been developed by deriving a film drainage model quantifying the effect of d_1 on p_c. The model indicates that as d_1 increases, p_c increases and thereby the film thins faster and the froth becomes unstable.

5.1 Introduction

As bubbles migrate upward in a froth phase, they coalesce with each other and become larger. As bubbles become larger, bubble surface area becomes smaller, restricting the number of hydrophobic particles that can be carried upward and flow into a launder. On the other hand, in the process of the bubble coarsening, less hydrophobic particles tend to be removed more easily, it can contribute to increase the grade of a froth product [1]. Thus, the throughput of a flotation cell depends on bubble coarsening. Therefore, it is important to understand the basic mechanisms of bubble coarsening and froth (or foam) stability.

A foam is thermodynamically unstable due to the large surface area, which means high surface energy. Therefore, in pure water air bubbles collapse immediately to reduce the free energy. It is generally known that surfactants enhance the foam stability. When a surfactant adsorbs at air/water interface, it can reduce the thermodynamic instability by lowering the surface energy. In the case of an ionic surfactant, it can also enhance the foam stability by increasing the electrostatic repulsion force acting between two air/water interfaces and thereby regarding the film thinning.

It is known that a solid particle can also act as a surfactant. A froth is a three-phase foam, where particles are present and a froth is generally more stable than a foam due to the presence of particles [2-5]. It has been reported that the froth stability depends on particle properties, including surface hydrophobicity [2, 3, 5-7], shape [8], concentration [2], and size [2-4].

With regard to particle size (d_1) effect, several experiential studies have been reported. Tang *et al*. [4] have found that smaller particles can increase the froth stability. They used silica particles of $d_1 < 770$ nm, which is relatively fine as compared to flotation practice. Johansson and Pugh [5] conducted static and dynamic froth stability tests in the presence of fine (26 ~ 44 μm) and coarse (74 ~ 106 μm) quartz particles with alcohol type frothers. They also found that generally fine particles can cause higher stabilizing effect, but how the change in d_1 affect the froth stability was explained. Ip *et al*. [2] have measured the froth life time, as indicator of the froth stability, in a flotation column in the presence of silica particles (40 μm < d_1 < 150 μm) while the volume faction of particles in the slurry was kept constant. They also observed that the froth stability increases as d_1 decreases. It was suggested that at a constant volume faction, as d_1 decreases, the number of particles in the slurry and the collection efficiency can increases, which will result in

the high surface coverage of a bubble by particles. They assumed that the higher surface coverage by finer particles can enhance the froth stability. More recently, Aktas and his co-workers [3] also have shown that fine particles benefit the froth stability through dynamic stability tests. However, up to now, there is no theoretical model that can explain the influence of particle size on the froth stability.

Fortunately, we have recently developed a froth model for predicting bubble coarsening in a froth phase as a function of particle size. The model is based on the recognition that particles can reduce the capillary pressure (p_c), which contribute to thin a liquid film formed between bubbles in a froth. As a result, particles can decrease the film drainage rate and thereby enhance the froth stability. The model is also based on the premise that parameter p_c is affected by the number of particles and the local capillary pressure ($p_{c,local}$) around particles, which vary with particle size in the film.

In the present work, the model was verified by comparison with our experiments testing the influence of particle size on froth stability. We have conducted a series of laboratory-scale flotation experiments with 10^{-5} M methyl-isobutyl carbinol (MIBC) solutions in the presence of silica particle of different sizes (d_1 = 11, 35, 71, and 119 μm). In each experiment, the bubble size ratio ($d_{2,t}/d_{2,b}$), the ratio of average bubble diameter at the top of the froth ($d_{2,t}$) and to the same at the base of the froth ($d_{2,b}$), as a measure of the froth stability, was calculated.

5.2 Experiment

5.2.1 Materials and Hydrophobization of Silica Surfaces

In the present study, to investigate the influence of particle size on froth stability, four different diameters (d_1 = 11, 35, 71, and 119 μm) of silica spheres (Potters industries) were treated, respectively. First, silica particles of identical size and a reference silica plate were cleaned by immersing them in boiling Piranha solution (H_2O_2/H_2SO_4 3: 7 by volume) for 1 h. Then they were rinsed in ultrapure water for 10 min and subsequently allowed to dry thoroughly in an oven at 160 ℃ overnight. After that, the cleaned surfaces of both the particles and the plate were simultaneously hydrophobized by soaking them together in 10^{-4} M octadecyltrichlorosilane (OTS, 95% purity, Alfa Aesar)-in-toluene (99.9% purity, Spectrum Chemical) solution. After

hydrophobization, they were washed with chloroform (99.9% purity, Fisher Chemical), acetone (99.9 % purity, Aldrich), and ultrapure water, sequentially. Due to the same conditioning time of the particles and the plate, it may reasonable to assume that they exhibit the identical water contact angles (θ). Hence, the θ value of the particles were simply estimated by measuring that of the plates using a goniometer (Rame-hart instrument co.). By varying the immersion time in 10^{-4} M OTS-in-toluene, the θ value was controlled. Until θ reaches 40°, by repeating the procedure stated above, four different diameters (d_1 = 11, 35, 71, and 119 μm) of silica spheres with θ = 40° were prepared prior to experiments.

5.2.2 Experimental Procedure

In the present study, we have carried out flotation tests by means of a Denver laboratory flotation machine. A 1.5 L of transparent glass cell was specially made to observe bubble-coarsening phenomena in a froth phase clearly. The cell was built with flat plates to reduce optical distortion. Prior to each experiment the cell was cleaned thoroughly with distilled water. The cell was, then, filled with 10^{-5} M methyl-isobutyl carbinol (MIBC, 98% purity, Aldrich) aqueous solution. Before generating air bubbles, the 60 g silica particles (solids concentration of 5% w/w) of an identical size were added to the MIBC solution and stirred at the rotation speed of 900 rpm for 5 min for wetting. After that, a froth phase was created by injecting air to the cell at the superficial gas velocity of 1 cm/s. The formed froth was allowed to overflow and then recirculated to the cell using a peristaltic pump. The froth height was adjusted to be 4 cm by controlling the pulp-froth level. During the experiment, the bubble images in a froth were recorded using a high-speed camera (Fastec imaging). We repeated the experiments with changing particle sizes. Additionally, an experiment was conducted in the absence of particles for comparison with foam stability.

After the flotation tests, the Sauter mean bubble diameter at the base of the froth ($d_{2,b}$) and the same at the top ($d_{2,b}$) were calculated by analyzing the acquired images by means of BubbleSEdit, image-analysis software. Finally, the bubble size ratio ($d_{2,t}/d_{2,b}$) of each particle size was obtained.

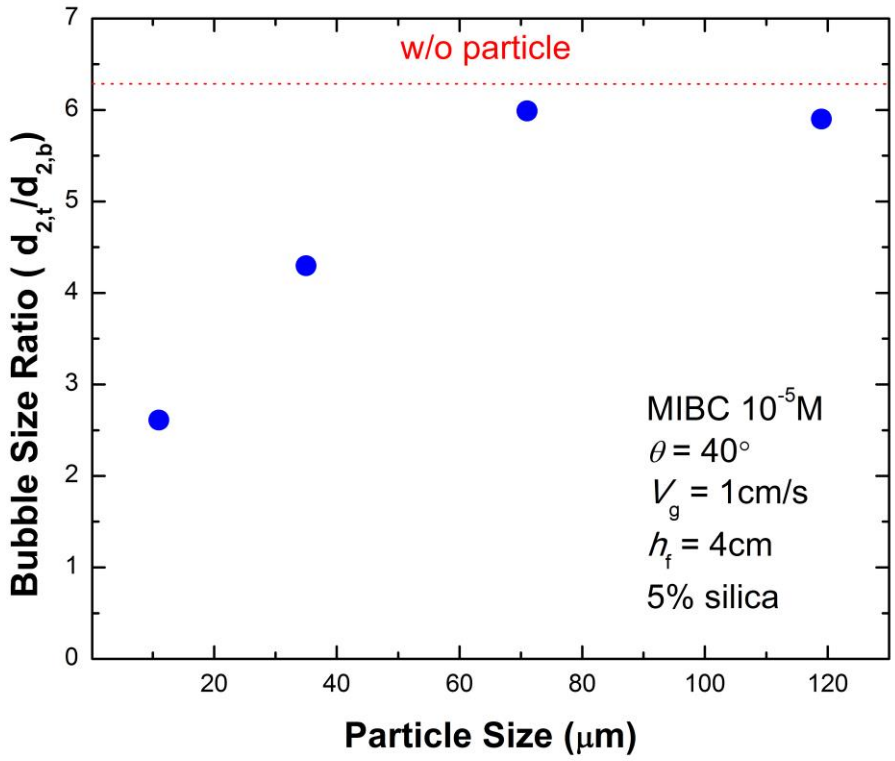

Figure 5.1 The bubble size ratio ($d_{2,t}/d_{2,b}$) measured in the presence of different sizes of particles at θ = 40°. The dotted line represents $d_{2,t}/d_{2,b}$ in the absence of particles.

5.3 Experimental Result

Figure 5.1 shows the values of experimentally measured bubble size ratio ($d_{2,t}/d_{2,b}$) in the absence of particles and in the presence of particles of different sizes at θ = 40°. It should be reasonable to assume that the higher $d_{2,t}/d_{2,b}$ indicates the lower froth stability. As shown, it was observed that froth stability decreases considerably as particle size becomes coarser from 11 to 71 μm. As particle size increases further to 119 μm, the froth stability changes little. It is also noticeable that in the present experimental range the $d_{2,t}/d_{2,b}$ values of the froth were lower as compared to the foam phase. It indicates that particles at θ = 40° can stabilize bubbles or thin liquid films between the bubbles over wide range of particle sizes.

5.4 Theoretical Approach and Discussion

In this section, we analyze the experiential results with the theoretical bubble-coarsening froth model presented in Chapter 4. Theoretically, how particle size affects a froth stability is explained. In the process, the bubble-coarsening froth model is verified by the comparison with the experimentally measured bubble size ratio ($d_{2,t}/d_{2,b}$) presented in Section 5.3.

5.4.1 Number of Particles in a Froth Film

In Chapter 4, the $N_{1,film}$ (the number of particles in the film) was given by the following expression,

$$N_{1,film} = N_{1,seg} P_c P_a (1 - P_d) \tag{5.1}$$

where P_c is the probability of collision, P_a the probability of attachment, and P_d the probability of detachment, and $N_{1,seg}$ the number of particles having a chance to collide with a bubble surface

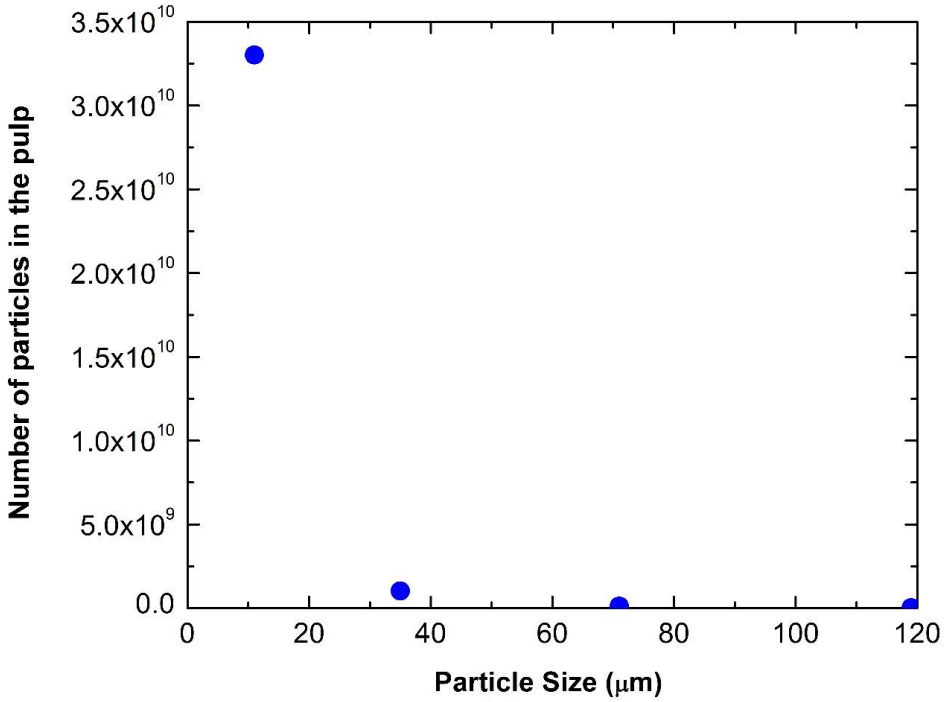

Figure 5.2 The number of injected particles in the pulp vs. particle sizes (d_1).

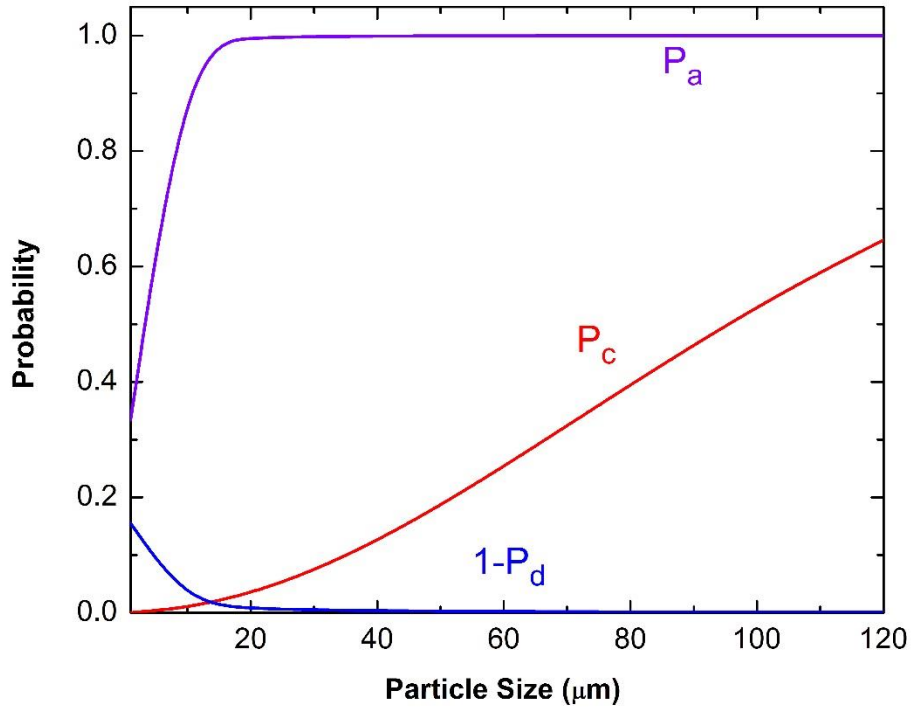

x

Figure 5.3 Effect of particle sizes on the probability of collision (P_c), the probability of attachment (P_a), and the probability of detachment (P_d), respectively.

segment in pulp phase ending up a single lamella film in the froth phase. The value of $N_{1,seg}$ may be proportional to the number of particles suspending in the pulp, $N_{1,pulp,}$

$$N_{1,seg} = cN_{1,pulp} \tag{5.2}$$

where c is the proportionality constant, which may vary with the cell dimensions and the number of bubbles in the pulp. In using Eq. (5.2), the value of $N_{1,pulp}$ can be calculated by dividing the total mass of particles injected to the cell (m_1) by a mass of a single particle,

$$N_{1,pulp} = \frac{m_1}{\rho_1 \frac{4}{3}\pi\left(\frac{d_1}{2}\right)^3} \tag{5.3}$$

Table 5.1 Input parameters for the simulation shown in Figure 5.3.

Frother (MIBC) concentration (M)	10^{-5}
Solids concentration (% w/w)	5
Specific power (kW/m^3)	22.8
Superficial gas rate (cm/s)	1.0
Froth height (cm)	4
Particle contact angle (°)	40
Particle Zeta potential (mV)	-0.08
Bubble Zeta potential (mV)	-0.03

where ρ_1 is the density of the particle. In the present experiment, m_1 was set to 60 g and ρ_1 of silica was 2.65 g/cm^3. As shown in Figure 5.2, with increasing d_1, $N_{1,pulp}$ sharply decreases as d_1^{-3}.

The plots of probability functions (P_c, P_a, and P_d) were then drawn as a function of d_1 in Figure 5.3 and input parameters used for the calculations were listed in Table 5.1. While only the values of particle zeta potential was assumed, the bubble zeta potential was obtained from Comley *et al.*'s study [9] and the others were measured in experiments.

Figure 5.4 shows the values of $P_cP_a(1-P_d)$ obtained from Figure 5.3. It was found that fine particles are less unlikely to survive in the pulp due to lower P_c and P_a, while coarse particles are less unlikely to survive in the pulp due to higher P_d.

Finally, as shown in Figure 5.5, the values of $N_{1,film}$ were obtained by substituting Eqs. (5.2) and (5.3) into (5.1). In using (5.2), the value of c was arbitrary chosen to 384244. It was found that $N_{1,film}$ decreases as d_1 increases. The $N_{1,film}$ values shown in Figure 5.5 were used to calculate the driving force for froth films in the following section.

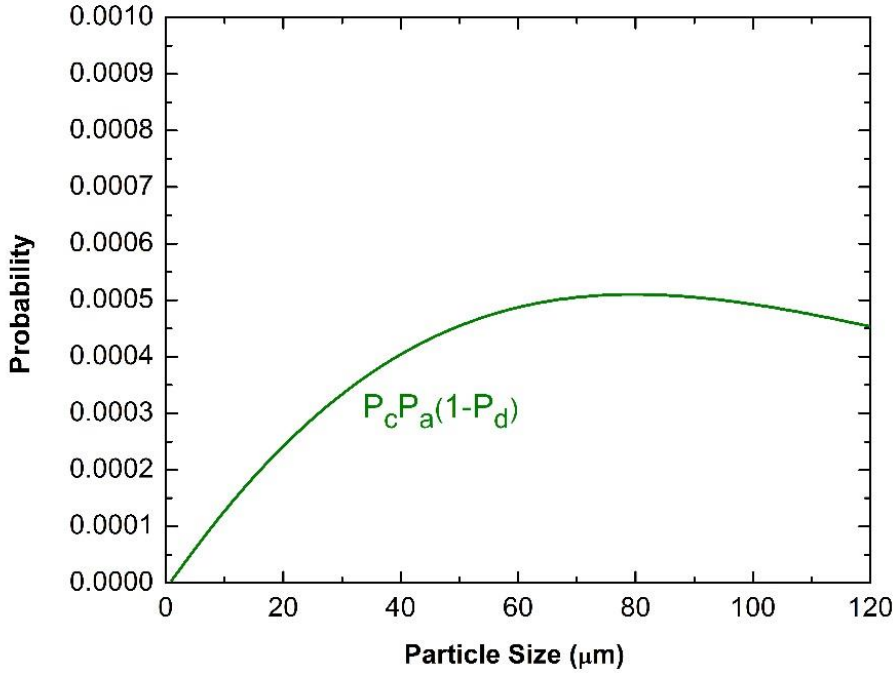

Figure 5.4 Effect of particle sizes on the probability of particles surviving in a pulp phase, $P_c\ P_a\ (1\text{-}P_c)$.

5.4.2 Driving Force for a Froth Film Thinning

To calculate the driving force (p) for froth films, the methodology presented in Chapter 4 was used. Figure 4.8 shows the schematic of a layer of particles located in the film. The thinning velocity of a froth film may be obtained by the Reynolds lubrication equation [10],

$$\frac{dH}{dt} = -\frac{2H^3 p}{3\mu R_f^2} \tag{5.4}$$

where H is the film thickness, t the drainage time, μ the dynamic viscosity, R_f the film radius, and p the driving force for film thinning and can be expressed as,

$$p = p_c - \Pi \tag{5.5}$$

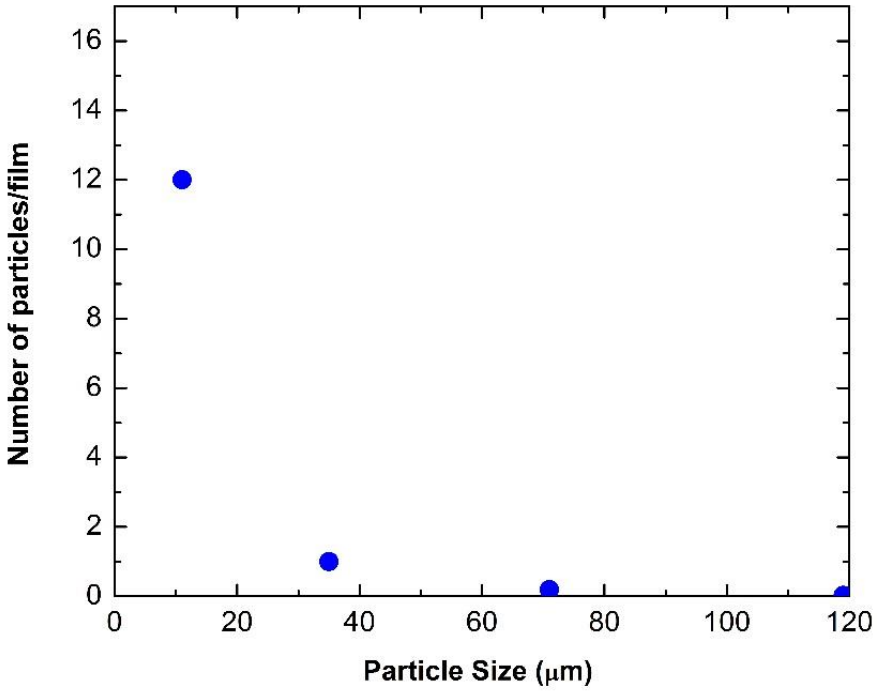

Figure 5.5 The number of particles residing in a froth film ($N_{1,\text{film}}$) predicted as a function of particle sizes (d_1).

in which p_c and Π are the contributions from capillary pressure and the disjoining pressure, respectively.

In using Eq. (5.5), p_c is defined as follows,

$$p_c = \frac{\text{Overall capillary force}}{\text{Film area}} = \frac{p_I A_I N_{1,\text{film}} + p_{II} A_{II}}{A_I N_{1,\text{film}} + A_{II}} \tag{5.6}$$

where A_I and A_{II} are areas of section I and II, respectively and p_I and p_{II} are the capillary pressure acting in Section I and II, respectively. The values of p_I and p_{II} were expressed as, respectively,

$$p_I = \frac{2\gamma}{R} - p_{c,\text{local}} \tag{5.7}$$

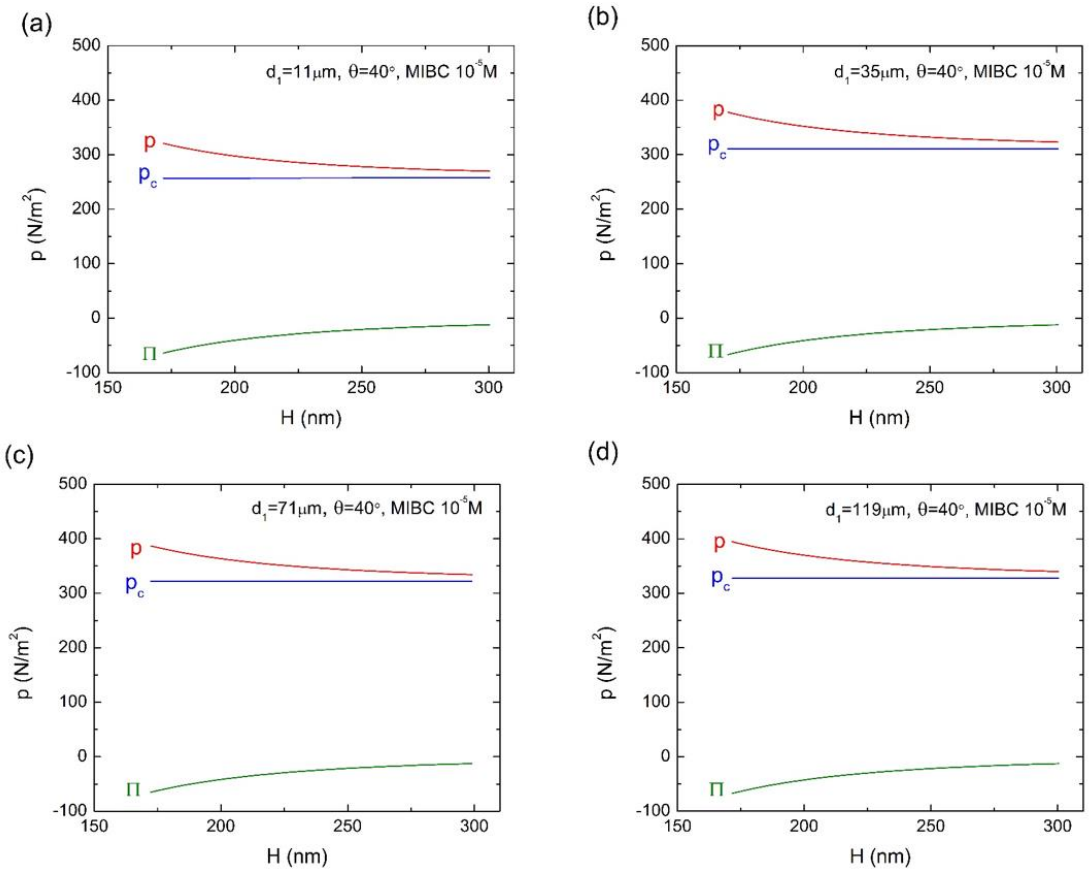

Figure 5.6 The changes in driving pressure (p), capillary pressure (p_c), and disjoining pressure (Π) as a function of the thickness (H) of a film containing particles with sizes (d_1) of (a) 11 μm, (b) 35 μm, (c) 71 μm, and (d) 119 μm. The values of K_{232} = 2.3×10^{-19} J, A_{232}= 4×10^{-21} J, R = 0.44 mm, γ = 0.0724 N/m, T = 298 K, e = 1.6 ×10^{-19} C, ψ_s = -30 mV, and κ^{-1}= 30 nm were used.

$$p_{II} = \frac{2\gamma}{R} \tag{5.8}$$

where γ is the surface tension, R is the bubble radius, and $p_{c,local}$ is the local capillary pressure arising from the interface deformation by particle absorption. The value of $p_{c,local}$ were calculated using Denkov *et al.*'s model [11].

On the other hand, in using Eq. (5.5), Π is defined as,

$$\Pi = \frac{\text{Overall surface force}}{\text{Film area}} = \frac{\Pi_I A_I N_{particle} + \Pi_{II} A_{II}}{A_{II}} \approx \Pi_{II} \tag{5.9}$$

where Π_I and Π_{II} are the disjoining pressure arising in section I and II, respectively. The values of Π_I and Π_{II} were expressed as, respectively,

$$\Pi_I = \frac{\int_{r_c}^{b} \Pi(r)(2\pi r)dr}{A_I} \approx 0 \tag{5.10}$$

$$\Pi_{II} = \Pi_{el} + \Pi_{vw} + \Pi_{hp} = 64 C_{el} RT \tanh^2\left(\frac{e\psi_s}{4kT}\right)\exp(-\kappa H) - \frac{A_{232}}{6\pi H^3} - \frac{K_{232}}{6\pi H^3} \tag{5.11}$$

where Π_{el} is the disjoining pressure due to electrostatic interaction, Π_{vw} is the disjoining pressure due to van der Waals dispersion force, Π_{hp} is the disjoining pressure due to hydrophobic force, C_{el} is the electrolyte concentration, R_2 the gas constant, T the absolute temperature, e the electronic charge (e = 1.6 ×10^{-19} C), ψ_s the surface potential at the air/water interfaces, k the Boltzmann's

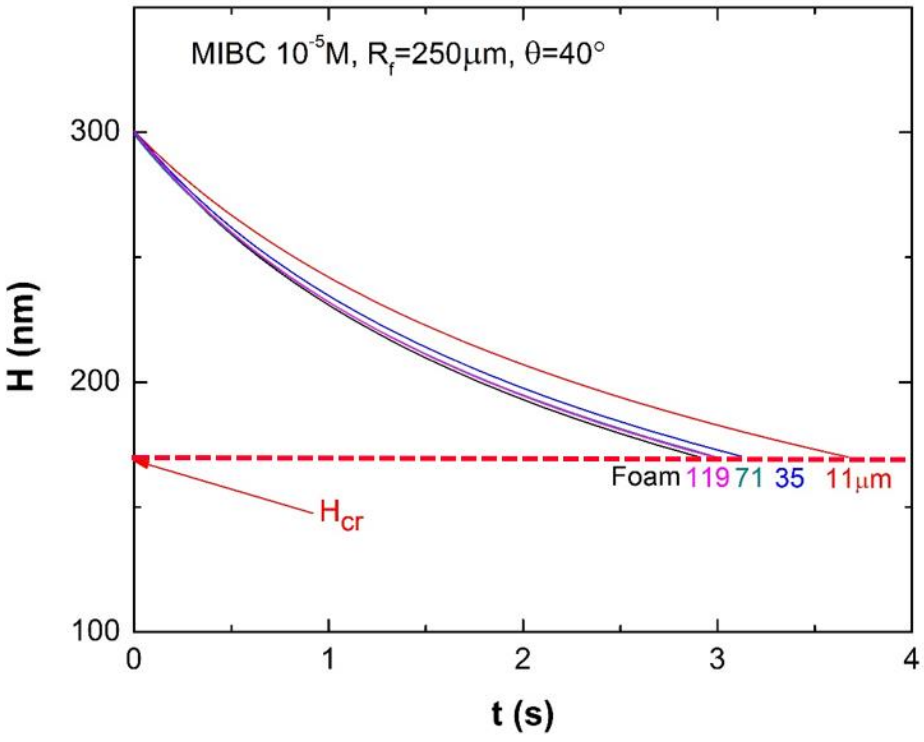

Figure 5.7 Effect of particle size on film thinning rate. The red line represents the critical rupture thickness (H_{cr}) of a 10^{-5}M MIBC foam film predicted from the H_{cr} model developed in Chapter 2.

constant, κ the reciprocal Debye length, A_{232} the Hamaker constant, and K_{232} the hydrophobic constant.

Figure 5.6 shows the effect of d_1 on p, p_c, and Π. In the calculations, T = 298 K was used from the measurement in the experiment. The values of γ = 0.0724 N/m and ψ_s = -30 mV were used as reported by Comley *et al*. [9] and Srinivas *et al*. [12], respectively. Also the values of K_{232} = 2.3×10^{-19} J and A_{232}= 4×10^{-21} J were used as reported by Wang [13]. Only the value of κ^{-1}= 30 nm was assumed. As shown, p_c increases as d_1 becomes larger from 11 to 71μm. As d_1 increases further to 119 μm, p_c changes little. Since the value of Π is independent of d_1, the change in p_c dominate the variation of p. Note in Figure 5.5 that the variation trend of p with d_1 is similar with that of $d_{2,t}/d_{2,b}$.

5.4.3 The Critical Rupture Time (t_{cr}) of a Froth Film

As shown in Figure 5.7, substituting the p values obtained in Figure 5.6 into Eq. (5.4), we calculated the film thinning rates of films containing particles of d_1 = 11, 35, 71, and 119 μm, respectively. In the calculation, assuming that a bubble has a dodecahedron structure, R_f was calculated to 250 μm from the following geometrical considerations,

$$R_f = R/\sqrt{3} \tag{5.12}$$

in which R was 0.44 mm as measured at the base of the froth (or foam) in this study. It is noticeable that the thinning velocity of the film containing particles of d_1 =11 μm is the slowest, which is attributed to the smallest p values. As d_1 gets coarser to 35 μm, the thinning rate becomes significantly slower, mostly due to the significant decrease in p_c. As d_1 becomes coarser to 71 μm, the thinning rate becomes little slower, mostly due to small decrease in p_c. It was also found that the thinning rates of d_1 = 71 μm and 119 μm are almost same due to similar p values.

As presented in Chapter 2, in the present work, the critical rupture thickness (H_{cr}) of the foam film were predicted by incorporating the hydrophobic force into the capillary wave theory,

$$144\gamma\left\{3H_m^{-4}\left(\left.\frac{\partial\Pi}{\partial H}\right|_{H=H_m}\right)^{-2}-2H_m^{-3}\left(\left.\frac{\partial\Pi}{\partial H}\right|_{H=H_m}\right)^{-3}\left.\frac{\partial^2\Pi}{\partial H^2}\right|_{H=H_m}\right\}-\frac{3H_m^{-3}R_f^{2}}{2(p_c-\Pi)}=0 \qquad (5.13)$$

$$H_{cr}=0.845H_m$$

The model prediction from Eq. (5.13) showed that H_{cr} of the 10^{-5} M MIBC foam film of R_f = 250 μm is 171 nm. In the present study, it is assumed that the film in the presence of particles has the identical H_{cr} values as compared to the foam film, due to the hypothesis that the film rupture of the froth film may happen in the free film section, which is similar with a foam film. Consequently, the values of the critical rupture time (t_{cr}) of the froth film was obtained as a function of d_1, as shown in Figure 5.8.

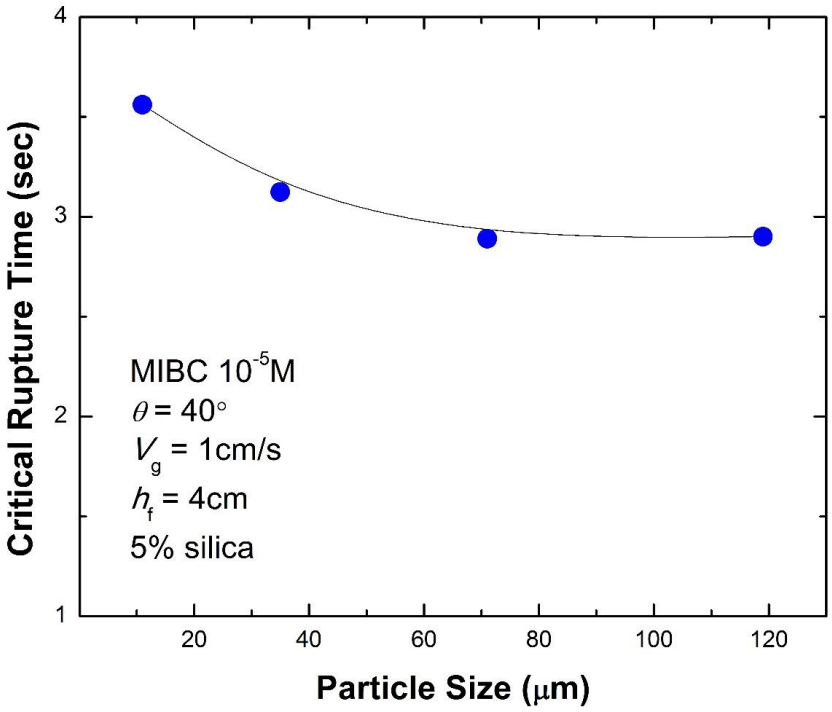

Figure 5.8 The critical rupture time (t_{cr}) of a froth film predicted as a function of particle size.

5.4.4 Prediction of Bubble Size Ratio ($d_{2,t}/d_{2,b}$) from t_{cr}

In Chapter 4, a theoretical model for predicting bubble size ratio ($d_{2,t}/d_{2,b}$) from t_{cr} was derived, as follows,

$$\frac{d_{2,t}}{d_{2,b}} = \left[\exp\left(-\frac{0.46 h_f N_{rupture}}{t_{cr} V_g} \right) \right]^{-0.5} \tag{5.14}$$

where h_f is the froth height, V_g is the superficial gas rate, and $N_{rupture}$ is the number of the films that rupture at t_{cr} among 12 films forming a dodecahedron-shaped bubble. In using Eq. (5.14), the values of h_f, t_{cr}, and V_g are known, $N_{rupture}$ needs to be determined. $N_{rupture}$ was assumed to be 5. at d_1 = 11 and 35 μm. At d_1 =71 and 119 μm, however, based on the recognition that possibly more films could rupture at t_{cr} due to the increase of the area occupied by free film with small particle

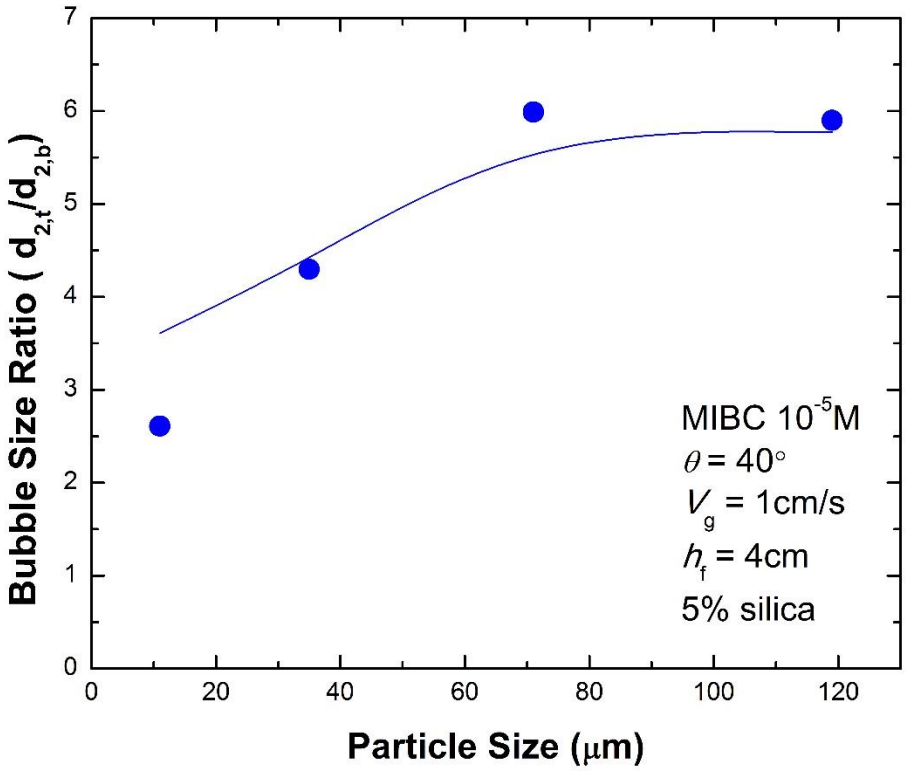

Figure 5.9 Bubble size ratio ($d_{2,t}/d_{2,b}$) as a function of particle size (d_1). The lines drawn through the experimental data points represent the model predictions.

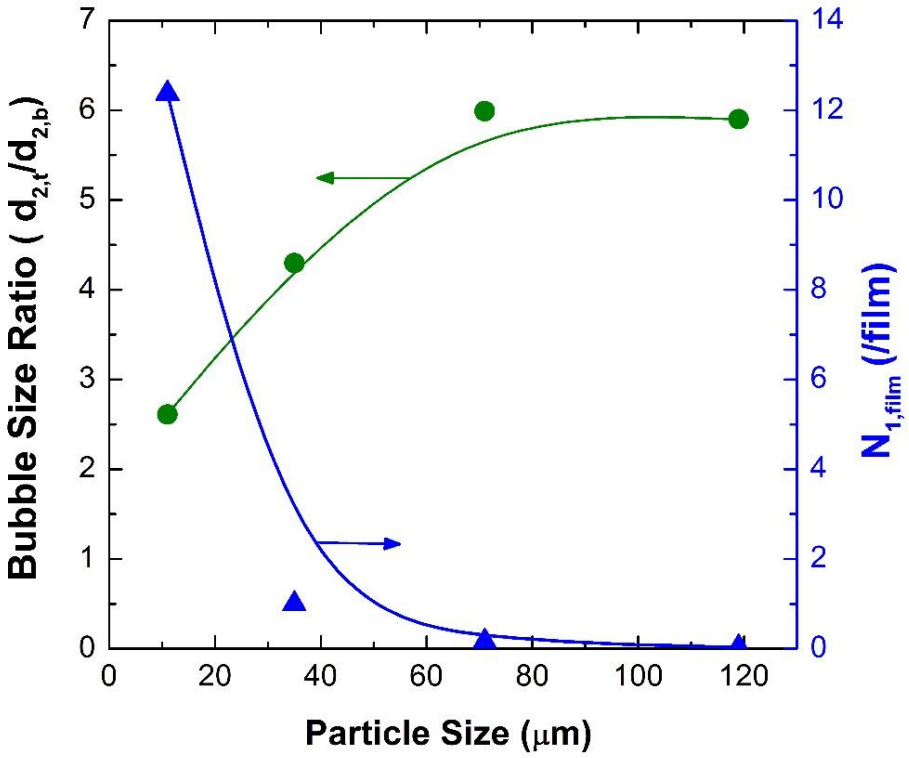

Figure 5.10 Effect of particle size (d_1) on bubble size ratio ($d_{2,t}/d_{2,b}$) and the number of particles in a froth film ($N_{1,film}$). The increase in $d_{2,t}/d_{2,b}$ with increasing d_1 may be partially attributed to the decrease in $N_{1,film}$.

number, slightly higher value ($N_{rupture}$ = 5.5) was used. As shown in Figure 5.9, the model predictions agree with the experimental results.

In Chapter 4, it was found that two independent parameters determine the value of $d_{2,t}/d_{2,b}$. One parameter is the particle number in a film ($N_{1,film}$) and the other is the local capillary pressure ($p_{c,local}$) around a particle. The increase in both parameters causes the overall capillary pressure p_c to decrease, resulting in decrease in driving force p and drainage rate. It was found in the present work that the two parameters vary with particle size as shown in Figure 5.10 and 5.11, respectively. Note in Figure 5.10 that $N_{1,film}$ decreases as a particle become coarser, which may partially attribute to the increase in overall capillary pressure p_c. Note in Figure 5.11 that $p_{c,local}$ decreases as a particle become coarser, which may also partially attribute to the increase in p_c.

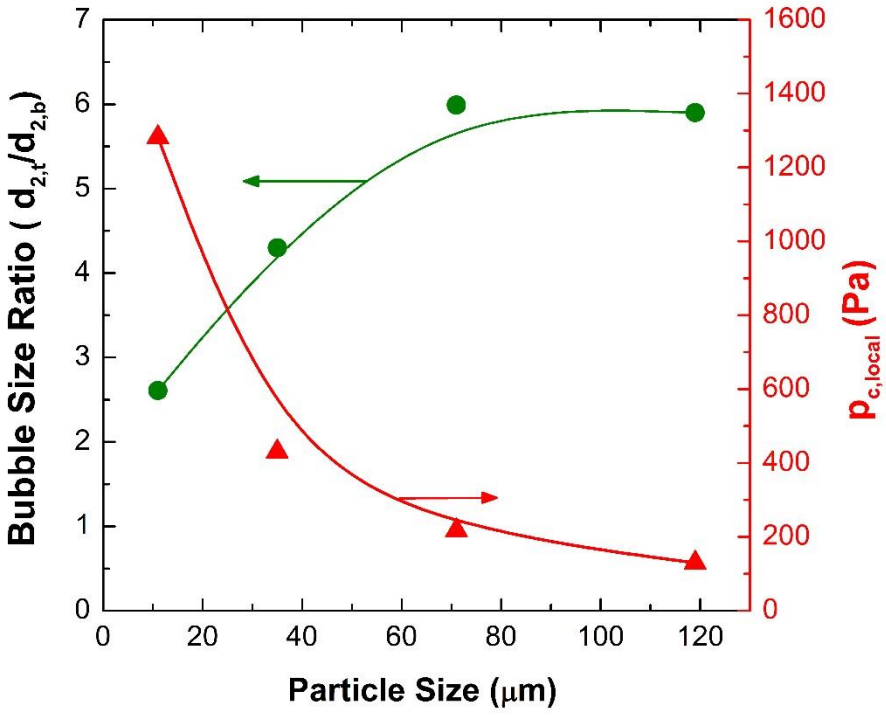

Figure 5.11 Effect of particle size (d_1) on bubble size ratio ($d_{2,t}/d_{2,b}$) and the local capillary pressure ($p_{c,local}$) when the film ruptures. The increase in $d_{2,t}/d_{2,b}$ with increasing d_1 may be partially attributed to the decrease in $p_{c,local}$.

As shown in Figure 5. 12, since both $N_{1,film}$ and $p_{c,local}$ cause p_c to increase with increasing particle size, it was found that p_c increases with particle size

Figure 5.13 shows the effect of particle size on driving force p for filming drainage. This trend can give the explanation for the effect of on particle size forth stability in terms of the drainage rate according to the Reynolds equation.

5.5 Summary and Conclusions

In the present study, the effect of particle size (d_1) on the bubble-coarsening (or froth stability) has been studied by measuring the bubble size ratio between the top and bottom of a forth in the presence of different sizes of particle (d_1 = 11, 35, 71, and 119 μm). We found that the froth

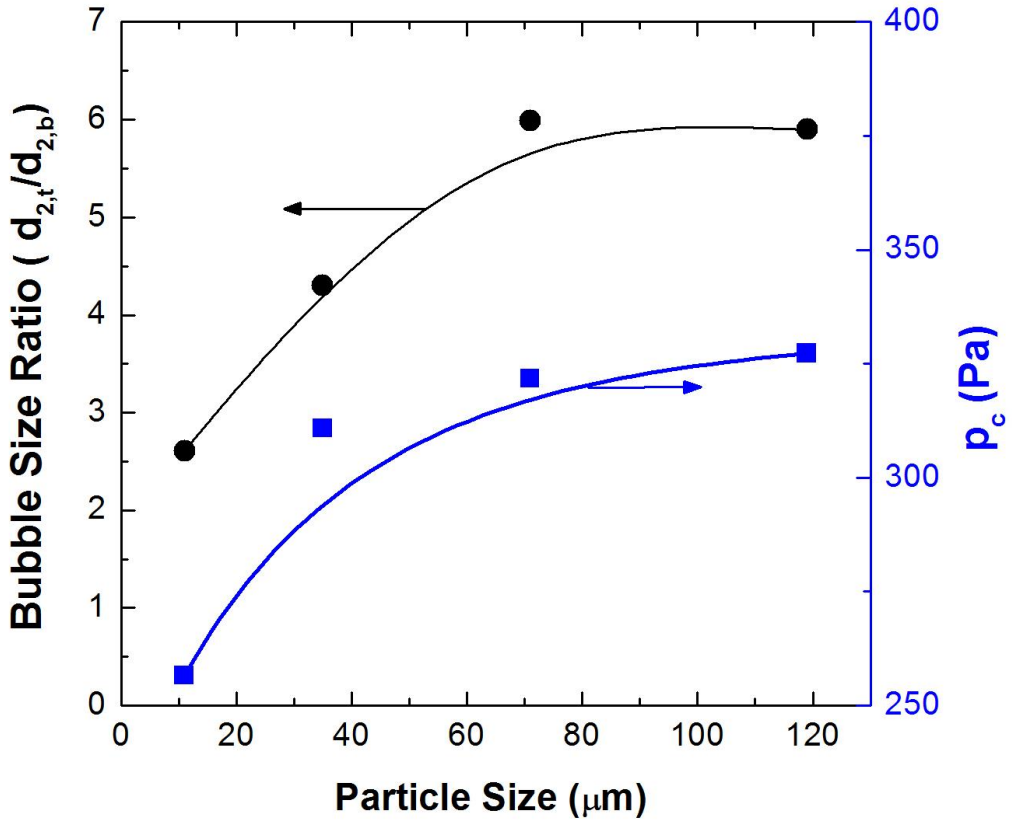

Figure 5.12 Effect of particle size (d_1) on bubble size ratio ($d_{2,t}/d_{2,b}$) and the capillary pressure (p_c) at the critical film thickness (H_{cr}).

stability decreases considerably as particle size becomes coarser from 11 to 71 μm. However, as particle size increases further to 119 μm, the froth stability changes little.

In addition, we have developed a model for predicting the bubble-coarsening in a froth by deriving a film drainage model quantifying the effect of d_1 on the capillary pressure (p_c), which induces the film drainage. The parameter p_c is affected by the number of particles ($N_{1,film}$) in a film and the local capillary pressure ($p_{c,local}$) around particles, which in turn vary with d_1. The model indicates that as d_1 increases, both $N_{1,film}$ and $p_{c,local}$ decreases, causing p_c to increase. As a result, the film drains faster and the froth becomes unstable.

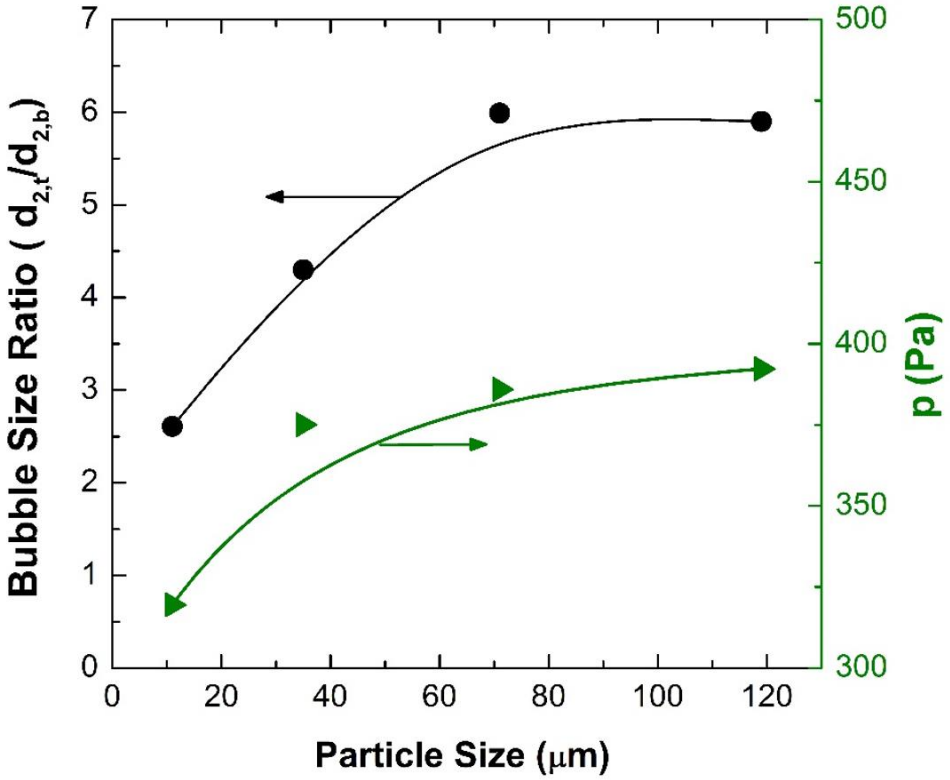

Figure 5.13 Effect of particle size (d_1) on bubble size ratio ($d_{2,t}/d_{2,b}$) and the driving pressure (p) for the film thinning at the critical film thickness (H_{cr}).

References

[1] Seaman, D.R., E.V. Manlapig, and J.P. Franzidis, Selective transport of attached particles across the pulp–froth interface. *Minerals Engineering*, 2006. **19**(6–8): p. 841-851.

[2] Ip, S.W., Y. Wang, and J.M. Toguri, Aluminum foam stabilization by solid particles. *Canadian Metallurgical Quarterly*, 1999. **38**(1): p. 81-92.

[3] Aktas, Z., J.J. Cilliers, and A.W. Banford, Dynamic froth stability: Particle size, airflow rate and conditioning time effects. *International Journal of Mineral Processing*, 2008. **87**(1–2): p. 65-71.

[4] Tang, F.-Q., et al., The effect of SiO2 particles upon stabilization of foam. *Journal of Colloid and Interface Science*, 1989. **131**(2): p. 498-502.

[5] Johansson, G. and R.J. Pugh, The influence of particle size and hydrophobicity on the stability of mineralized froths. *International Journal of Mineral Processing*, 1992. **34**(1–2): p. 1-21.

[6] Morris, G., et al., The effect of particle hydrophobicity, separation distance and packing patterns on the stability of a thin film. *Journal of Colloid and Interface Science*, 2008. **327**(1): p. 138-144.

[7] Ata, S., N. Ahmed, and G.J. Jameson, A study of bubble coalescence in flotation froths. *International Journal of Mineral Processing*, 2003. **72**(1–4): p. 255-266.

[8] Morris, G., S.J. Neethling, and J.J. Cilliers, A model for investigating the behaviour of non-spherical particles at interfaces. *Journal of Colloid and Interface Science*, 2011. **354**(1): p. 380-385.

[9] Comley, B.A., et al., Frother characterisation using dynamic surface tension measurements. *International Journal of Mineral Processing*, 2002. **64**(2-3): p. 81-100.

[10] Reynolds, O., On the Theory of Lubrication and Its Application to Mr. Beauchamp Tower's Experiments, Including an Experimental Determination of the Viscosity of Olive Oil. *Proceedings of the Royal Society of London*, 1886. **40**(242-245): p. 191-203.

[11] Denkov, N.D., et al., A Possible Mechanism of Stabilization of Emulsions by Solid Particles. *Journal of Colloid and Interface Science*, 1992. **150**(2): p. 589-593.

[12] Srinivas, A. and P. Ghosh, Coalescence of bubbles in aqueous alcohol solutions. *Industrial & Engineering Chemistry Research*, 2011. **51**(2): p. 795-806.

[13] Wang, L. Inter-bubble attractions in aqueous solutions of flotation frothers. in *SME Annual Meeting*. 2011. Denver, CO, United States.

Chapter 6. Conclusions and Recommendations for Future Research

6.1 Conclusions

The primary findings and contributions presented in the dissertation are summarized as follows.

1. A thin liquid film (TLF) confined between two bubbles in a froth phase (or in a foam) drains by the capillary pressure (p_c) created from the changes in curvature and the disjoining pressure (Π) created by surface forces in the films. If Π is negative (attractive), the film drainage rate and the wave motions at the air/water interfaces accelerate. When the TLFs thin to a critical film thickness (H_{cr}), the TLF ruptures and the two bubbles become one. The capillary wave model describes the film thinning process and the wave motions using the classical DLVO theory, which considers the repulsive double-layer force and the attractive van der Waals forces only. It has been found in the present work that the H_{cr} values predicted from the capillary wave model are substantially smaller as compared to the experientially measured values in the case of the foam films stabilized by with weak surfactants, *e.g.*, MIBC.

2. Based on the recognition that attractive hydrophobic force is also present in foam films in addition to the double-layer force and the van der Waals force, by incorporating the hydrophobic force in the capillary wave model, the author has developed a model that can predict H_{cr} more accurately. The model shows that the hydrophobic force contributes to accelerate both film thinning rate and surface corrugation growth rate and thereby may cause the film to rupture at higher film thickness.

3. Based on the new H_{cr} model, a model for predicting bubble-coarsening in a dynamic foam has been developed in the present work. The model was developed by deriving a

mathematical relation between the Plateau border area, which controls film drainage rate, and the lamella film thickness, which controls bubble-coalescence rate. The model is able to predict the bubble size ratio between the top and bottom of a foam as a function of surface tension (frother dosage), aeration rate, and foam height. The model was validated using a specially designed foam column equipped with a high-speed camera. It has been found that bubble-coarsening increases with decreasing frother dosage and aeration rate and increasing foam height.

4. In the present study, a model for predicting bubble-coarsening in a froth (3-phase foam) has been developed for the first time. The model was developed by deriving a film drainage model quantifying the effect of particles on p_c. The parameter p_c is affected by the number of particles and the local capillary pressure ($p_{c,local}$) around particles, which in turn vary with the hydrophobicity and size of the particles in the film. Assuming that films rupture at free films, the p_c corrected for the particles in lamella films has been used to determine the critical rupture time (t_{cr}), at which the film thickness reaches H_{cr}, using the Reynolds equation. Assuming that the number of bubbles decrease exponentially with froth height, and knowing that bubbles coalesce when film drains to a thickness H_{cr}, a bubble coarsening model has been developed. This first principle model is capable of predicting the bubble size ratio between the top and bottom of a froth phase as a function of frother dosage, collector dosage (contact angle), particle size, aeration rate, and froth height.

5. The bubble-coarsening froth model developed in the present study has been verified using a Denver laboratory flotation cell using spherical particles of varying hydrophobicity and size. It has been found in the present study that bubble-coarsening decreases with particle contact angle (θ) up to $\theta = 70^o$ due to a decrease in p_c, resulting in retarded film drainage rate. At $\theta > 70^o$, on the other hand, the bubble-coarsening increases due to increased p_c and, hence, increased drainage rate. In addition, it has been shown that bubble-coarsening decreases with particle size, which may be attributed to decreased p_c and drainage rate.

6.2 Recommendations for Future Research

Finally, the author of this dissertation recommends the following works for future research.

1. In a flotation model, a froth recovery is given by a function of the bubble-coarsening factor, which is the bubble size ratio between the top and bottom of a froth phase. By incorporating

the bubble-coarsening froth model developed in the present work into the flotation model, more accurate description of flotation circuits can be possible.

2. The froth model presented in the present work is valid in the presence of fully liberated spherical particles. The study on the effects of liberation and particle shape on froth stability is recommended.

3. The critical rupture thickness (H_{cr}) model presented in the dissertation ignores the film stabilization by film elasticity. At high frother concentration, the film elasticity may play a significant role in determining the film stability and the value of H_{cr}. The H_{cr} model also neglects the possibility that the lamella film between air bubbles thins faster in the presence of hydrophobic force due to possible slip. Those two mechanisms will be worthy to be considered.